Nanophotonic Structures: Fundamentals and Applications in Narrowband Transmission Color Filtering

Thesis by
Dagny Fleischman

In Partial Fulfillment of the Requirements for the
degree of
Doctor of Philosophy

CALIFORNIA INSTITUTE OF TECHNOLOGY
Pasadena, California

2019
Defended June 22, 2018

Dagny Fleischman
ORCID: 0000-0003-2913-657X

ACKNOWLEDGEMENTS

This has been an incredible journey, and it would not have come together without the support and wisdom of a phenomenal group of people. They say it takes a village to raise a child, and through this experience I've seen that is equally applicable to graduate students, because it has certainly taken a village to raise me.

First and foremost, I want to thank my advisor, Harry Atwater. I am incredibly grateful for the freedom Harry has given me to turn my childhood fascination with colors into an extremely gratifying research path. Harry embodies everything a scientist and faculty member should be: keenly intelligent, insatiably curious, and someone who cares as deeply about his students as he does the science he is studying. As much as he has contributed to my development as a scientist, he has added even more to my understanding of just how much an individual can contribute to science and technology. We often joke in lab that "we can't all be Harry Atwater" and I will always be deeply impressed by the nearly impossibly high bar he has set for us all to aspire to.

In addition to Harry's mentorship, I was extremely fortunate to have Luke Sweatlock as a mentor during the early years of my PhD. Our nearly weekly meetings transformed me from an excited fab monkey into an excited fab monkey that could code, perform numerical analysis, and cogently talk about optical phenomena. The skills I learned under Luke's tutelage form the core of the biggest skillsets I've gained during my PhD. His ability to clearly explain optical phenomena is second to none, and I gained so much from our conversations about both science and the world-at-large.

In a previous draft of these acknowledgments I had Michelle Sherrott in at least 4 difference places: in with the labmates, in with the enriching science discussions, in with the close friends, and in with the people who helped shape me into the person I've become. So for the sake of readability I've decided to roll all of those acknowledgments into one: Michelle, thank you for simultaneously managing to embody an inspiring scientist, a helpful colleague, and an amazing friend. You have encouraged me to become the best version of myself for the last 10 years, and I'm so excited to see where we will be after the next 10.

The work in this thesis would not have been possible without my collaborations with Kate Fountaine, Georgia Papadakis, and Colton Bukowsky. Not only was I fortunate to be able to work with and learn from them as scientists, I'm also lucky enough to be able to call them friends. Thank you three for managing to make science even more fun. I also need to acknowledge the many bottles of wine Kate and I sacrificed in the pursuit of our science—I'm so glad that those many years of meetings were as fruitful as they were entertaining.

Over the course of my PhD, I spent many years troubleshooting and spit-balling fab processes, and would not have been nearly as successful without the great ideas of Phil Jahelka, Sisir Yalamachili, and Matt Sullivan Hunt. Along with their help, the filters I fabricated would not have been possible without the extremely hardworking and helpful current and former KNI staff members: Guy DeRose, Nathan Lee, Carol Garland, Melissa Melendes, Burt Mendoza, Barry Baker, and Nils Asplund. Along the same lines, I want to make sure I thank team e-beam past and present (Cris Flowers, John Lloyd, Joeson Wong, and Alex Welch) for all of their hard work helping me keep the evaporator up and running, and Rebecca Glaudell for her tireless work keeping everyone in lab as safe as possible.

I was lucky to meet some great people when I first joined the A-Team, and want to thank Emily Kosten, Victor Brar, and Jim Fakonas for helping me find my footing in the group during my early years. I also want to thank Deep Jariwala, Giulia Tagliabue, Ruzan Sokhoyan, and Artur Davoyan for the help and perspective they've given me during our discussions about both science and life after grad school.

Our group has been incredibly fortunate to have a bunch of amazing administrators who keep the group running. Thank you to Tiffany Kimoto, Jennifer Blankenship, Liz Hormigoso, Lyann Lau, and Jonathan Gross for your ceaseless help and words of encouragement.

Ladies night at Amigos was one of my favorite parts of being a member of the A-Team, so I need to thank Yulia Tolstova, Kelly Mauser, Rebecca Saive, and Yuri the Beautiful for always being game to order another pitcher of margaritas. (Also, a special shout-out to Sisir for being the only person in lab capable of matching me margarita-for-margarita.)

I have been lucky to make some really amazing friends during my time in LA. Aysen and Richard Norte welcomed me into Fillmore house before I started Caltech, and their friendship turned LA into home faster than I could have believed possible. I also want to thank the staff at the Trader Joes on Arroyo Parkway (the original Trader Joes, in case anyone was wondering). They helped transform LA from a new city into a small town where everyone knows my name. Thank you all for always being friendly and never (outwardly) judging all those times Carey and I were having pizza and wine for dinner for third night that week.

I am so lucky to have great friends near and far that are always supportive and understanding, even when I'm too submerged in lab to respond to texts. Thank you Didi Rado, Oni Lazurus, the Wives, Kalla Gervasio, Elaine Kwon, Laura Lee, Nini Lee, Zac Ostrow, and Hillary Corbin for the late night pep talks, support, and the much needed distractions.[1]

My parents, Paul and Dawn Fleischman, dealt with a never-ending stream of questions for the entirety of my childhood. Thank you both for fostering and celebrating my curiosity. Your support is what put me on this path and made this thesis possible.

And last, and by far most importantly, thank you C. For everything. For making sure I ate and slept enough these last few months. For your patience with all my late night tool runs and with the fact that I apparently do my best writing between the hours of 10 pm and 3 am. For making life so wonderful. Thank you.

[1] Not going to lie, I now understand how Oscars speeches get so out-of-hand

For C

Years of studying light-matter interactions made it clear
that yours is the light that matters most.

ABSTRACT

The optical properties of materials can be manipulated by structures roughly the size of the wavelength of light of interest. For visible wavelengths, many different types of structures sized on the order of 10s-100s of nanometers have been used to engineer materials to produce a targeted optical response. Multilayer stacks of nanoscale metal and dielectric films are a widely explored geometry that has been used to make composite materials with effective optical properties that vary significantly from their constituent films. In this thesis, carefully designed multilayer stacks were used to induce artificial magnetism in non-magnetic materials, opening new directions for tailoring wave propagation in optical media. By perforating these multilayer structures with an array of sub-wavelength slits, these nanophotonic structures were shown to be able to function as narrowband transmission color filters. Using numerical optimization methods, these narrowband filters were further refined and simplified to only require a single thin film sandwiched between two mirrors to achieve this high resolution spectral filtering. Novel methods were used to fabricate these ultracompact narrowband transmission color filters, which were shown to possess extremely narrow transmission resonances that can be controllably pushed across the visible and near IR parts of the spectrum. These mirrored color filters have footprints as small as 400 nm, well below the size of state-of-the-art CMOS pixels, inviting the possibility for integrating multi- and hyperspectral imaging capabilities into small portable electronic devices.

PUBLISHED CONTENT AND CONTRIBUTIONS

[1] Dagny Fleischman, Luke A. Sweatlock, Hirotaka Murakami, and Harry Atwater. "Hyper-selective plasmonic color filters". In: *Opt. Express* 25.22 (2017), pp. 27386–27395. DOI: 10.1364/OE.25.027386.
DF participated in the design, optimization, analysis, fabrication, and measurement of the structures and led the writing of the manuscript.

[2] Georgia T. Papadakis, Dagny Fleischman, Artur Davoyan, Pochi Yeh, and Harry A. Atwater. "Optical magnetism in planar metamaterial heterostructures". In: *Nature Communications* 9.296 (2018). DOI: 10.1038/s41467-017-02589-8.
DF participated in the design of the structures, fabricated the heterostructures, performed the TEM measurements, and participated in the writing of the manuscript.

[3] Kelly W. Mauser, Seyoon Kim, Slobodan Mitrovic, Dagny Fleischman, Ragip Pala, Youngeun Kim, K. C. Schwab, and Harry A. Atwater. "Resonant thermoelectric nanophotonics". In: *Nature Nanotechnology* 12.770 (2017). DOI: 10.1038/nnano.2017.87.
DF participated in initial discussions of the concept, the development of the fabrication method, and took the angle resolved measurements.

[4] Mary X. Wang, Soyoung E. Seo, Paul A. Gabrys, Dagny Fleischman, Byeongdu Lee, Youngeun Kim, Harry A. Atwater, Robert J. Macfarlane, and Chad A. Mirkin. "Epitaxy: Programmable Atom Equivalents Versus Atoms". In: *ACS Nano* 11.1 (2017), pp. 180–185. DOI: 10.1021/acsnano.6b06584.
DF fabricated the nanoparticle arrays used for epitaxy.

TABLE OF CONTENTS

LIST OF ILLUSTRATIONS

Number *Page*

Chapter 1

INTRODUCTION

> The agreement of the results seems to show that light and magnetism are affections of the same substance, and that light is an electromagnetic disturbance propagated through the field according to electromagnetic laws.
>
> James Clerk Maxwell, 1865

1.1 Optical Properties of Materials

The work presented in this thesis is grounded in optical effects derived from the interactions of light with metals and dielectrics. Although these materials interact with light in vastly different ways, their responses are dictated by their electronic structure. The optical response of metals is largely controlled by their loosely bound conduction band electrons. These electrons move in response to incident electromagnetic radiation and shield the metal from developing any internal electric fields. This shielding behavior is what produces the characteristic reflectance seen in many metals at and near visible frequencies. Dielectric materials, in contrast, have electrons that are far more tightly bound to their nuclei. Without the ability to move as freely, these materials lack the same shielding effects seen in metals and are largely transparent.

Maxwell's Equations can be used to more precisely describe the interaction between electromagnetic radiation and materials. These equations, as listed in Equations 1.1 through 1.4, are

$$\nabla \cdot \mathbf{D} = \rho_{ext} \tag{1.1}$$

$$\nabla \cdot \mathbf{B} = 0 \tag{1.2}$$

$$\nabla \times \mathbf{E} = -\frac{\partial \mathbf{B}}{\partial t} \tag{1.3}$$

$$\nabla \times \mathbf{H} = -\frac{\partial \mathbf{D}}{\partial t} + \mathbf{J} \tag{1.4}$$

These equations relate the four fields within a system, the displacement field **D**, electric field **E**, magnetic field **H**, and magnetic induction field **B** to the charge carrier density ρ_{ext} and the current density **J**.

There are two constitutive relationships that can be used to link the dielectric displacement to the electric field and the magnetic field to the magnetic induction.

$$\mathbf{D} = \epsilon \mathbf{E} \tag{1.5}$$

$$\mathbf{H} = \frac{1}{\mu}\mathbf{B} \tag{1.6}$$

Equations 1.5 and 1.6 relate these quantities via the electric permittivity ϵ and the magnetic permeability μ. As implied by its name, the dielectric permittivity is a measure of how much charge is needed to generate a single unit of electric flux in a material (i.e., how well it can resist the generation of electric flux). In a similar vein, the magnetic permeability describes how well a material can support a magnetic field within itself. With these two quantities, we can fully define a materials interaction with electromagnetic radiation[1]. ϵ and μ can each be either positive, negative, or zero, and their values have significant effects on material behavior. Excluding the ϵ and/or $\mu = 0$ cases (which are extremely interesting, but beyond the scope of this thesis), the possible combinations of ϵ and μ are summarized in Figure 1.1.

We can use ϵ and μ to expand on the discussion at the start of this section: while both metals and dielectrics possess an $\epsilon > 1$, their vastly different optical responses arise from the difference between possessing a positive or negative μ. In addition to having interesting optical responses individually, combining materials with high

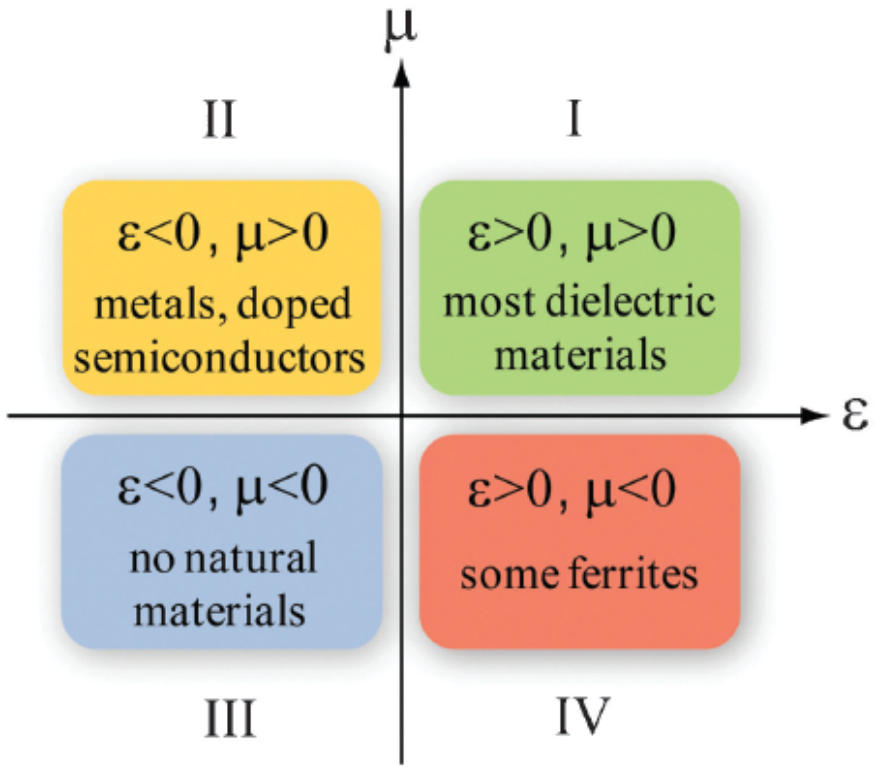

Figure 1.1: The four different combinations of positive and negative ϵ and μ and a description which classes of materials display these optical responses[2]

mu contrast can lead to some very useful optical effects, which will be utilized in all the chapters of this thesis.

1.2 Nanophotonics

While the electronic structure of a material dictates how light and matter interact, these interactions can be manipulated by introducing inhomogenieties in the material that are on the order of the wavelength of interest. These inhomogenieties can be voids, different materials, changes in roughness, etc, but they all serve the same purpose: to change the ϵ and occasionally μ of the materials system.

Without the assistance of measurement tools or exotic materials, the human experience is largely confined to interactions with electromagnetic radiation spanning from the UV, visible, and near infrared parts of the spectrum, roughly 100 nm to 2 μm in wavelength. The inhomogenieties required to manipulate light-matter interactions in this part of the spectrum therefore need to be on the order of 10s - 100s of nm. Relatively recent developments in fabrication technology have given

us the ability to precisely shape dielectrics, semiconductors, and metals at these lengthscales. The field of nanophotonics uses these nanoscale structures to directly engineer optical responses. These engineered structures have developed into new technologies ranging from those already in use such as light emitting diodes to burgeoning new technologies including cancer treatments, high density optical storage, and all-optical computing[3–6].

Nanophotonics is a broad discipline within optical engineering that can be divided into four relatively distinct areas[7]. The first area can be briefly summarized as electron confinement effects on optical properties. The structures in this field are on the scale of a few nanometers and have precisely tailored size-dependent absorption, emission, and transmission spectra. The second area is light wave confinement phenomena and is the study of wave propagation in structured dielectrics for use in photonic circuitry elements. The third area is concerned with the quantum optics of nanostructures and has been explored to develop lasing systems.

The fourth section is the utilization of metal-dielectric nanostructures, which forms the core of the work in this thesis. Until the advent of nanophotonics, metals were not used in optical engineering for anything other than mirrors [7]. However, these materials become extremely interesting at the nanoscale, where ϵ and μ can be manipulated for visible wavelengths. These manipulations can be used to produce metamaterials composed of sub-wavelength unit cells of materials and can be tailored to produce optical responses that cannot be found in natural materials [2, 8]. Additionally, the favorable surface-area to volume ratios of nanostructures give surface effects the ability to dominate over the bulk and can give rise to surface electron oscillations of electrons that can mediate light-matter interactions. These collective oscillations, called plasmons, present a toolbox for manipulating light-matter interactions at metal-dielectric interfaces.

Plasmonics

Conduction band electrons can be excited into collective oscillations relative to the lattice atoms in metals. These oscillations, called plasmons, are quantized, and can therefore be treated as a quasiparticle with a well defined wavelength. Plasmons can propagate both through the bulk of a material (volume plasmons) or be confined onto a materials surface. In this thesis, we consider the case of surface plasmons that are coupled with incident light, which are called surface plasmon polaritons (SPPs).

Within the field of plasmonics, SPPs are used to confine, filter, and propagate light at the interface of negative and positive ϵ materials.

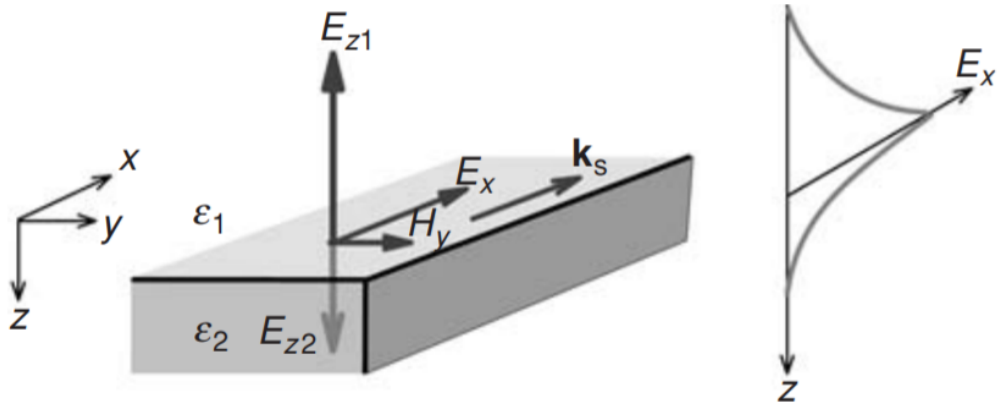

Figure 1.2: A metal slab suspended in vacuum that supports a surface plasmon polariton mode at the sharp interface of ϵ_1 and ϵ_2. The x component of the electric field vector E_x decays exponentially in the z direction both into the metal slab and into the vacuum. k_s is the wave vector of the supported surface plasmon polariton[7]

The nature of these propagating modes can be derived directly from Maxwell's equations (Equations 1.1 - 1.4)[7]. When carrier density ρ_{ext} and current density $\mathbf{J}$ are both zero and only non-magnetic media are considered these equations can be used to derive the Helmholtz equation (Equation 1.7). This relation describes the spatial distribution of an electric field when electromagnetic radiation (with frequency ω) propagates through a medium with index of refraction $n(\mathbf{r})$

$$\nabla^2 E(\mathbf{r}) + k^2 E(\mathbf{r}) = 0 \tag{1.7}$$

$$k = \frac{n(\mathbf{r})}{c}\omega \tag{1.8}$$

where E($\mathbf{r}$) is the electric field, ω is the frequency of the electric field, k is the wave number of the electric field, n is the index of refraction of the medium, and c is the speed of light. By considering the metal slab in a vacuum shown in Figure 1.1, where the dielectric function changes abruptly at the metal-vacuum interface from ϵ_1 to ϵ_2 and the electric field is of the form $\mathbf{E}(x, y, z) = \mathbf{E}(z)exp(ik_x x)$, the Helmholtz equation can be written in the form,

$$\frac{\partial \mathbf{E}(z)}{\partial z^2} + [k_0^2 \epsilon(z) - k_x^2]\mathbf{E} = 0 \tag{1.9}$$

combining Equation 1.9 with Equations 1.3 and 1.4 of Maxwell's Equations can be used to yield two sets of solutions for two different polarizations of propagating modes. The transverse magnetic mode (TM mode) has non-zero E_x, E_z, and H_y field components, whereas the transverse electric mode (TE mode) has non-zero H_x, H_z, and E_y.

For the interface geometry shown in Figure 1.1 it can be shown that to maintain continuity across the metal-vacuum interface

$$\frac{k_{z1}}{k_{z2}} = -\frac{\epsilon_1}{\epsilon_2} \tag{1.10}$$

The wave vectors must be real and positive, which means that ϵ_1 and ϵ_2 must have opposite signs. This confirms the assertion made above that surface plasmons polaritons are only supported on interfaces where one material is a metal and the other is a dielectric. Using equation 1.10 and some arithmetic, the H_y continuity condition can solved for to yield Equation 1.11, which provides the dispersion relation of the surface plasmon polariton mode.

$$k_x = \frac{\omega}{c}\sqrt{\frac{\epsilon_1 \epsilon_2(\omega)}{\epsilon_1 + \epsilon_2(\omega)}} \tag{1.11}$$

The dispersion relation can be plotted, as shown in Figure 1.3 for the cases of both an ideal free electron plasma and an Ag/air interface. The dispersion relation of the plasmon modes approaches that of light in a vacuum for smaller wavenumbers, and therefore the SPP mode behaves like electromagnetic radiation incident on a dielectric at grazing incidence. By contrast, at higher wave numbers the SPP mode asymptotically approaches the surface plasmon frequency described by Equation 1.12, where ϵ_1 is the permittivity of the dielectric.

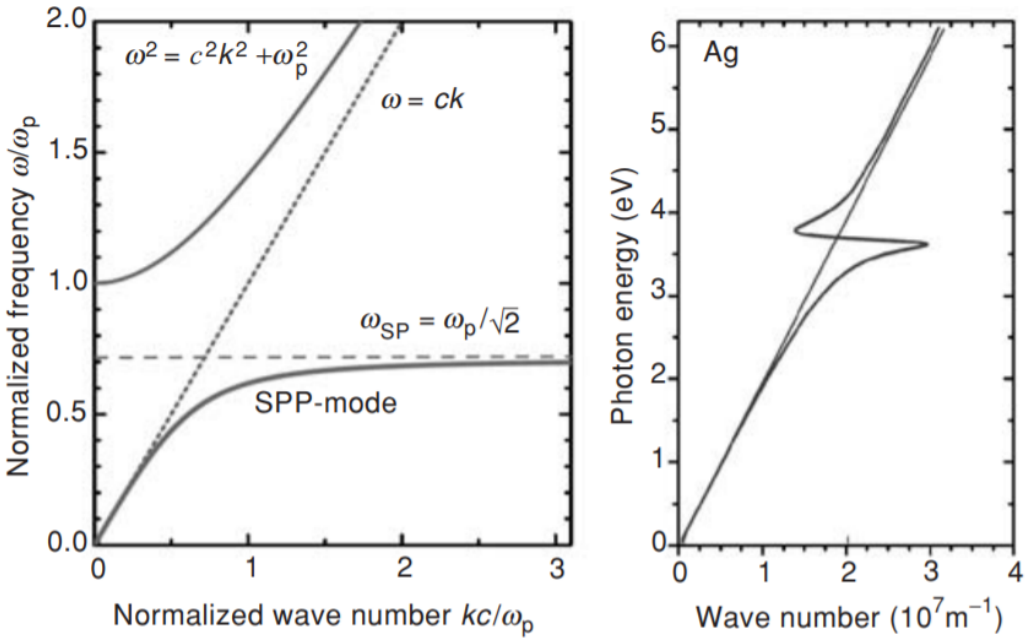

Figure 1.3: Left: the solid lines are the dispersion curve for an ideal free electron plasma in vacuum. The dashed line is the dispersion for light in vacuum. The SPP mode always has more energy at a given frequency than light in free space, illustrating the need photons have for a momentum boost in order to couple into SPP modes. Right: a dispersion curve for Ag/air interface. Interband transitions cause the substantial variation from the ideal electron plasma case [7]

$$\omega_{SP} = \frac{\omega_P}{\sqrt{1+\epsilon_1}} \tag{1.12}$$

In real metals, interband transitions effect the dispersion relation and prevent the SPP mode from achieving arbitrarily long wavenumbers, as shown in the right-hand panel of Figure 1.3.

There are no wavenumbers for which the SPP dispersion curve is within the light cone. Therefore, SPPs cannot be excited by just an external incident electromagnetic wave, because light at a given frequency has less momentum than a plasmon at the same frequency. Therefore, to excite an SPP, there must be momentum transfer to to give the SPP mode the momentum boost it needs. There are a number of methods that can be used to excite surface plasmons, including prism coupling, near-field excitation using leaky modes, and excitation using diffraction gratings[9–12]. This need for a momentum boost to access plasmon modes can act as a filtering

mechanism that only allows certain wavelengths of light to couple into SPPs. This property has been used to demonstrate plasmonic color filtering, which will be addressed in depth in depth in Chapters 3 and 4[13, 14].

The derivation leading to the plasmon dispersion relation and the references it is drawn from agree that while there are available modes for TM plasmons, there are no allowed TE modes. Any attempt at solving for TE modes would violate the electric and magnetic field continuity requirements at the metal-dielectric interface. This arises from one of the initial assumptions made in this derivation, that $\mu = 1$. It will be shown in Chapter 2 of this thesis that it is possible for materials with $\mu < 1$ to support TE polarized magnetic surface plasmon modes.

Metamaterials

A metamaterial can be concisely defined as a "*Man-made or otherwise artificially structured material with inclusions embedded in a host medium or patterned on a host surface, where the length scale of the inclusions is significantly smaller than the wavelength of interest*"[15]. Because these inclusions need to be much smaller than the wavelength of light they seek to manipulate, the first demonstrations of intentionally designed[1] metamaterials were composed of copper strings and split ring resonators on circuit boards that interacted with microwave electromagnetic radiation[16]. Within 10 years of that initial experimental verification, advanced fabrication techniques have allowed for the demonstration of metamaterials that have manipulated optical properties for visible light.

These metamaterials seek to fill the gap in optical properties shown in Figure 1.1: the lack of natural materials that have both ϵ and μ simultaneously less than zero. The index of refraction is defined as $n^2 = \epsilon\mu$, and materials that have both ϵ and μ less than zero possess a negative index of refraction[17]. Negative index of refraction materials possess a number of exotic properties, including backwards refraction. Light crossing a border between materials with two different refractive indexes diffracts, as illustrated by Snell's Law:

$$n_1 sin(\theta_1) = n_2 sin(\theta_2) \tag{1.13}$$

As equation 1.13 shows, when light crosses the border between a positive n material

[1] Glass artisans managed to create metal nanoparticle based metamaterials to produce colors in stained glassed at least 1700 years ago, though remarkably, we didn't understand how this worked until Mie scattering theory was developed in 1908[15]

and a negative n material, it refracts backwards. This phenomenon is illustrated in Figure 1.4. The development of negative index metamaterials (NIMs) has been a very active field because of their their exotic and potentially impactful applications including: optical cloaking, sub-wavelength imagining with hyperlenses, and optical circuitry elements[18–20].

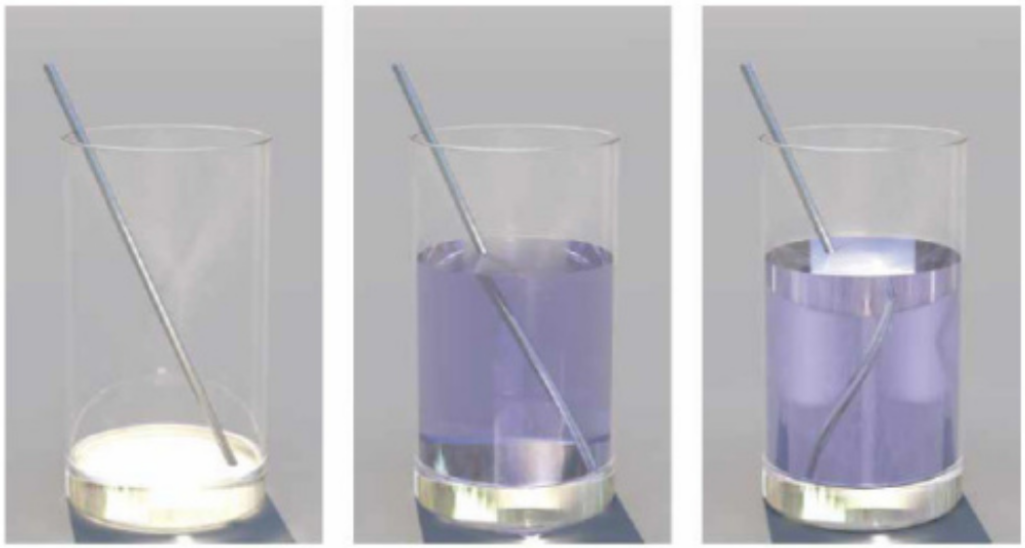

Figure 1.4: Photorealistic calcuations of refraction in positive and negative index of refraction materials. Left: an empty glass with a straw. Center: a glass filled with water $n = 1.3$ that demonstrates conventional refraction. Right: a glass filled with a negative index material $n = -1.3$ illustrating backwards refraction [21]

There are a number of ways to achieve $\mu < 0$ to create NIMs. Composite resonance based NIMs utilize a magnetic resonance to achieve negative index at select frequencies[22]. Engineering a non-isotropic permittivity in a metamaterial can also be used to create a NIM [23]. ϵ can be engineered to be directionally anisotropic, by patterning sub-wavelength features with specific ϵ such that components of the inclusions of a material have negative permittivity relative to the surrounding medium[24]. This material can be treated as a uniaxial metacrystal with the permittiivty tensor, shown in Equation 1.14 and described by the dispersion relation in Equation 1.15[25].

$$\epsilon = \begin{pmatrix} \epsilon_{xx} & 0 & 0 \\ 0 & \epsilon_{yy} & 0 \\ 0 & 0 & \epsilon_{zz} \end{pmatrix} \tag{1.14}$$

$$\frac{(k_x^2 + k_y^2)}{\epsilon_{zz}} + \frac{k_z^2}{\epsilon_{xx}} = (\frac{\omega}{c})^2 \tag{1.15}$$

where $\epsilon_{xx} = \epsilon_{yy}$ in Equation 1.14 to yield Equation 1.15. The dispersion is unbounded, so the HMM can support propagating waves with infinitely large k-vectors[26]. Figure 1.5 displays three different types of dispersion. Figure 1.5(a) provides the dispersion for an isotropic $\epsilon > 0$ material for context. Figure 1.5(b) shows the dispersion for a material that possesses hyperbolic dispersion and $\epsilon_{xx} = \epsilon_{yy} > 0$ and $\epsilon_{zz} < 0$. This HMM is classified as Type I and are primarily dielectric and so have relatively low loss. Type II HMMs are shown in Figure 1.5(c). These materials have $\epsilon_{xx} = \epsilon_{yy} < 0$ and $\epsilon_{zz} > 0$.

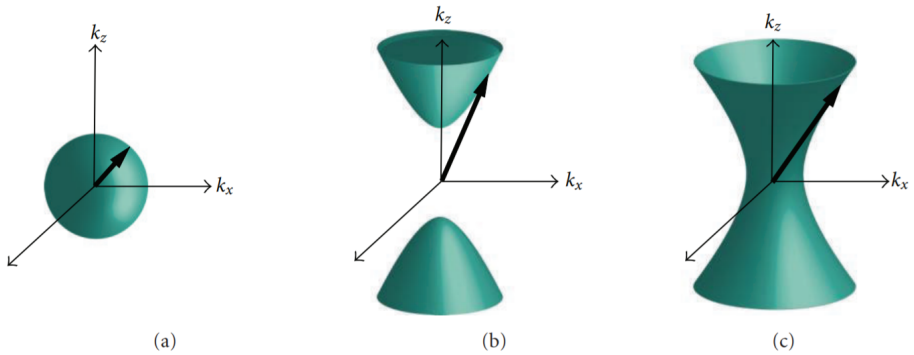

Figure 1.5: (a) Dispersion for isotropic materials (b) Dispersion for Type I HMMs where $\epsilon_{xx} = \epsilon_{yy} > 0$ and $\epsilon_{zz} < 0$ (c) Dispersion for Type II HMMs where $\epsilon_{xx} = \epsilon_{yy} < 0$ and $\epsilon_{zz} > 0$ [25]

There are a number of ways to implement HMMs, and they can be relative simple structures, even at optical frequencies. Experimental demonstrations of HMMs have been achieved with planar stacks of alternating materials (including graphene) and nanowire arrays [27–29].

1.3 Color Filtering in CMOS Devices

CMOS Image Sensors

Nanophotonic structures have been proposed for a variety of applications, and their small mode volumes makes them particularly promising as color filters in state-of-the-art complementary metal-oxide semiconductor (CMOS) image sensors. CMOS image sensors convert an optical signal into an electrical response that can be interpreted to form an image. Image sensors, along with the microlenses, and color filters, form the core of the data acquisition that converts a real-space scene into a digital image via the imaging system pipeline shown in Figure 1.6[30].

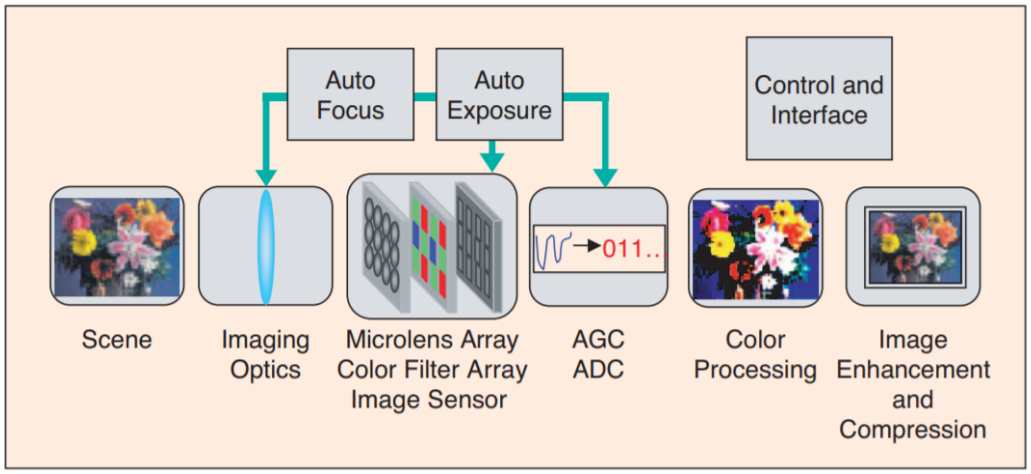

Figure 1.6: The imaging pipeline. Light that was incident on real-space objects is focused onto the image sensor using the imaging optics. It passes through a microlens array and a mosaiced color filter array that selectively filters red, green, and blue. When light of the appropriate color passes through a filter, the CMOS pixel beneath it generates an electrical signal that is digitized by an analog-to-digital converter. A color processing step is then used to demosaic the color data and the final image can be digitally processed to remove any artifacts[30]

A CMOS image sensor can be viewed as a circuit composed of a photodiode, a photodiode reset switch, signal amplification, and output circuits[31]. They are currently preferred to charge coupled devices (CCDs) because they are less expensive, have relatively low power consumption, and they integrate sensing with analog-to-digital processing on the individual pixel level[30, 31]. Currently organic dye based color filters are used in CMOS image sensors. In CMOS image sensors, these dye based filters are arranged in the Bayer mosaic pattern which is composed of twice the green filters as blue or red to account for the human eye's increased sensitivity to green light[32]. A visual of this layout is shown in Figure 1.7.

While this combination of dye filters and layout has been successfully utilized since the 1970s, as pixel sizes have decreased, issues with optical cross talk and the cost associated with manufacturing these dye based filters have increased significantly[33]. These dye based filters also suffer from degradation with UV exposure and in elevated temperature environments[34]. Nanophotonic structures have shown promise for replacing organic dye filters in small pixel CMOS image sensors due to their robustness against degradation and limited optical cross-talk[34, 35].

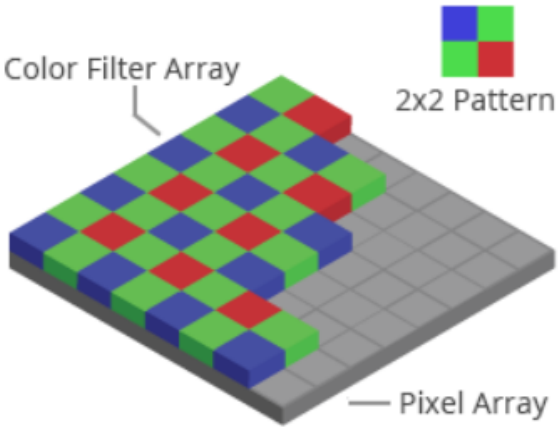

Figure 1.7: Bayer Mosaic layout for red, green, and blue color filters on an array of CMOS pixels. The 2 x 2 array illustrates that there are twice the green pixels as there are blue or red[36]

Multi and Hyperspectral Imaging

While human eyes are limited to red, green, and blue color filtering, devices are capable of far more. The spectral selectivity of some nanophotonic structures presents the opportunity for increasing the spectral resolution of devices by utilizing narrower bandwidth filters. By utilizing spectral filters with smaller bandwidths, instead of just collecting data about three colors, devices can collect data about the way materials interact with 10s and 100s of spectral bands, providing enough data to perform spectroscopy.

These narrowband nanophotonic filters allow for the possibility of developing CMOS image sensors as multi- and hyperspectral imaging systems. In these imagining systems, more than just the three red, green, and blue colorbands are collected to allow for reconstructing an optical spectrum at a given pixel of an image. The distinction between multi- and hyperspectral imaging is blurred and discipline dependent[37]. But generally multispectral imaging has fewer spectral bands than hyperspectral imaging, and hyperspectral imaging can have in excess of 100 spectral bands.

There have been a number of different multi- and hyperspectral imaging architectures employed to gather this additional spectroscopic data. There are a number of techniques used to collet multi- and hyperspectral data. Two of the most common are push broom and tunable spectral filters. In push broom imaging, a single line

of a scene is diffracted across a grating and onto an array of pixels[38]. One axis in the array records the varying spatial response and the other axis records the spectral response. The camera is then scanned across the scene in a line-by-line fashion to collect the entire three dimensions of data in the scene (the two spatial and one spectral dimension). The need to scan the scene with the camera means that the spatial information is not collected simultaneously, while all spectral data is collected at the same time[39]. Electrically tunable spectral filters possess the opposite data capturing behavior: the bandpass are electrically modulated to allow different spectral bands to illuminate the underlying pixel array[39]. So in this configuration, all spatial data is collected simulatenously while the spectral data is collected over time. The spectral data collected is limited by the number of accessable spectral bands of the filter, so the tunable configuration does not have the spectral resolution of pushbroom sensors[37]. The multi- and hyperspectral imaging configurations are used dependent on the intended application.

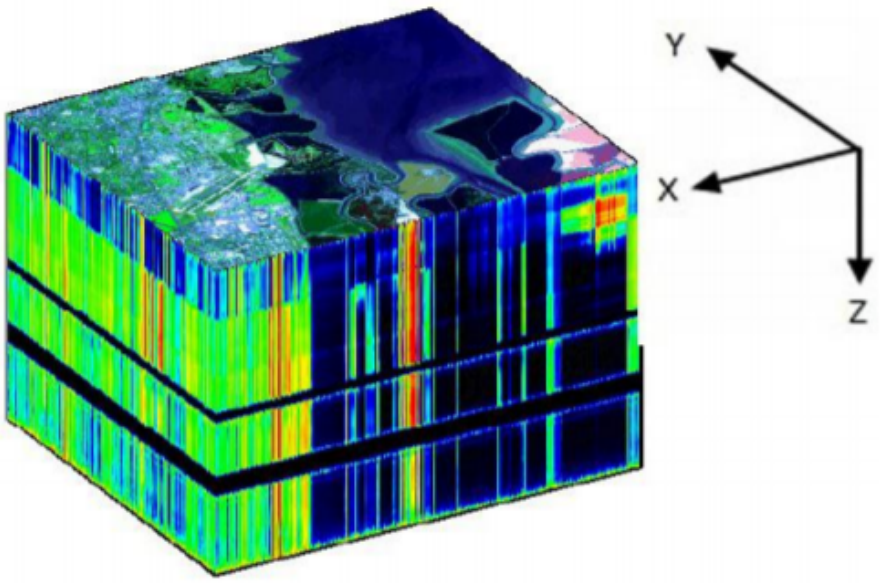

Figure 1.8: Image cube of data collected from an airborn hyperspectral image sensor of the earth below. x and y are the spatial directions and z contains the spectral data collected at each (x,y) point[40]

Multi- and hyperspectral imaging have found applications in a large variety of fields. The technique was developed for use in remote earth sensing to determine mineral composition from airborne sensors[41]. A representative image of this type of data is shown in Figure 1.8[40]. The ability to resolve the materials in an image from a distance has also been proven useful in military applications, where camouflage,

smoke, and flares can be flouted by spectral analysis[42]. Multi- and hyperspectral analysis has also been usefully applied in archaology, art conservation, and analysis of historical documents where it is used to visualize underdrawings, determine ink types, and perform damage detection[37, 43]. There is a growing movement in healthcare to utilize additional spectroscopic data, where it has already found applications in monitoring wound healing, cancer detection, and retinal diseases [44–46]. Multi- and hyperspectral imaging have been utilized in non-destructive food analysis capable of identifying safety hazards and shown promise in forensic analysis, where it can identify the age of bruises and identify the chemical composiiton and spatial distribution of forensic traces, among many other applications[47–49].

1.4 Scope of This Thesis

Broadly, this thesis addresses the design, fabrication, and analysis of three different types of nanophotonic structures. The first class of structures investigated looks at developing exotic optical affects in simple multilayer geometries. The other two structures are focused on a more immediate application: the pursuit of a narrowband color filter capable of endowing CMOS image sensors with the ability to do multi and hyperspectral imaging.

In Chapter 2, we describe the design, fabrication and measurement of metamaterials that possess $\mu \neq 1$ using a simple 5 layer stack of materials. The ability to induce artificial magnetism in these multilayer structures provides for new understanding in the plasmonic and hyperbolic properties of these simple structures. Most excitingly, using the magnetic effects in this system, we were able to report the existence of transverse electric polarized interface bound modes, analogous to their TM polarized counterparts, surface plasmon polaritons. These TE plasmons open new directions for tailoring wave propagation in optical media and generalize our view of plasmonics.

Using nanophotonic geometries very similar to the multilayer structures discussed in the previous chapter, Chapter 3 adapts these five layer structures for color filtering applications. By introducing a grating of slits that perforates an $Ag/SiO_2/Ag/SiO_2/Ag$ stack of thin films, this nanophotonic structure can produce single-peak narrowband transmission in the visible and near-IR parts of the spectrum. We used finite difference time domain (FDTD) methods to find the optimized filter structure, before we fabricated the filter and verified its narrowband filtering behavior.

While the narrowband transmission results in the previous chapter were promising, the use of a grating meant that these structures rely on long-range order. The array of slits puts a constraint on the minimum size of the filter, because a narrowband resonance cannot be produced with too few slits. In Chapter 4, a filter is discussed that circumvents this size constraint by introducing reflective barriers at either side of a single slit. FDTD simulations indicated that this mirrored geometry lifts the need for multiple film stacks. A single film with a single slit was capable of producing a single narrowband transmission peak. Numerical optimization methods were used to find a champion filter capable of producing a single narrowband transmission peak that can be shifted across the spectrum by shifting the position of the mirrors. This nanophotonic system is independent of materials system and has been shown to function in the visible and near-IR with Ag and Cu, and proposed to also function at longer wavelengths. Prototype filters were fabricated using a new fabrication method developed specifically to produce these high quality filters. Measurements confirmed that filters as small as 500 nm square were capable of producing the transmission responses predicted by our calculations.

While the methods for making the nanostructures discussed in this thesis are addressed in some depth in the main text, for the sake of readability some of the details were omitted. The final chapter of this thesis is a cookbook with precise recipes containing the exact details for the various fabrication methods, which should be sufficient for recreating all of the structures described.

References

[1] Arthur Davoyan and Nader Engheta. “Magnetized Epsilon-Near-Zero (ENZ) Structures: Hall Opacity, Hall Transparency, and One-Way Photonic Surface States”. In: *arXiv:1309.2650v1* (2013).

[2] Yongmin Liu and Xiang Zhang. “Metamaterials: a new frontier of science and technology”. In: *Chem. Soc. Rev.* 40 (5 2011), pp. 2494–2507.

[3] Siddha Pimputkar et al. “Prospects for LED lighting”. In: *Nature photonics* 3.4 (2009), p. 180.

[4] Xiaohua Huang et al. “Cancer cell imaging and photothermal therapy in the near-infrared region by using gold nanorods”. In: *Journal of the American Chemical Society* 128.6 (2006), pp. 2115–2120.

[5] Min Gu, Xiangping Li, and Yaoyu Cao. “Optical storage arrays: a perspective for future big data storage”. In: *Light: Science & Applications* 3.5 (2014), e177.

[6] Nader Engheta, Alessandro Salandrino, and Andrea Alu. “Circuit Elements at Optical Frequencies: Nanoinductors, Nanocapacitors, and Nanoresistors”. In: *Phys. Rev. Lett.* 95 (9 2005), p. 095504.

[7] Sergey V. Gaponenko. *Introduction to Nanophotonics*. Cambridge University Press, 2010.

[8] Alexandra Boltasseva and Vladimir M Shalaev. “Fabrication of optical negative-index metamaterials: Recent advances and outlook”. In: *Metamaterials* 2.1 (2008), pp. 1–17.

[9] Erwin Kretschmann. “Die bestimmung optischer konstanten von metallen durch anregung von oberflächenplasmaschwingungen”. In: *Zeitschrift für Physik A Hadrons and nuclei* 241.4 (1971), pp. 313–324.

[10] Claes Nylander, Bo Liedberg, and Tommy Lind. “Gas detection by means of surface plasmon resonance”. In: *Sensors and Actuators* 3 (1982), pp. 79–88.

[11] Stefan A Maier et al. “Local detection of electromagnetic energy transport below the diffraction limit in metal nanoparticle plasmon waveguides”. In: *Nature materials* 2.4 (2003), p. 229.

[12] R. H. Ritchie et al. “Surface-Plasmon Resonance Effect in Grating Diffraction”. In: *Phys. Rev. Lett.* 21 (22 1968), pp. 1530–1533.

[13] Thomas W Ebbesen et al. “Extraordinary optical transmission through sub-wavelength hole arrays”. In: *Nature* 391.6668 (1998), p. 667.

[14] J. A. Porto, F. J. Garcia-Vidal, and J. B. Pendry. “Transmission Resonances on Metallic Gratings with Very Narrow Slits”. In: *Phys. Rev. Lett.* 83 (14 1999), pp. 2845–2848.

[15] Kenneth Diest. *Numerical methods for metamaterial design*. Springer, 2013.

[16] David R Smith et al. “Composite medium with simultaneously negative permeability and permittivity”. In: *Physical review letters* 84.18 (2000), p. 4184.

[17] Viktor G Veselago. “The electrodynamics of substances with simultaneously negative values of and μ”. In: *Soviet physics uspekhi* 10.4 (1968), p. 509.

[18] John B Pendry, David Schurig, and David R Smith. “Controlling electromagnetic fields”. In: *science* 312.5781 (2006), pp. 1780–1782.

[19] Zhaowei Liu et al. “Far-Field Optical Hyperlens Magnifying Sub-Diffraction-Limited Objects”. In: *Science* 315.5819 (2007), pp. 1686–1686.

[20] Nader Engheta. “Circuits with Light at Nanoscales: Optical Nanocircuits Inspired by Metamaterials”. In: *Science* 317.5845 (2007), pp. 1698–1702.

[21] Gunnar Dolling et al. “Photorealistic images of objects in effective negative-index materials”. In: *Opt. Express* 14.5 (2006), pp. 1842–1849.

[22] John B Pendry and David R Smith. “Reversing light with negative refraction”. In: *Physics today* 57 (2004), pp. 37–43.

[23] Viktor A Podolskiy and Evgenii E Narimanov. “Strongly anisotropic waveguide as a nonmagnetic left-handed system”. In: *Physical Review B* 71.20 (2005), p. 201101.

[24] Alexander Poddubny et al. “Hyperbolic metamaterials”. In: *Nature Photonics* 7.12 (2013), p. 948.

[25] Yu Guo et al. “Applications of hyperbolic metamaterial substrates”. In: *Advances in OptoElectronics* 2012 (2012).

[26] Zubin Jacob et al. “Engineering photonic density of states using metamaterials”. In: *Applied physics B* 100.1 (2010), pp. 215–218.

[27] Xiaodong Yang et al. “Experimental realization of three-dimensional indefinite cavities at the nanoscale with anomalous scaling laws”. In: *Nature Photonics* 6.7 (2012), p. 450.

[28] Jyotirmayee Kanungo and Joerg Schilling. “Experimental determination of the principal dielectric functions in silver nanowire metamaterials”. In: *Applied Physics Letters* 97.2 (2010), p. 021903.

[29] Ivan V Iorsh et al. “Hyperbolic metamaterials based on multilayer graphene structures”. In: *Physical Review B* 87.7 (2013), p. 075416.

[30] Abbas El Gamal and Helmy Eltoukhy. “CMOS image sensors”. In: *IEEE Circuits and Devices Magazine* 21.3 (2005), pp. 6–20.

[31] Junichi Nakamura. *Image sensors and signal processing for digital still cameras*. CRC press, 2017.

[32] Bryce E Bayer. *Color imaging array*. US Patent 3,971,065. 1976.

[33] Qin Chen et al. “CMOS photodetectors integrated with plasmonic color filters”. In: *IEEE Photonics Technology Letters* 24.3 (2012), pp. 197–199.

[34] Yu Horie et al. “Visible wavelength color filters using dielectric subwavelength gratings for backside-illuminated CMOS image sensor technologies”. In: *Nano letters* 17.5 (2017), pp. 3159–3164.

[35] S. P. Burgos, S. Yokogawa, and H. A. Atwater. “Color imaging via nearest neighbor hole coupling in plasmonic color filters integrated onto a complementary metal-oxide semiconductor image sensor”. In: *ACS Nano* 7 (2013), pp. 10038–10047.

[36] URL: `http://www.bigshotcamera.com/learn/image-sensor/sensing-color`.

[37] Haida Liang. “Advances in multispectral and hyperspectral imaging for archaeology and art conservation”. In: *Applied Physics A* 106.2 (Feb. 2012), pp. 309–323.

[38] Hans Grahn and Paul Geladi. *Techniques and applications of hyperspectral image analysis*. John Wiley & Sons, 2007.

[39] Nahum Gat. “Imaging spectroscopy using tunable filters: a review”. In: *Wavelet Applications VII*. Vol. 4056. International Society for Optics and Photonics. 2000, pp. 50–65.

[40] Raffaele Pizzolante and Bruno Carpentieri. “Visualization, band ordering and compression of hyperspectral images”. In: *Algorithms* 5.1 (2012), pp. 76–97.

[41] Alexander FH Goetz et al. “Imaging spectrometry for earth remote sensing”. In: *Science* 228.4704 (1985), pp. 1147–1153.

[42] AC Goldberg, B Stann, and N Gupta. *Multispectral, hyperspectral, and three-dimensional imaging research at the US Army research laboratory*. Tech. rep. ARMY RESEARCH LAB ADELPHI MD, 2003.

[43] B Aalderink et al. "Clearing the image: A quantitative analysis of historical documents using hyperspectral measurements". In: *37th AIC* (2009).

[44] Dmitry Yudovsky et al. "Monitoring temporal development and healing of diabetic foot ulceration using hyperspectral imaging". In: *Journal of biophotonics* 4.7-8 (2011), pp. 565–576.

[45] Matthew E Martin et al. "Development of an advanced hyperspectral imaging (HSI) system with applications for cancer detection". In: *Annals of biomedical engineering* 34.6 (2006), pp. 1061–1068.

[46] Guolan Lu and Baowei Fei. "Medical hyperspectral imaging: a review". In: *Journal of biomedical optics* 19.1 (2014), p. 010901.

[47] AA Gowen et al. "Hyperspectral imaging–an emerging process analytical tool for food quality and safety control". In: *Trends in Food Science & Technology* 18.12 (2007), pp. 590–598.

[48] Gemma Payne et al. "Applying visible hyperspectral (chemical) imaging to estimate the age of bruises". In: *Medicine, science and the law* 47.3 (2007), pp. 225–232.

[49] GJ Edelman et al. "Hyperspectral imaging for non-contact analysis of forensic traces". In: *Forensic science international* 223.1-3 (2012), pp. 28–39.

Chapter 2

OPTICAL MAGNETISM IN PLANAR METAMATERIAL HETEROSTRUCTURES

2.1 Introduction

In the optical spectral range, the magnetic response of most materials, given by the magnetic permeability μ, is generally weak. This is famously expressed by Landau *et al*: "there is no meaning in using the magnetic susceptibility from the optical frequencies onward, and in discussing such phenomena, we must put μ = 1"[1]. However, in this range , materials possess a diverse range of dielectric properties, expressed through the dielectric permittivity ϵ, which can be positive, negative, or zero. The weak magnetic response in natural materials has motivated a search for structures and systems that may exhibit magnetic properties through non-natural means. Metamaterials, for example, possess artificial magnetism through engineered displacement and conduction currents generated when the structures are illuminated with electromagnetic fields[2]. However, until now, magnetic metamaterials have required complex resonant geometries[2–4], such as arrays of paired thin metallic strips[5, 6], split-ring resonators [7–9], and fishnet metamaterials[10]– structures that require sophisticated fabrication techniques at optical frequencies.

In contrast to their magnetic properties, the dielectric behavior of metamaterials can be engineered in simple planar configurations of layered media. These heterostructures of alternating metallic and dielectric layers, termed hyperbolic metamaterials (HMMs), have been intensely explored in the last decade[11–13] due to their anisotropic dielectric response. This peculiar dielectric response manifests in the hyperbolic dispersion for transverse magnetic (TM) waves (i.e., $\mathrm{k} \cdot \mathrm{H} = 0$ where $\mathrm{k} \cdot \mathrm{E} \neq 0$) leading to interesting phenomena such as negative refraction[11, 14–18] without the need of a negative refractive index, hyper-lensing[19], extreme enhancement in the density of optical states[13], and interface-bound plasmonic modes[20–25].

Due to the their weak magnetic response, all the interesting physics and applications for layered HMMs have been limited to TM polarization. Phenomena related to transverse electric (TE) polarized waves (i.e., $\mathrm{k} \cdot \mathrm{E} = 0$, whereas $\mathrm{k} \cdot \mathrm{H} \neq 0$) has

remained largely unexplored, because the effective magnetic permeability in planar layered media has been widely assumed to be unity[11–13, 26]. Utilizing the effective magnetic response (i.e., μ_{eff} = diag{μ_o,μ_o,μ_e}≠I) is necessary to harness and control arbitrary light polarization (TE and TM). A material where the combined components of the dielectric permittivity and magnetic permeability tensors are less than zero ($\epsilon_o\epsilon_e$ < 0 and $\mu_o\mu e$ < 0) could allow polarization independent negative refraction (Fig. 2.1a) and excitation of TE surface waves (Fig. 2.1b), the magnetic counterpart of surface plasmon polaritons (SPPs). Furthermore, gaining control over the magnetic permeability in planar systems can yield impedance-matched epsilon-and-mu-near-zero (EMNZ) optical responses (Fig. 2.1c)[27]. Although it is straightforward to tailor the permittivity to cross zero in planar metamaterials[28], a simultaneously EMNZ metamaterial at optical frequencies has not yet been demonstrated.

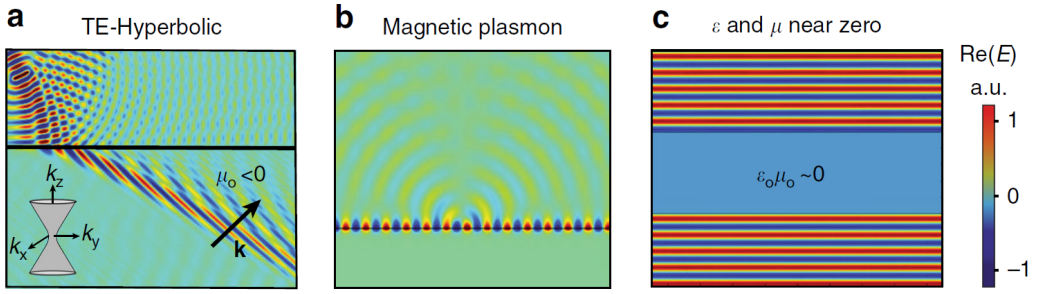

Figure 2.1: (a) A Transverse electric (TE) negative refraction of phase in a hyperbolic metamaterial with μ_o < 0 and μ_e > 0. The arrow indicates the direction of wavevector and the black line indicates the interface between air and the hyperbolic metamaterial. Inset: 3D isofrequency diagram for μ_o < 0, μ_e > 0. (b) TE magnetic plasmon at the interface between air and magnetic material (μ < 0), analogous to transverse magnetic polarized surface plasmon polaritons (ϵ < 0). c, ϵ, and μ near zero (EMNZ): a field propagating inside an EMNZ slab with vanishing phase advance

In this work, we proposed a concept for tailoring the effective magnetic response within planar, unpatterned, one-dimensional (1D) multilayer structures. In contrast to previous generations of magnetic metamaterials with complex three-dimensional structures such as split-ring resonators[7–9], fishnet structures[10], and nanoparticles[29, 30], pattern-free multilayers are readily realizable with lithography-free thin-film deposition, greatly simplifying fabrication. We show theoretically and experimentally that the magnitude and sign of the permeability tensor may be engineered at will, enabling observation and use of TE polarization related phenomena

in simple layered structures. We further identify implications that are associated with the observed artificial magnetism.

2.2 Induced Magnetic Dipoles in Planar Systems

A circulating electric current can create a magnetic dipole and is the key to inducing magnetism in magnet-free systems. Based on this principle, induction coils generate and induce magnetic flux, allowing for the manipulation of magnetic fields at radio frequencies. The same concept is widespread in metamaterials design[31, 32] where metamaterial elements are shaped to produce a circulating current flow, which in turn induces magnetic dipoles. Dielectric nanorods[33, 34] and nanoparticles[29, 30, 35–38] can be used as the building blocks for two- and three-dimensional magnetic metamaterial structures, respectively (Figs. 2.2a, b). The magnetic response of these arrangements is sometimes incorporated into an equivalent, alternative, spatially dispersive permittivity. Although this is, in principle, always possible[1, 39, 40], descriptions utilizing a permittivity ϵ and a permeability μ allows for physical intuition and reduces complexity, especially when it is straightforward to relate the dielectric (or magnetic) response with physical macroscopic electric (or magnetic) moments. This can be particularly useful for the uniaxial planar and unpatterned multilayers, discussed in this chapter.

The design parameters for an enhanced magnetic response in planar metamaterials can be determined by first considering a single subwavelength dielectric slab of refractive index n_{diel} and thickness d. When illuminated at normal incidence (z direction in Fig. 2.2c), the displacement current $J_d = i\omega\epsilon_o(n_{diel}^2 - 1)E$ induces a macroscopic effective magnetization $M_{eff} = \frac{1}{2}\mu_o \int (r \times J_d) \cdot dS$[1, 33, 41]. By averaging the magnetic field, $H_{avg} = \int_{d/2}^{d/2} H(z)dz$, we use $\mu_{eff} \approx 1 + M_{eff}/(\mu_o H_{avg})$ to obtain an empirical closed-form expression for the magnetic permeability:

$$\mu_{eff} \approx 1 - \frac{n_{diel}^2 - 1}{2n_{diel}^2}\left(-1 + \frac{n_{diel}\pi d/\lambda}{\tan(n_{diel}\pi d/\lambda)}\right) \tag{2.1}$$

By setting $n_{diel} = 1$, we recover the unity magnetic permeability of free space. From Eq. (2.1), we see that μ_{eff} diverges when tan $(n_{diel}\pi d/\lambda) = 0$. This yields a magnetic resonant behavior at free-space wavelengths $\lambda = n_{diel}d/\rho$, where $\rho = 1$, 2, ... At these wavelengths, the displacement current distribution is anti-symmetric, as shown in Fig. 2.2d for $\rho = 1, 2$. This anti-symmetric current flow closes a loop in y = $\pm\infty$ and induces a magnetization M_{eff} that is opposite to the magnetic field

of the incident wave (Fig. 2.2c), leading to a magnetic resonance. Via Eq. (1) the design parameters for enhanced magnetic response can be estimated.

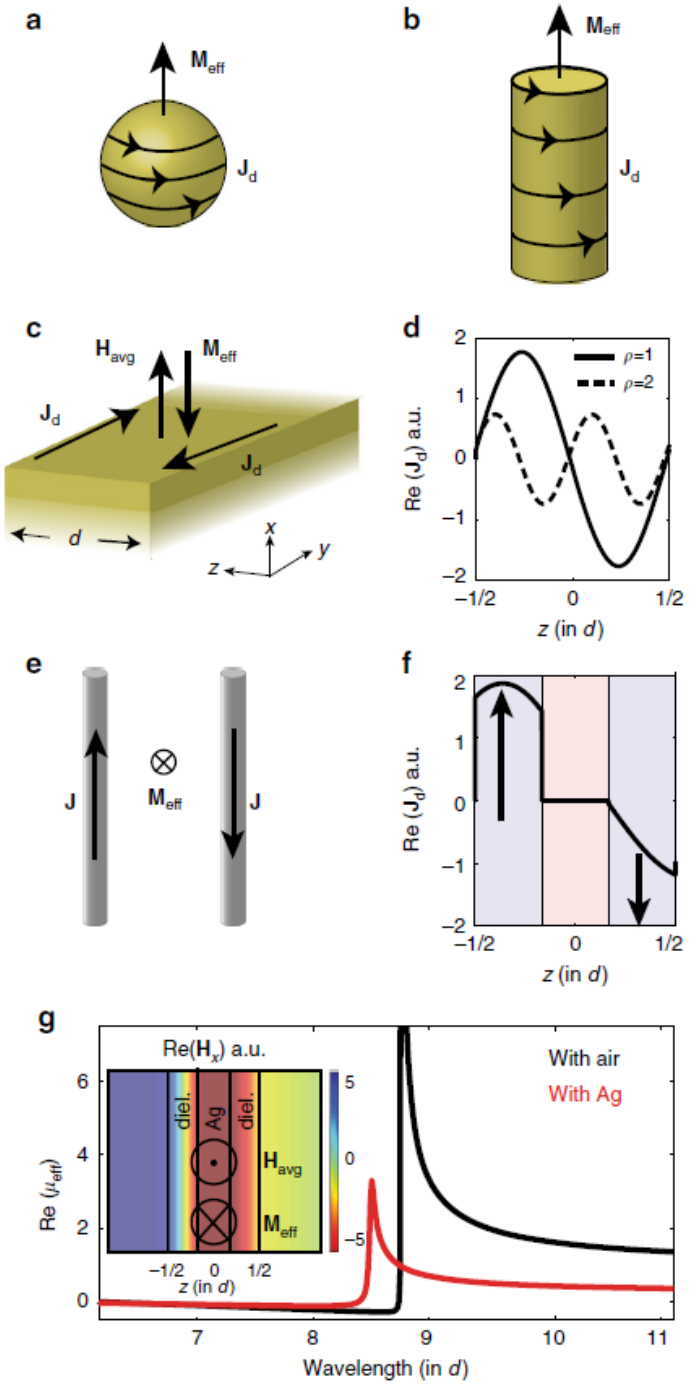

Figure 2.2: A circulating current flow Jd induces a magnetization Meff in all three cases:(a) dielectric nanoparticles (3D metamaterials), (b) dielectric nanorods (2D metamaterials), and (c) 1D dielectric slabs. H_{avg} is the average magnetic field, which faces in the direction opposite of M_{eff}. (d) Displacement current distribution at resonance for $\rho = 1$, $\rho = 2$, for a 90 nm slab of refractive index $n_{diel} = 4.5$. (e) Two infinite wires carrying opposite currents are equivalent to (f) two dielectric layers (blue shaded regions) separated by air (pink shaded region) in terms of their current distribution. Arrows in (f) indicate the direction of J_d, which is anti-symmetric at resonance. (g) Effective permeability for two dielectric layers separated by air and silver. Inset: tangential magnetic field distribution at resonance; average magnetic field is opposite to M_{eff}.

In the long-wavelength limit, only the fundamental and second order resonances, $\lambda = n_{diel}d$, $n_{diel}d/2$, play significant roles. In the visible and near-infrared parts of the spectrum and slab layer thicknesses on the order of 10–100 nm, dielectric indices higher than $n_{diel} \approx 2$ are required for strong magnetic effects[42]. The same principle applies for grazing incidence, in which case the displacement current induces a magnetic response in the extraordinary or, out-of-plane (z) direction. As indicated by Fig 2.2(d), a circular shape designed to support a closed current loop is not a requirement for magnetic metamaterials. A planar structure suffices, for which the current loop closes in ± infinity.

In order to make this magnetic response significant, we extend this principle to multilayer configurations. We first examine the case of two infinite parallel wires in air, carrying opposite currents (Fig. 2.2e). Their net current distribution induces a magnetic moment that scales with their distance, as dictated by $M_{eff} \propto \mathrm{r} \times J$. This is directly equivalent to a layered configuration composed of two high-index dielectrics separated by air. Their displacement current distribution can be anti-symmetric on resonance, as shown in Fig. 2.2(f). By calculating their magnetic permeability μ_{eff}, we confirm the magnetic character of this arrangement. As shown with the black curve in Fig. 2.2(g), μ_{eff} strongly deviates from unity.

The planar geometry does not require that the two high-index layers be separated by air; any sequence of alternating high-low-high refractive index materials will induce the same effect. For example, replacing the air region with a layer of metal, with $n_{metal} < 1$ at visible wavelengths, does not dramatically change the magnetic response. The red curve in Fig. 2.2 (g) demonstrates this using silver as the low index separation layer. Therefore, in contrast to the gigahertz regime, at optical frequencies, metals do not contribute significantly to the magnetic response in this planar configuration. As shown by the magnetic field distribution shown in the inset of Fig. 2.2(g), the average magnetic field faces in the direction opposite to the magnetization, expressing a negative response for the dielectric/silver unit cell

2.3 Combining hyperbolic dielectric and magnetic properties

In addition to the magnetic response described in the previous section, multilayer systems composed of metals and dielectrics also possess a distinct hyperbolic dielectric response for TM polarization. These systems are uniaxially anisotropic and, at wavelengths large compared to the unit cell, they exhibit an in-plane metallic re-

sponse ($\epsilon_o < 0$) due to the metallic layers, while $\epsilon_e > 0$[11]. If the dielectric layers are high-index materials capable of supporting strong displacement currents at optical frequencies, it is possible to induce a significant additional magnetic response in planar dielectric/metal HMMs. Previously reported dielectric/metal HMMs have primarily featured dielectric layers with lower-refractive indices, such as LiF[43], Al_2O_3 [26, 44, 45], and TiO_2[13]. Figure 3 shows that, for layer thicknesses below 50 nm, these lower-index dielectric/metal systems exhibit magnetic resonances in the ultraviolet (UV)-short wavelength visible regime.

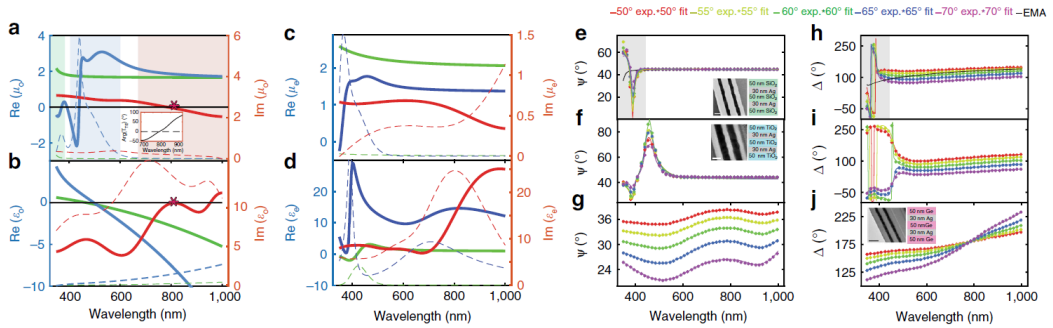

Figure 2.3: Experimentally determined (a) μ_o, (b) ϵ_o, (c) μ_e, (d) ϵ_o for SiO_2/Ag-green, TiO_2/Ag-blue, Ge/Ag-red metamaterials. Shaded regions in (a) indicate the regime of magnetic resonances in μ_o for the studied metamaterials. Solid lines represent real parts while dashed lines represent imaginary parts. Asterisks in (a) and (b) indicate the ϵ_o and μ_o near zero (EMNZ) wavelength for the Ge/Ag metamaterial. The EMNZ condition is confirmed by a vanishing phase of the transmission coefficient at the EMNZ wavelength, shown in the inset of (a). (e)–(g) and (h)–(j) show the agreement between raw experimental data, Ψ and Δ respectively (which are the conventional ellipsometric angles), and the ellipsometric fitting, for the SiO_2/Ag metamaterial in (e) and (h), for the TiO_2/Ag metamaterial in (f), (i), and for the Ge/Ag metamaterial in (g), (j). Shaded regions in (e), (h) emphasize the disagreement between experimental data and the effective medium approximation (EMA). Insets in (e), (f), (j) show TEM images of the fabricated samples. The scale bar is 50 nm for (e), (f) and 100 nm for (j)

Previous approaches used effective medium approximations (EMAs), such as the Maxwell Garnett theory[46], to describe the dielectric response of dielectric/metal HMMs. These EMAs *a priori* assume a unity magnetic permeability along all coordinate directions. However, a uniaxial system is most generally described in terms of both an effective permittivity tensor $\epsilon_{eff} = \text{diag}\epsilon_o, \epsilon_o, \epsilon_e$ and an effective permeability tensor $\mu_{eff} = \text{diag}\mu_o, \mu_o, \mu_e$. In order to capture the magnetic dipole moments in multilayer structures, instead of an EMA an exact parameter retrieval that relaxes the $\mu_{eff} = I$ assumption is used[47].

2.4 Experimental Verification

Fabricating Multilayer Structures

Each of the three different metamaterials were fabricated using electron-beam evaporation. To ensure the layer thicknesses were well controlled and each interface had the same morphology, the SiO_2/Ag stack was deposited on a cleaned Ge substrate, to prevent any native oxide on a Si chip from contributing to the thickness of the first deposited layer of SiO_2. Likewise, the Ge/Ag film was deposited on a Si substrate so there would be good index contrast between the substrate and the first layer. The TiO_2 sample was also deposited on a Ge substrate because the cleaning chemicals are not as scary. The substrates were all cleaned and stripped of their oxides using the methods described in Chapter 6.1 of this thesis. Once cleaned, all substrates for all samples (metamaterials and single layers) were transferred in a vacuum container to an ALD, where they were immediately deposited with 2 nm (20 cycles) of Al_2O_3 to prevent native oxides from forming on the substrates.

All samples were deposited in the same chamber, and no structure was removed from vacuum before all layers were deposited to insure clean, oxide-free interfaces. Because of the columnar morphology of Ag when deposited on SiO_2[48], a 2 nm AgO seed layer was deposited and reduced under vacuum before the deposition of the remaining 28 nm to produce smoother Ag films[49]. To maintain consistency, this method was used even when the underlying layer was not SiO_2. The exact deposition parameters of this method are listed in Chapter 6.2 and are discussed in more detail in the Experimental Verification section in Chapter 3.

In the final metamaterial structures, the target thickness for each Ag layer was 30 nm and the target thicknesses for the Ge, TiO_2, and SiO_2 layers was 40 nm thick. The thicknesses of all films were determined using transmission electron microscopy (TEM). While the Ag seed layer method reduced the rms surface roughness of the deposited Ag films to 2.3 nm, the roughness in each layer compounded in the SiO_2 and TiO_2 stacks, as shown in the insets in Figure 2.3 (e), (f), and (j) for SiO_2/Ag, TiO_2/Ag, and Ge/Ag respectively.

Measurement and Analysis of Experimental Structures

In addition to the deposited metamaterials, films of all constituent materials were also deposited individually using the above methods to measure the optical constants of the constituent layers with spectroscopic ellipsometry. Using thicknesses

from TEM images and the optical data, the layered metamaterials could be homogenized by assigning them effective parameters ϵ_{eff} and μ_{eff} [47], while still taking into account fabrication imperfections. Ellipsometric measurements were then performed on the full metamaterials. The experimental data was fit with the effective parameters ϵ_o, ϵ_e, μ_o, and μ_e in a uniaxial and Kramers–Kronig consistent model, while total metamaterial thickness is held to the value determined through TEM. The fitting is over-determined: the number of incident angles exceeds the total number of fitted parameters.

The fabricated metamaterials are composed of alternating layers of SiO_2/Ag, TiO_2/Ag, and Ge/Ag (TEM images and schematics in insets of Figs. 2.3(e),(f), and (j) respectively). The indices of the selected dielectric materials at optical frequencies are $n_{SiO_2} \approx 1.5$, $n_{TiO_2} \approx 2$, and $n_{Ge} \approx 4$˘4.5. Figure 2.3(a) shows that increasing the dielectric index redshifts the magnetic resonance in the ordinary direction μ_o, indicating the SiO_2/Ag metamaterial supports a magnetic resonance in the long-wavelength UV regime (300 nm). In contrast, the TiO_2/Ag and Ge/Ag metamaterials exhibit resonances in the blue (450 nm) and red (800 nm) parts of the spectrum, respectively. The enhanced absorption in Ge at optical frequencies leads to considerable broadening of the Ge/Ag metamaterial magnetic resonance, yielding a broadband negative magnetic permeability for wavelengths above 800 nm. As expected, the losses in μ_o are increased at the magnetic resonance frequency for all investigated heterostructures, similar to previous reports on artificial magnetism with split-ring resonators and other magnetic metamaterials[50–52].

The presence of Ag induces a negative ordinary permittivity ϵ_o (Fig. 3b), which, for the Ge/Ag metamaterial, becomes positive above 800 nm due to the high-index of Ge. ϵ_o crosses zero at 800 nm, similar to μ_o, as emphasized with the asterisks in Figs. 2.3(a) and (b). Therefore, the Ge/Ag metamaterial exhibits an EMNZ response at optical frequencies. The EMNZ condition can be confirmed by transfer-matrix analytical calculations of the physical multilayer structure. As shown in the inset of Fig. 3(a), the phase of the transmission coefficient vanishes at the EMNZ wavelength, demonstrating that electromagnetic fields propagate inside the metamaterial without phase advance[27].

By comparing μ_o and μ_e in Figs. 2.3(a) and (c) respectively, it can be inferred that increasing the dielectric index leads to enhanced magnetic anisotropy. The

parameter μ_e only slightly deviates from μ_o for the SiO_2/Ag metamaterial and sees a larger deviation in the TiO_2/Ag structure. For the Ge/Ag metamaterial, μ_e remains positive beyond 800 nm, while $\mu_o < 0$, indicating magnetic hyperbolic response for TE polarization. All three heterostructures exhibit hyperbolic response for TM polarization, with $\epsilon_o < 0$ and $\epsilon_e > 0$ (Figs. 3(b), (d)). Thus, the Ge/Ag metamaterial possesses double hyperbolic dispersion.

Figures 3(e)–(j) demonstrate the excellent agreement between the fitting and raw experimental data, where the parameters Ψ and Δ correspond to the conventional ellipsometric angles. Figs. 2.3(e) and (h) provide a Maxwell Garnett EMA-based fit for the SiO_2/Ag metamaterial, and the EMA fails to reproduce the experimentally measured magnetic permeability resonances in both Ψ and Δ (gray-shaded regions in Figs. 3(e), (h)). Similar EMA-based fits for the TiO_2/Ag and Ge/Ag metamaterials lead to large disagreement with the experimental data across the visible and infrared parts of the spectrum and are, thus, omitted. This disagreement is expected, as the EMA approach is based on the assumption that the electric field exhibits negligible or no variation within the lattice period, which does not apply to high-index dielectric layers.

It should be noted that the dielectric hyperbolic response $\epsilon_o\epsilon_e < 0$ is broadband in planar systems, as seen in Figs. 2.3(b) and (d). In contrast, the magnetic permeabilities deviate from unity in a resonant manner along both coordinate directions μ_o and μ_e, thereby making TE polarization-based phenomena more narrowband in nature.

2.5 Beyond $\mu_{eff} \neq 1$ and TE polarization effects

In the previous sections we established, theoretically and experimentally that dielectric/metal layered systems may be described with an effective magnetic permeability that deviates from unity across all coordinate directions. The purpose of introducing this parameter is to build a simple and intuitive description for understanding and predicting new phenomena, such as TE polarization response in planar systems. This section will discuss how the demonstrated non-unity and, in particular, the negative and anisotropic magnetic response manifests the characteristics of TE-polarized propagating modes (Fig. 2.4) and surface waves (Fig. 2.5).

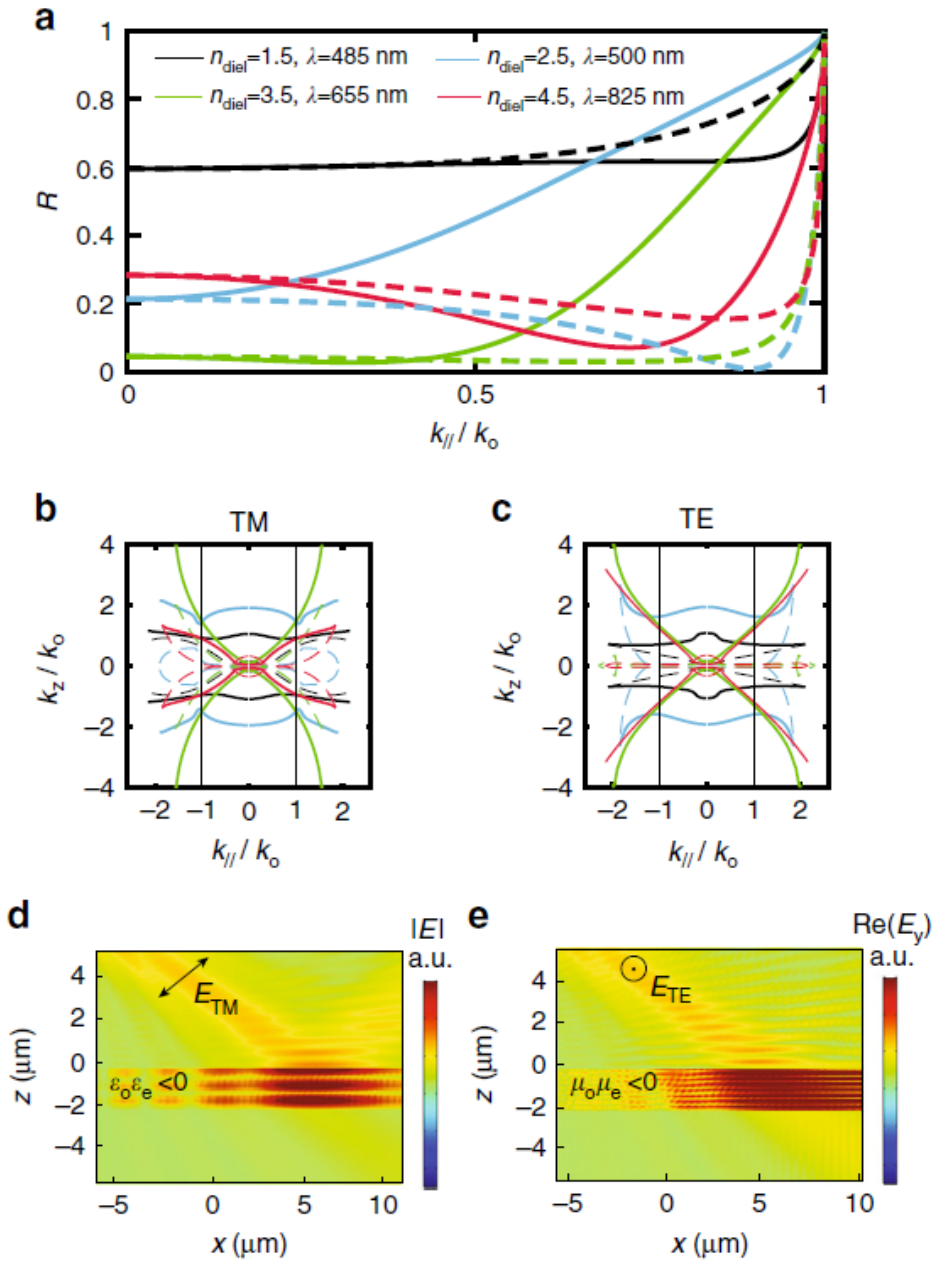

Figure 2.4: Analytical calculations of (a) reflectance and (b), (c) isofrequency diagrams for a metamaterial consisting of five alternating layers of dielectric n_{diel}: 55 nm and Ag: 25 nm. Solid lines in (a) correspond to TE polarization whereas dashed lines correspond to TM polarization. Solid lines in (b) and (c) correspond to the real parts, whereas dashed lines correspond to the imaginary parts. Vertical black lines in (b) and (c) indicate the maximum free space in-plane wavenumber $k_{|}| = k_o$. The color code is consistent for (a)–(c). (d) and (e) show the results of a numerical simulation of a fifty-five layers dielectric (n_{diel} = 4)/Ag multilayer metamaterial. The surrounding medium has index n_{sur} = 1.55, allowing coupling of high-k modes. The number of layers was increased to allow for clear visibility of the field localization inside the structure. Strong field localization is the consequence of (d) dielectric hyperbolic dispersion for TM polarization ($\epsilon_o\epsilon_e < 0$) and (e) magnetic hyperbolic dispersion for TE polarization ($\mu_o\mu_e < 0$)

We use an example system of dielectric/silver alternating layers, similar to the one investigated experimentally. The calculations and full-wave simulations presented here are performed in the actual, physical, multilayer geometry (Figs. 2.4(a), (d), (e), and 2.5) and compared with the homogenous effective slab picture (ϵ_{eff}, μ_{eff} Figs 4(b) and (c)). This helps assess the validity of our model and emphasize the physicality of the magnetic resonances.

Transfer-matrix calculations were performed for the example multilayer metamaterial and the angle dependence for TE and TM reflectance is shown in Fig. 2.4(a). The strong angle dependence for TM polarization is well understood in the context of an equivalent homogenous material with anisotropic effective dielectric response $\epsilon_o\epsilon_e < 0$. Bulk TM modes experience dispersion

$$\frac{k_x^2 + k_y^2}{\epsilon_e(\omega, k)\mu_o(\omega, k)} + \frac{k_z^2}{\epsilon_o(\omega, k)\mu_o(\omega, k)} = k_o^2 \tag{2.2}$$

where $k_o = \omega/c$. This dispersion is hyperbolic, as shown by the isofrequency diagrams in Fig 2.4(b). Losses and spatial dispersion perturb the perfect hyperbolic shape[12]. In contrast to the TM modes, TE bulk modes interact with the magnetic anisotropy through the dispersion equation

$$\frac{k_x^2 + k_y^2}{\epsilon_o(\omega, k)\mu_e(\omega, k)} + \frac{k_z^2}{\epsilon_o(\omega, k)\mu_o(\omega, k)} = k_o^2 \tag{2.3}$$

which is plotted in Fig 2.4(c). For small wavenumbers ($k_{||}/k_o < 1$) and small dielectric indices n_{diel}, the isofrequency diagrams are circular, therefore isotropic. This agrees with our experimental results: as shown in Figs. 2.3(a) and (c), for the SiO_2/Ag metamaterial, the ordinary and extraordinary permeabilities do not dramatically deviate from each other. Increasing the dielectric index opens the isofrequency contours, due to enhanced magnetic response in the ordinary direction (μ_o), which leads to magnetic anisotropy. Note that the displayed wavelengths are selected at resonances of μ_o. Open TE polarization isofrequency contours for $n_{diel} \leq 2$ are also consistent with the experimental results. As shown in Fig. 2.3 for the TiO_2 and Ge-based metamaterials, increasing n_{diel} enhances the ansisotropy. This also aligns with the picture of the physical multilayer structure, as shown in Fig. 2.4(a), where the TE reflectance exhibits extreme angle dependence for increasing dielectric index. Strikingly, we observe a Brewster angle effect for TE polarization, which is unattainable in natural materials due to unity magnetic permeability at optical frequencies[53].

An open isofrequency surface can lead to enhancement in the density of optical states relative to free space. Physically, this may yield a strong interaction between incident light and a hyperbolic structure, and enhanced absorption when large wavenumbers can couple in from the surrounding medium[54, 55]. So far, only TM polarization has been considered able to experience this exotic hyperbolic response in planar dielectric/metal metamaterials, due to $\epsilon_o \epsilon_e e < 0$ [12, 13, 26]. Based on the open isofrequency surfaces for both TE and TM polarizations in Figs. 2.4(b) and (c), a high-index dielectric/metal multilayer metamaterial may exhibit distinct frequency regimes of double hyperbolic-like response (as in simultaneously TE and TM polarization). To confirm this, finite element simulations of a (n_{diel} = 4)/Ag multilayer metamaterial were performed for both linear polarizations in a surrounding medium with index nsur = 1.55, which allows for coupling to larger wavenumbers. To facilitate visualizing the interaction between the fields and the metamaterial, we consider a thick structure consisting of fifty-five layers. Without loss of generality, we carry out the simulation in the low loss limit to reveal the physics while avoiding side-effects from losses. Figure 2.4(d) demonstrates the well-known TM hyperbolic response, where the electric field is strongly localized within the multilayer. Switching the polarization to TE (Fig. 2.4(e)), we observe similar hyperbolic behavior. This result cannot be attributed to the dielectric anisotropic response, because the electric field only experiences the in-plane dielectric permittivity ϵ_o (Eq. (2.3)). The TE enhanced absorption is associated with the $\mu_o \mu_e < 0$ condition[56], and the number of TE modes supported by this metamaterial in this frequency range is dramatically increased.

Surface wave propagation can also be investigated in the layered dielectric n_{diel}/Ag metamaterial by utilizing the transfer matrix mode condition $m_{11} = 0$ [57], which can be implemented numerically using the reflection pole method[58]. In order to ensure interface-localized propagation with fields decaying into air and in the metamaterial, we impose an additional constraint for the waves to be located in the optical band gaps of both bounding media.

Figure 2.5(a) displays the dispersion for TM polarization. The identified surface waves bear similarity to typical surface plasmon polaritons (SPPs) on metallic interfaces[22, 59] and to plasmonic waves in dielectric/metal waveguides and systems[24]. Their plasmonic nature is evident as their dispersion asymptotically approaches the surface plasma frequency, similar to SPPs. Fig. 2.5(c) compares

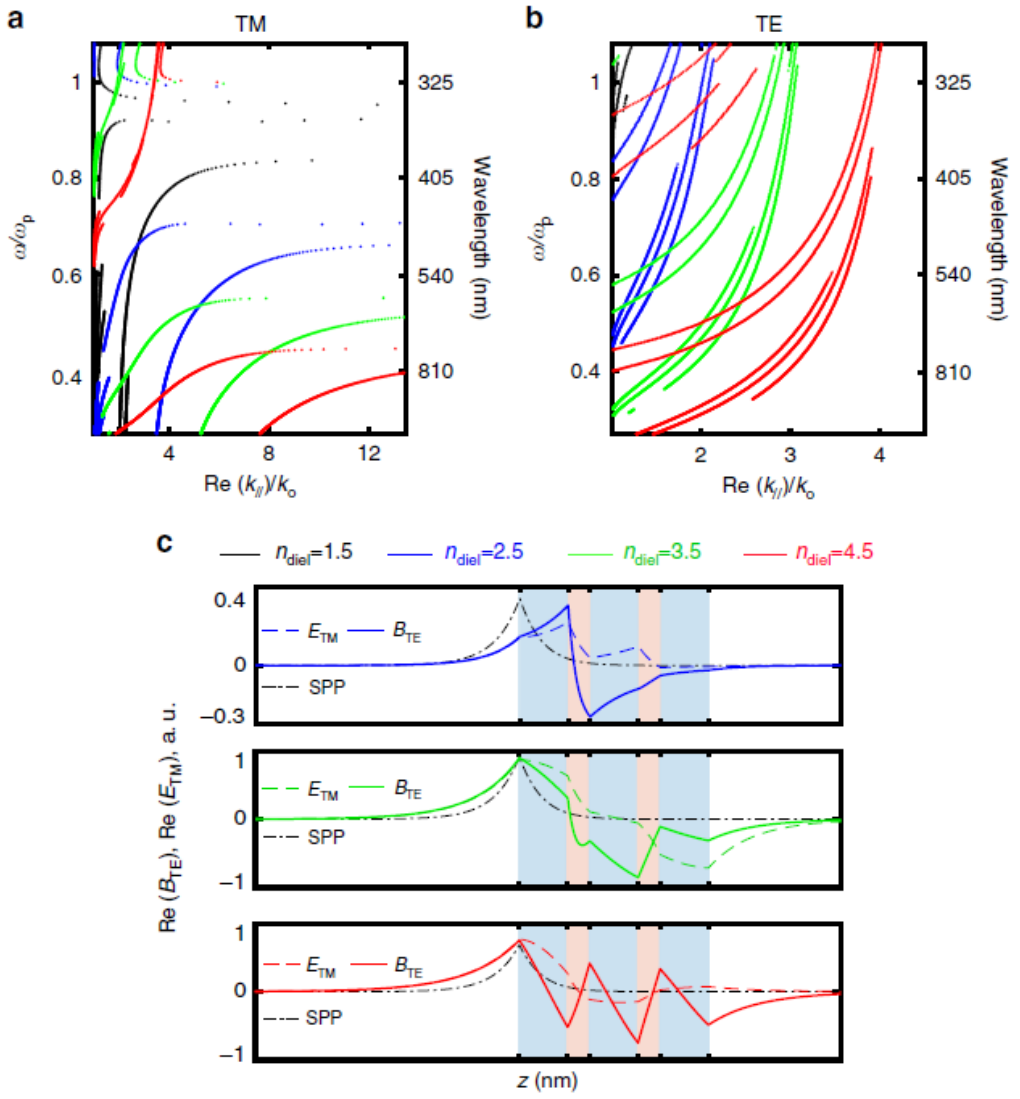

Figure 2.5: (a) TM and (b) TE surface wave dispersion for a metamaterial consisting of five alternating layers of dielectric n_{diel}: 55 nm and Ag: 25 nm. (c) Field profiles (incidence from the left) and comparison with a surface plasmonic polariton (SPP) on an equivalent Ag slab (black dotted line). Calculations in (c) correspond to a wavelength of 620 nm for $n_{diel} = 2.5$, 880 nm for $n_{diel} = 3.5$ and 1100 nm for $n_{diel} = 4.5$. Blue shaded regions in (c) indicate dielectric layers and pink shaded regions indicate Ag

the surface wave field distribution (dashed lines) to SPPs on an equivalent silver slab (black dotted lines). Such TM surface waves on metamaterial interfaces are often associated with an effective negative dielectric response[20, 21, 25]. This is consistent with the effective dielectric and magnetic model experimentally above, where Fig. 2.3(b) shows the ordinary permittivity is negative $\epsilon_o < 0$.

Performing the same analysis for TE polarized waves, TE surface-bound modes were also confirmed to exist (Fig. 2.5(b)). Their dispersion is parabolic, resembling that of Tamm states in photonic crystals[25, 60]. However, here it is shown that they also exist in the subwavelength metamaterial limit and can coexist with typical TM plasmonic surface waves. TE polarized Tamm states have been previously associated only qualitatively with some arbitrary negative net magnetic response[25]. Here this hypothesis is confirmed and explicitly connects the dispersion of Tamm states in planar metamaterials to experimentally measured values of magnetic permeabilities (Fig. 2.3). This analysis identifies their physical origin in the strong displacement current supported in high-index dielectric layers with a loop-like distribution on resonance. These TE surface waves emerge in the visible regime for dielectric layers with refractive index $n_{diel} \leq 2$ (Fig. 2.5(b)), at frequencies where the metamaterial exhibits a negative effective magnetic response. For this reason, these states may be seen as magnetic plasmons. The frequency regimes in which double surface waves are supported demonstrate the possibility of exciting TM polarized plasmonic modes simultaneously with their TE counterparts in dielectric/metal pattern-free multilayers.

2.6 Relaxing the $\mu_{eff} = 1$ constraint

The most extensively used approach for describing the effective response of hyperbolic multilayer metamaterials is the Maxwell Garnett EMA[11] (and references therein)[12, 13]. Based on this approach, the in-plane dielectric permittivity is given by $\epsilon_{o,MG} = f\epsilon_m + (1-f)\epsilon_d$ and the out-of-plane extraordinary permittivity is $\epsilon_{e,MG}^{-1} = f\epsilon_m^{-1} + (1-f)\epsilon_d^{-1}$, where f is the metallic filling fraction[46], while μ_{eff} is *a priori* set to unity. Another common approach is the Bloch formalism, based on which, a periodic A-B-A-B... superlattice is described with a Bloch wavenumber[57]. This wavenumber is directly translated to an effective dielectric permittivity[61], while also assuming $\mu_{eff} = 1$. These approaches are useful and simple to use, however, they are both based on the assumption of an infinite and purely periodic medium, ignoring the finite thickness of realistic stacks.

Non-planar metamaterials are generally more structurally complex, such as split-ring resonators[7–9, 62], nanoparticles[30], and fishnet structures[63, 64]. These are modeled with exact S-parameter retrieval approaches[65, 66]. S-parameter retrievals solve the inverse problem of determining the effective dielectric permittivity and magnetic permeability, ϵ_{eff} and μ_{eff}, respectively, of a homogeneous slab with the

same scattering properties, namely transmission T and reflection R coefficients, as the arbitrary inhomogeneous, composite metamaterial system of finite thickness d.

By lifting the constraint of an infinite medium, both transmission T and reflection R coefficients can be computed and used in S-parameter approaches. This allows obtaining an effective wavenumber k_{eff} together with an effective impedance Z_{eff}[65, 66]. These parameters are then used to decouple the effective permittivity from the permeability through $k_{eff} = \sqrt{\epsilon_{eff}\mu_{eff}}\frac{\omega}{c}$ and $Z_{eff} = \sqrt{\frac{\mu_{eff}}{\epsilon_{eff}}}$. By contrast, Bloch-based approaches[57, 61] only consider a Bloch wavenumber K_{Bloch} (based on periodicity), with no other information available for allowing decoupling μ_{eff} from ϵ_{eff} . Both the Maxwell Garnett result[46] and its Bloch-based generalizations (for example[61]) are based on the assumption that $\mu_{eff} = 1$. A schematic comparison between the two approaches is shown in Figures 2.6(a) and (b).

Contrary to the extensive use of EMAs, we use the S-parameter approach to describe dielectric/metal multilayer metamaterials of finite thickness. By letting the magnetic permeability μ_{eff} be a free parameter, instead of *a priori* setting $\mu_{eff} = 1$, we obtain magnetic resonances at wavelengths where magnetic dipole moments occur, as demonstrated in Figures 2.2(f) and (g). This confirms the physicality of the non-unity μ; magnetic resonances arise at wavelengths where the system supports loop-like current distributions. By accounting for the uniaxial anisotropy in planar heterostructures, we obtain both the ordinary and the extraordinary permeabilities μ_o and μ_e, together with their dielectric permittivity counterparts, ϵ_o and ϵ_e. As a sanity check, we first consider homogeneous metallic and dielectric slabs with known dielectric permittivity $\epsilon_o = \epsilon_e$ and $\mu_o = \mu_o = 1$, which we recover upon application of our retrieval[47].

Another way to establish the validity of the effective parameters is to perform an impedance-matching sanity check in the low loss limit. Based on electromagnetic theory, the impedance of a structure at normal incidence, ($Z_{eff} = \sqrt{\frac{\mu_o}{\epsilon_o}}$), must be unity at transmittance $|T|^2$ maxima. As seen in Figure 2.6(c), the retrieved parameters ϵ_o and μ_o accurately describe the scattering properties of planar dielectric/metal arrangements of finite thickness. By contrast, not accounting for a magnetic permeability leads to inaccurate prediction of transmittance maxima. This is seen both by our S-retrieval-based approach while setting *a priori* the magnetic permeability to unity ($Z_{\mu_=1}$), and with the traditional EMA; both approaches fail to predict the

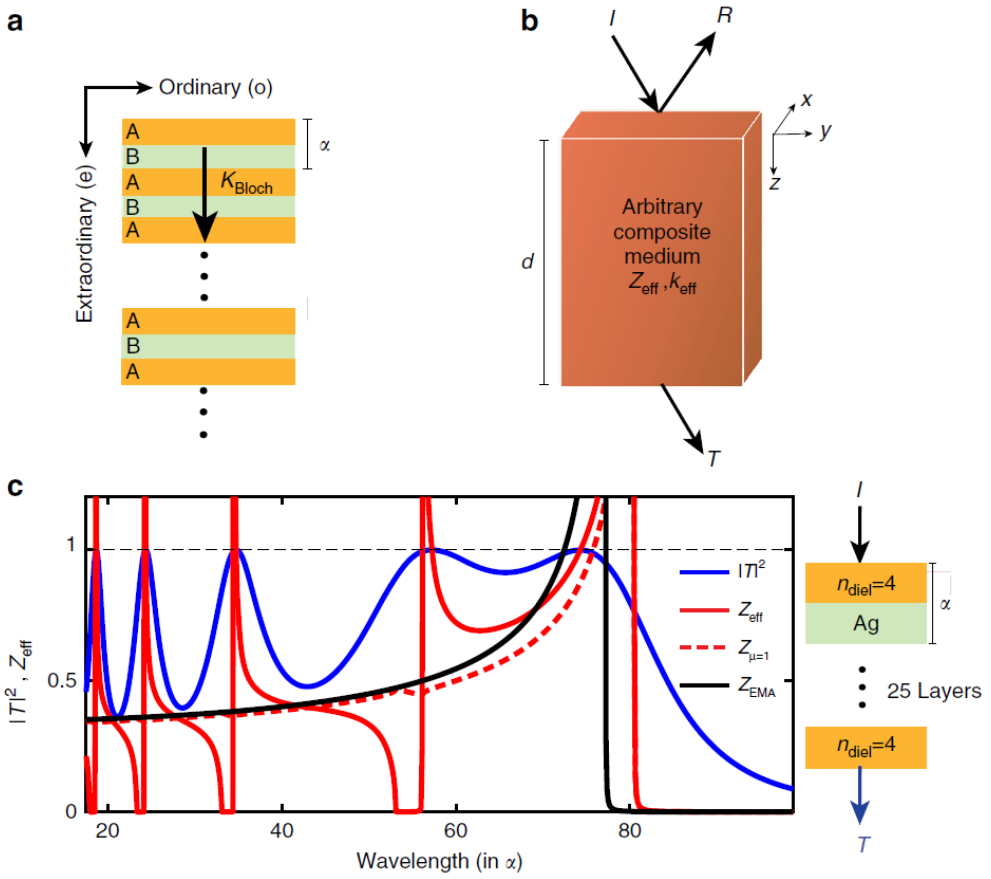

Figure 2.6: Comparison between effective medium theory (EMA) and Bloch approaches and S-parameter retrieval. (a) EMA and Bloch formalisms (for infinite periodic arrangements), α is the lattice period and K_{Bloch} is the Bloch wavenumber. (b) general concept of S-parameter retrievals that take finite total thickness d into account. T and R are the transmitted and reflected amplitudes and Z_{eff} and k_{eff} are the effective impedance and wavenumber. (c) Impedance-matching sanity check at normal incidence for a twenty-five layer dielectric/metal metamaterial, for $n_{diel} = 4$. The transmittance $|T|^2$ calculation (blue solid line) was performed with the transfer-matrix formalism[57] for the physical multilayer system in the lossless limit. The dielectric and magnetic effective model ($Z_{eff} = \sqrt{\frac{\mu_o}{\epsilon_o}}$) (red solid line) accurately captures the resonances unlike the non-magnetic approach $Z_{\mu_{eff}=1}$ (red dashed line) and the Maxwell Garnett EMA (black solid line)

resonances).

By sweeping the angle of incidence from 0 to 90 degrees, i.e., by varying the in-plane wavenumbers $k_{||}$, we obtain angle-independent, local material parameters for the systems we consider[47]. This makes ellipsometry a suitable method to experimentally characterize our metamaterials in terms of local material tensorial

parameters μ_{eff} and ϵ_{eff} . For larger $k_{||} \gg \frac{\omega}{c}$, dielectric/metal arrangements exhibit some degree of spatial dispersion, due to the plasmonic nature of the metallic layers[67]. This effect is distinct from the magnetic resonances we investigate, which are the result of induced magnetic dipole moments[2]. Spatial dispersion is fully accounted for in the results presented here. This is done by extending our previous approach[47] to consider as a free parameter not only the magnetic permeability, but also spatial dispersion in the form of wavenumber ($k_{||}$) dependence (see discussion pertaining to Figures 4(b) and (c)). Furthermore, as seen by the experimentally confirmed effective parameters discussed in Figure 3, all constituent permittivity and permeability components (ϵ_o, ϵ_e, μ_o, μ_e) are passive and causal and have positive imaginary parts with no antiresonance artifacts. Such artifacts are often associated with weak form of spatial dispersion (see[68] and discussion in[69] and[70] among others).

Other approaches are also able to capture this artificial magnetic response by accounting for an effective permeability in multilayer metamaterials. The general field averaging scheme introduced by Smith and Pendry[41] captures the magnetic permeability we introduce, as discussed with regards to Figure 2.2 and Equation 2.1. This scheme has been implemented in the work by Watanabe et al.[53]. Another method can be found in[71] and in references therein. Both of these approaches, however, must be used with caution as they do not explicitly account for spatial dispersion; in contrast, spatial dispersion is taken into account by being considered as a free parameter in Mota et al.[67] and Papadakis et al.[47].

2.7 Conclusions

This chapter has shown that displacement currents in 1D-layered systems can lead to non-unity effective magnetic permeability at optical frequencies. This makes it possible to tailor the magnetic response of planar HMMs, which have been previously explored only for their dielectric permittivity features. It was experimentally demonstrated that planar structures can have negative in-plane magnetic permeability, which can lead to double HMMs. By studying bulk and surface wave propagation, frequency ranges of a relatively polarization-insensitive response have been identified. Through this analysis, TE polarized magnetic surface plasmons, attributed to the negative magnetic permeability, were confirmed to exist. These magnetic plasmons are complementary to typical TM polarized surface plasmonic modes in materials with magnetic media in significantly simplified layered systems.

It is anticipated that this work will enable the generalization of the unique properties of plasmonics and HMMs, previously explored for TM polarizated waves and negative permittivity media, for unpolarized light at optical frequencies.

References

[1] L. Landau, E. Lifshitz, and L. P. Pitaevskii. *Electrodynamics of continuous media*. 2nd ed. Pergamon, 1984.

[2] F. Monticone and A. Alu. "The quest for optical magnetism: from split-ring resonators to plasmonic nanoparticles and nanoclusters". In: *J. Mater. Chem.* (2014), pp. 9059–9072.

[3] V. M. Shalaev. "Optical negative-index metamaterials". In: *Nat. Photonics* (2007), pp. 41–48.

[4] James C. Ginn et al. "Realizing Optical Magnetism from Dielectric Metamaterials". In: *Phys. Rev. Lett.* 108 (9 2012), p. 097402.

[5] U. K. Chettiar et al. "Negative index metamaterial combining magnetic resonators with metal films". In: *Opt. Express* 14 (2006), pp. 7872–7877.

[6] G. Shvets and Y. A. Urzhumov. "Negative index meta-materials based on two-dimensional metallic structures". In: *J. Opt. A: Pure Appl. Opt.* 8 (2006), S122–S130.

[7] J. Zhou et al. "Saturation of the Magnetic Response of Split-Ring Resonators at Optical Frequencies". In: *Phys. Rev. Lett.* 95 (22 2005), p. 223902.

[8] L. Langguth and H. Giessen. "Coupling strength of complex plasmonic structures in the multiple dipole approximation". In: *Opt. Express* 19 (2011), pp. 22156–22166.

[9] R. S. Penciu et al. "Multi-gap individual and coupled split-ring resonator structures". In: *Opt. Express* 16.22 (2008), pp. 18131–18144.

[10] Sergey S. Kruk et al. "Magnetic hyperbolic optical metamaterials". In: *Nat. Commun.* 7.22 (2016), p. 11329.

[11] A. Poddubny et al. "Hyperbolic metamaterials". In: *Nat. Photonics* 7 (2013), pp. 958–967.

[12] V. P. Drachev, V. A. Podolskiy, and A. V. Kildishev. “Hyperbolic metamaterials: new physics behind a classical problem”. In: *Opt. Express* 21 (2013), pp. 15048–15064.

[13] H. N. S Krishnamoorthy et al. “Topological transitions in metamaterials”. In: *Science* 336 (2012), pp. 205–209.

[14] Z. Liu et al. “Far-field optical hyperlens magnifying subdiffraction- limited objects”. In: *Science* 315 (2007), p. 1686.

[15] Alexander A. High et al. “Visible-frequency hyperbolic metasurface”. In: *Nature* 522 (2015), p. 192.

[16] Xiao Lin et al. “All-angle negative refraction of highly squeezed plasmon and phonon polaritons in graphene–boron nitride heterostructures”. In: *Proceedings of the National Academy of Sciences* 114.26 (2017), pp. 6717–6721.

[17] Anthony J. Hoffman et al. “Negative refraction in semiconductor metamaterials”. In: *Nature Materials* 6 (2007), pp. 946–950.

[18] T. Xu et al. “All-angle negative refraction and active flat lensing of ultraviolet light”. In: *Nature* 497 (2013), pp. 470–474.

[19] D. Lu and Z. Liu. “Hyperlenses and metalenses for far-field super-resolution imaging”. In: *Nat. Commun* 3 (2012).

[20] J. Elser and V. A. Podolskiy. “Scattering-free plasmonic optics with anisotropic metamaterials”. In: *Phys. Rev. Lett.* 100 (2008).

[21] E. E. Narimanov. “Photonic hypercrystals”. In: *Phys. Rev. X* 4 (2014), p. 041014.

[22] S. A. Maier and A. H. Atwater. “Plasmonics: localization and guiding of electromagnetic energy in metal/dielectric structures”. In: *J. Appl. Phys.* 98 (2005), p. 011101.

[23] H. J. Lezec, J. A. Dionne, and H. A. Atwater. “Negative refraction at visible frequencies”. In: *Science* 316 (2007), pp. 430–432.

[24] J. A. Dionne et al. “Are negative index materials achievable with surface plasmon waveguides? A case study of three plasmonic geometries”. In: *Opt. Express* 16 (2008), pp. 19001–19017.

[25] Y.-t. Fang et al. “Tamm states of one-dimensional metal-dielectric photonic crystal”. In: *IET Optoelectron.* 7 (2013), pp. 9–13.

[26] Z. Jacob et al. “Engineering photonic density of states using metamaterials”. In: *Applied Physics B* 100 (2010), pp. 215–218.

[27] A. M. Mahmoud and N. Engheta. “Wavematter interactions in epsilon-and-mu-near-zero structures”. In: *Nat. Commun.* 5 (2014), p. 5638.

[28] R. Maas et al. “Experimental realization of an epsilon-near-zero metamaterial at visible wavelengths”. In: *Nat. Photonics* 7 (2013), pp. 907–912.

[29] A. I. Kuznetsov et al. “Magnetic light”. In: *Sci. Rep.* 2 (2012), p. 492.

[30] H. Alaeian and J. A. Dionne. “Plasmon nanoparticle superlattices as optical-frequency magnetic metamaterials”. In: *Opt. Express* 20 (2012), pp. 15781–15796.

[31] Guy Lipworth et al. “Magnetic Metamaterial Superlens for Increased Range Wireless Power Transfer”. In: *Scientific Reports* 4 (2014), p. 3642.

[32] F Capolino. *Theory and Phenomena of Metamaterials*. CRC Press, 2009.

[33] M. S. Mirmoosa, S. Y. Kosulnikov, and C. R. Simovski. “Magnetic hyperbolic metamaterial of high-index nanowires”. In: *Phys. Rev. B* 94 (2016), p. 075138.

[34] S. OBrien and J. B. Pendry. “Magnetic activity at infrared frequencies in structured metallic photonic crystals”. In: *J. Phys. Condens. Matter* 14 (2002), pp. 6383–6394.

[35] N. Engheta, A. Salandrino, and A. Alu. “Circuit elements at optical frequencies: Nanoinductors, nanocapacitors, and nanoresistors”. In: *Phys. Rev. Lett.* 95 (2005), p. 095504.

[36] S. Jahani and Z. Jacob. “All-dielectric metamaterials”. In: *Nat. Nano* 711 (2016), pp. 23–36.

[37] Andrey B. Evlyukhin et al. “Demonstration of Magnetic Dipole Resonances of Dielectric Nanospheres in the Visible Region”. In: *Nano Letters* 12.7 (2012), pp. 3749–3755.

[38] I. Staude and J. Schilling. “Metamaterial-inspired silicon nanophotonics”. In: *Nat. Photonics* 11 (2017), pp. 247–284.

[39] A. Alu and N. Engheta. “Dynamical theory of artificial optical magnetism produced by rings of plasmonic nanoparticles”. In: *Phys. Rev. B* 78 (2008), p. 085112.

[40] V. M. Agranovich et al. “Linear and nonlinear wave propagation in negative refraction metamaterials”. In: *Phys. Rev. B* 69 (2004), p. 165112.

[41] D. R. Smith and J. B. Pendry. “Homogenization of metamaterials by field averaging”. In: *J. Opt. Soc. Am. B.* 23 (2006), pp. 391–403.

[42] R. Merlin. “Metamaterials and the LandauLifshitz permeability argument: Large permittivity begets high-frequency magnetism”. In: *Proc. Natl Acad. Sci. USA.* 106 (2009), pp. 1693–1698.

[43] T. Tumkur et al. “Control of spontaneous emission in a volume of functionalized hyperbolic metamaterial”. In: *Applied Physics Letters* 99.15 (2011), p. 151115.

[44] J. Kim et al. “Improving the radiative decay rate for dye molecules with hyperbolic metamaterials”. In: *Opt. Express* 20.7 (2012), pp. 8100–8116.

[45] X. Ni et al. “Effect of metallic and hyperbolic metamaterial surfaces on electric and magnetic dipole emission transitions”. In: *Appl. Phys. B 103* 103 (2011), pp. 553–558.

[46] V. Agranovich and V. Kravtsov. “Notes on crystal optics of superlattices”. In: *Solid State Commun.* 55 (1985), pp. 553–558.

[47] G. T. Papadakis, P. Yeh, and H. A. Atwater. “Retrieval of material parameters for uniaxial metamaterials”. In: *Phys. Rev. B* 91 (2015), p. 155406.

[48] A. Mazor et al. “Columnar growth in thin films”. In: *Phys. Rev. Lett.* 60 (1988), pp. 424–427.

[49] O. J. Martin, K. Thyagarajan, and C. Santschi. “A New Fabrication Method for Aluminum and Silver Plasmonic Nanostructures”. In: *Workshop on Optical Plasmonic Materials (The Optical Society of America)* (2014).

[50] A. Ishikawa and T. Tanaka. “Negative magnetic permeability of split ring resonators in the visible light region”. In: *Opt. Commun.* 258 (2008), pp. 300–305.

[51] E. N. Economou, T. h. Koschny, and C. M. Soukoulis. “Strong diamagnetic response in split-ring-resonator metamaterials: Numerical study and two-loop model”. In: *Phys. Rev. B* 77 (2008), p. 092401.

[52] T. Driscoll et al. “Dynamic tuning of an infrared hybrid-metamaterial resonance using vanadium dioxide”. In: *Applied Physics Letters* 93.2 (2008), p. 024101.

[53] R. Watanabe, M. Iwanaga, and T. Ishihara. “s-Polarization Brewster’s angle of stratified metaldielectric metamaterial in optical regime”. In: *Phys. Stat. Solid.* 245 (2008), pp. 2696–2701.

[54] Conor T. Riley et al. “Near-perfect broadband absorption from hyperbolic metamaterial nanoparticles”. In: *Proceedings of the National Academy of Sciences* 114.6 (2017), pp. 1264–1268.

[55] E. E. Narimanov et al. “Reduced reflection from roughened hyperbolic metamaterial”. In: *Opt. Express* 21 (2013), pp. 14956–14961.

[56] G. V. Dedkov and A. A. Kyasov. “Equilibrium near and far electromagnetic field structures at a flat boundary of the half-space filled with a homogeneous dielectric (magnetic) medium”. In: *Tech. Phys. Lett.* 32 (2006), pp. 223–225.

[57] P. Yeh. *Optical Waves in Layered Media*. 2nd ed. Wiley-Interscience, 2005.

[58] E. Anemogiannis, E. N. Glytsis, and T. K. Gaylord. “Determination of guided and leaky modes in lossless and lossy planar multilayer optical waveguides: reflection pole method and wavevector density method”. In: *J. Light. Technol.* 17 (1999), pp. 929–941.

[59] E. N. Economou. “Phys. Rev.” In: *Phys. Stat. Solid.* 182 (1969), pp. 539–554.

[60] A. P. Vinogradov et al. “Surface state peculiarities in one-dimensional photonic crystal interfaces”. In: *Phys. Rev. B* 74 (4 2006), p. 045128.

[61] Xingjie Ni et al. “Loss-compensated and active hyperbolic metamaterials”. In: *Optics express* 19.25 (2011), pp. 25242–25254.

[62] David R Smith et al. “Composite medium with simultaneously negative permeability and permittivity”. In: *Physical review letters* 84.18 (2000), p. 4184.

[63] M Kafesaki et al. “Left-handed metamaterials: The fishnet structure and its variations”. In: *Physical Review B* 75.23 (2007), p. 235114.

[64] Gunnar Dolling et al. “Low-loss negative-index metamaterial at telecommunication wavelengths”. In: *Optics letters* 31.12 (2006), pp. 1800–1802.

[65] DR Smith et al. “Electromagnetic parameter retrieval from inhomogeneous metamaterials”. In: *Physical review E* 71.3 (2005), p. 036617.

[66] Xudong Chen et al. “Robust method to retrieve the constitutive effective parameters of metamaterials”. In: *Physical review E* 70.1 (2004), p. 016608.

[67] Achiles F Mota et al. “Constitutive parameter retrieval for uniaxial metamaterials with spatial dispersion”. In: *Physical Review B* 94.11 (2016), p. 115410.

[68] Andrea Alù. “Restoring the physical meaning of metamaterial constitutive parameters”. In: *Physical Review B* 83.8 (2011), p. 081102.

[69] Th Koschny et al. “Resonant and antiresonant frequency dependence of the effective parameters of metamaterials”. In: *Physical Review E* 68.6 (2003), p. 065602.

[70] Vadim A Markel. “Can the imaginary part of permeability be negative?” In: *Physical Review E* 78.2 (2008), p. 026608.

[71] Masanobu Iwanaga. “Effective optical constants in stratified metal-dielectric metameterial”. In: *Optics letters* 32.10 (2007), pp. 1314–1316.

Chapter 3

MULTILAYER SLOT-MODE PLASMONIC FILTERS FOR SPECTRAL FILTERING APPLICATIONS

3.1 Introduction

Today's state-of-the-art mobile electronics are as powerful as larger computers [1], and are equipped with a variety of sensors including accelerometers, gyroscopes, CMOS image sensors, and magnetometers [2]. CMOS image sensors have a particularly broad landscape of potential new functions: optical data on mobile platforms today consists primarily of three-color imaging, but a wide variety of applications could be accessed by the collection of high resolution spectroscopic information. Plasmonic structures have been demonstrated as a color filter platform well-suited for CMOS integration due to the small mode volumes of plasmons and the CMOS compatibility of many of the materials that support them. Plasmonic hole and slit array color filters have been demonstrated as a viable alternative to dye-based filters for RGB and CMYK color-filtering [3–8]. In addition to hole and slit array filters, many other geometries have been explored as potential platforms for commercially viable plasmonic color filters [9–12]. Recently, this spate of development has been translated into industrial CMOS image sensor prototypes and are actively being considered for full commercialization [13].

Previous work has demonstrated plasmonic hole and slit array color filters capable of filtering the visible spectrum into three or four broad spectral bands (>100 nm) [3–8]. By reducing the transmission bandwidth of the filters to less than 30 nm, CMOS image sensors would gain the ability to perform multi- and hyper-spectral imaging without needing to rely on algorithmic post-processing [9, 14]. Multi- and hyper-spectral imaging is utilized in a wide range of terrestrial and space applications, and providing portal devices with this functionality would have implications spanning food quality control to space exploration [15, 16]. Guided mode resonance filters have been shown capable of generating high intensity, narrowband filtering [17]. However, the millimeter-scale of these filters is impractical for CMOS integration [18]. Narrow bandwidth responses have also been reported in thin filmed multilayer plasmonic structures [19]. The peak wavelength of these structures is tuned via

changing the thickness of the intermediate dielectric layer, so the many lithographic steps needed to patterns the tens to hundreds of spectral bands make these structures infeasible for multi- and hyper-spectral filtering. In this work, we have designed and prototyped a micron-scale plasmonic color filter capable of narrow band-pass transmission (<30 nm). The filters span the visible and near infrared spectrum and all utilize the same planar stack of materials where the peak transmission wavelength is determined through a single lithographic step.

Plasmonic color filters utilizing periodic arrays of subwavelength holes or nanoslits in metal films enable efficient conversion of optical energy between incident photons and surface propagating two-dimensional charge density waves, surface plasmon polaritons (SPPs). Due to the permittivity discontinuity at metal-dielectric surfaces, SPPs have an in-plane momentum kSPP greater than that of light in free space ko. Patterned metal surfaces including gratings, or arrays of holes or slits, allow the matching of momentum and thereby enable efficient conversion of light into SPPs via scattering. The strength of interaction between photons and SPPs can be tailored by changing geometric factors such as the shape of the scattering elements, and the symmetry and periodicity of the array as well as by selecting the permittivity of the constituent materials [20].

In particular, periodic arrays of subwavelength apertures passing through a metal film exhibit enhanced transmission exclusively at conditions corresponding to constructive mutual interference between incident light and SPPs traveling along the surface between adjacent slits. In the case that the metallic layer is thick enough to be substantially opaque to incident photons, the SPP mediated process is the dominant mode of transmission and the surface acts as a band-pass color transmission filter. Such aperture arrays have been the topic of substantial scientific interest due to these remarkable optical properties and their utility as a testbed for studying fundamental light-matter interactions in plasmonic systems [7, 21].

The dispersion of plasmonic propagating modes can be further engineered using metal-clad slot waveguides, often realized as multilayer stacks with a metal-insulator-metal (MIM) configuration [8]. Such MIM stacks may support a multitude of polaritonic modes which lie either inside or outside the “light cone,” that is, with in-plane momentum either greater or less than that of a photon with equal energy. This additional degree of freedom enables substantially more complex op-

tical transmission filter spectra enabling narrow bandwidth suitable for multi- and hyperspectral color filtering applications [5].

3.2 Designing Plasmonic Color Filters

Finite difference time domain methods (FDTD) were used to determine the transmission spectra of different filter structures. Fig. 1 illustrates the different types of transmission filters and their spectral behavior. MIM have been used to make RGB color filters [5]. These structures can be optimized to have narrowband transmission, but as the structure is optimized to minimize FWHM of the transmission peak, the intensity of the next highest order mode increases. This trade-off can be lifted by introducing a second MIM mode into the structure that couples with the original MIM mode, leading to the suppression of the spurious transmission. The multilayer slot-mode plasmonic filter (MSPF) investigated demonstrates a narrow transmission bandwidth and spurious peak suppression, as shown in Fig. 1(b), and by changing the periodicity of the slits, this filter can be swept across the entire visible spectrum.

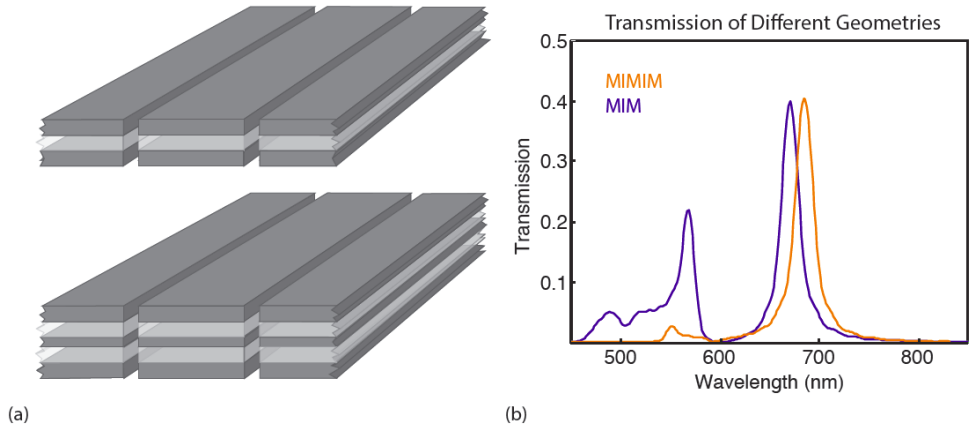

Figure 3.1: (a) Schematics of MIM and MIMIM filter structures. All dark grey metal layers are Ag and 70 nm thick, except for the 50 nm center metal layer of the MIMIM filter. All light grey insulating layers are 70 nm of SiO2 (b) Comparison between MIM and MIMIM transmission behavior shows similar FWHM but enhanced suppression of the secondary peak in the MIMIM case.

The MSPFs were optimized using an incident TM plane wave source. Optimizations were conducted via a series of parameter sweeps that considered both the thicknesses and optical indices of all the insulating and metallic layers, as well as the width and spacing of the milled slits. The initial values for the thicknesses of the metallic layers were determined by considering the skin and penetration depths of various metals. For a successful filter, the top and bottom metallic layers of the structure

must be sufficiently thick to be opaque across the visible and near IR parts of the electromagnetic spectrum. Using data from Rakic et al. for Ag as an example, the 1/e penetration depth (dp) of Ag was calculated to range from 12.9 nm – 16.8 nm across the visible spectrum. To prevent 98% of light from penetrating the structure, the top and bottom layers must be at least 4 times dp. Therefore 68 nm was used as the initial parameter sweep value when optimizing the system that utilized Ag.

Likewise, the starting point for the thickness of the insulating layers was approximated by considering the propagating modes guided laterally within the structure. Numerically determined dispersion curves derived from experimental optical constants of Ag and SiO2 can be used to determine the available modes within an MIM [8]. For SiO2 thicknesses of less than 100 nm, traditional photonic waveguide modes are cut off in an Ag/SiO2/Ag system, so the waveguide only supports high-momentum surface plasmon modes. Therefore, the parameter sweeps used 100 nm as the upper value restriction for the SiO2 thickness of each waveguide.

Iterating over the parameter sweep led to the final device structure, with alternating layers of Ag and SiO2. Both SiO2 layers were optimized to 70 nm, the top and bottom Ag layers are 70 nm and the spacer layer is 50 nm. The width of the slit is 50 nm for all filters and the slit periodicities investigated vary from 250 nm to 550.

The position of the transmission peak varies linearly with the periodicity of the slits and, as shown in Fig. 2(a), peak position can be swept across the visible and near IR spectrum. Therefore, just by varying the inter-slit pitch, a series of MSPFs with the same layer materials and thicknesses can be used as a color filter across a wide range of the spectrum. The FWHM of the transmission spectra are about 20 nm on average with no peak exceeding 28 nm, as shown in Fig. 2(b). Additionally, the overall transmission of the side-lobe peak does not exceed 11% of that of the primary peak in the visible portion of the spectrum, and does not exceed 25% of the primary peak intensity in all filters investigated. While it is possible to design MSPF filters using other materials systems, the Ag/SiO2 system was found to be most optimal. For example, the transmission spectrum of an optimized Al/SiO2 MSPF possesses a FWHM of 34 nm and peak transmission of just over 20%.

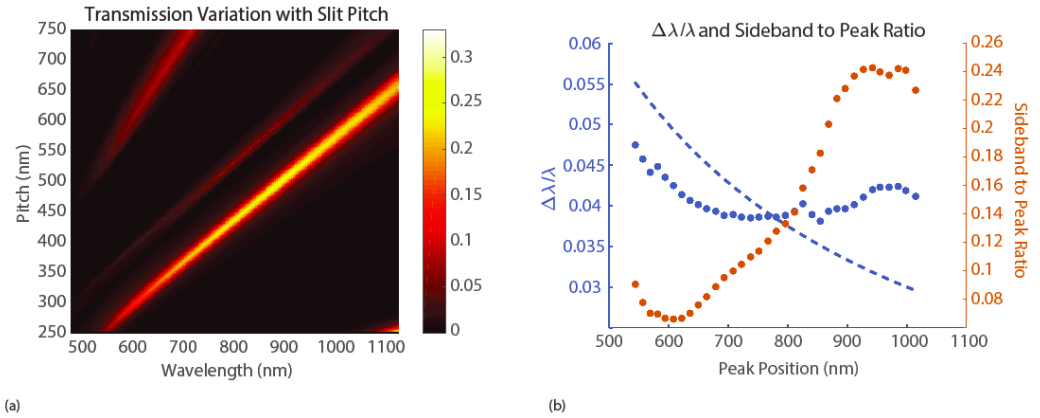

Figure 3.2: (a) Superposition of the transmission behavior of filters with varying slit pitches. As slit pitch increases the narrowband transmission peak is controllably shifted to longer wavelengths. (b) The relationship between FWHM, peak position, and sideband to peak ratio. The blue axis illustrates the ratio of FHWM to the peak position. The dashed line sets the threshold of a 30nm FWHM, and the dotted line illustrates the ratio of the transmission peak's FWHM to the peak position. The dotted line is beneath the dashed line for the entire visible spectrum, indicating that all filters fulfill the criteria for hyperspectral imaging. The orange dotted line illustrates the ratio between the sideband and main intensity peaks, showing the best filters are also in the visible part of the spectrum.

3.3 Experimental Verification

MSPFs were fabricated by depositing alternating layers of Ag and SiO2 in an electron beam evaporator onto a solvent cleaned fused silica slide and then subsequently milled using a focused ion beam (FIB). The 50 nm slit milled into a 330 nm structure is a prohibitively demanding aspect ratio for a FIB trench mill. For a set of proof-of-concept filters, these demanding design conditions can be relaxed by considering filters only towards the lower energy portion of the visible spectrum. For a slit width of 120 nm, the suppression of the spurious transmission peak is retained and the FWHM of the primary transmission peak only takes a 25 nm hit.

When Ag is deposited on SiO2 in an electron beam evaporator, the Ag films grow with a columnar growth mechanism [22]. These films are rough, which increases plasmonic loss, thereby reducing overall transmission intensity of the filter [23]. The roughness of Ag deposited on SiO2 is even more problematic in a multilayer structure like the MSPF because the roughness of each Ag layer compounds. A rough substrate increases the roughness of the film deposited on it due to differences in atomic flux received by areas of the film with positive and negative curvatures that

are larger than can be compensated for by surface diffusion [22]. Because the SiO2 conformally deposits on the underlying Ag layer, each Ag layer sees a progressively rougher substrate, leading to a very rough top surface of the MSPF.

By utilizing a seed layer of AgO deposited onto each SiO2 surface, a much smoother Ag film can be deposited [24]. The AgO is deposited by slowly electron beam evaporating Ag at a rate of 0.1 A/s in a chamber with an O2 pressure of 9.5x10-5 torr. Once 2 nm of AgO are on the surface of the SiO2, the deposition is paused and the AgO is held under vacuum for 10 minutes. Because AgO is not vacuum stable, the oxygen is pumped out of the film, leaving a thin Ag layer on the surface of the SiO2 [24]. The deposition is then resumed and the rest of the Ag layer is deposited at in a chamber with pressure 2.3x10-6 torr and no oxygen flow. The roughness of Ag films deposited with this method was measured to have an RMS of 2.56 nm and the top Ag surface of a multilayer deposited with the AgO growth method has an RMS of 2.92 nm. Each Ag layer was deposited using this method.

To further protect the integrity of the filter, a sacrificial layer was put on the top Ag surface. First a 90 nm layer of 950 A2 PMMA was then spun onto the top surface of the MSPF and then another 70 nm layer of Ag was deposited on top of the PMMA. The sacrificial layer protects the top Ag film of the MSPF by confining the worst of the ion beam damage to the surface of the sacrificial layer, rather than the surface of the MSPF. To utilize the best possible resolution of the ion beam, the 130 nm wide slits are milled in FEI Versa FIB, at 30 kV and 1.5 pA [25]. The high accelerating voltage and low beam current help compensate for the high aspect ratio of the filter structure. Multi-pass milling is used to reduce the taper of the slits—first a rectangle is milled, followed by a frame around the perimeter to better define the edges and clean off reposition within the slit. The sacrificial layer is then removed using a heated solvent bath.

The fabricated filters are then measured using a supercontinuum laser with monocrometer set-up that allows for the sample to be illuminated with a narrow bandwidth of incident radiation. A 5X objective takes the collimated light and focuses it down to a 10 um spot size with a 5.7deg angular spread from the incident normal. The incident beam is shined on the 30 μm x 30 μm MSPFs. Squares equal in size to the filters were milled 100 μm away from each filter and are used to determine the intensity of the laser. All transmitted power was collected by a Si photodiode that was

affixed behind the substrate in which the filters and normalization squares have been milled. The experimental response of each filter was determined by normalizing the light transmitted through the filter by that transmitted through its corresponding normalization square.

Fig. 3(a) shows the experimental transmission response of a prototype filter that has an inter-slit pitch of 475 nm. A cross section of the prototype filter was milled using the FIB. The micrograph of the filter's cross-section, shown in Fig. 3(c) reveals that there is a slight taper to the filter structure. Using FDTD simulations, we can compute the transmission behavior of filters with a progressively increasing sidewall taper. The results of these simulations, shown in Fig. 3(b) illustrate the importance of the slit sidewalls on the overall behavior of the structure. Using the information gathered from the FDTD simulations, it was determined that to maintain filtering behavior with side lobe suppression, the sidewalls of the slit could not possess greater than a 5deg taper. The side lobe in the experimental transmission is due in part to the 13.7deg taper in the fabricated filter. In future work, this taper can be eliminated by utilizing nanoimprint lithography couple with advanced thin film deposition techniques to produce MSPF filters with less taper. Additionally, diffractively coupled resonances are angle sensitive, so the angular spread of the incident beam also led to slight broadening and side lobe enhancement.

The polarization response was also experimentally confirmed to match the simulated predications, as shown in Figs. 4(a) and (b). While the fabricated filters were polarization sensitive, Figs. 4(c) and 4(d) illustrate that the polarization dependence of MSPFs can be eliminated entirely by introducing a second array of slits perpendicular to the original slit array, allowing any incident k-vector to effectively couple into the plasmon modes of the filter.

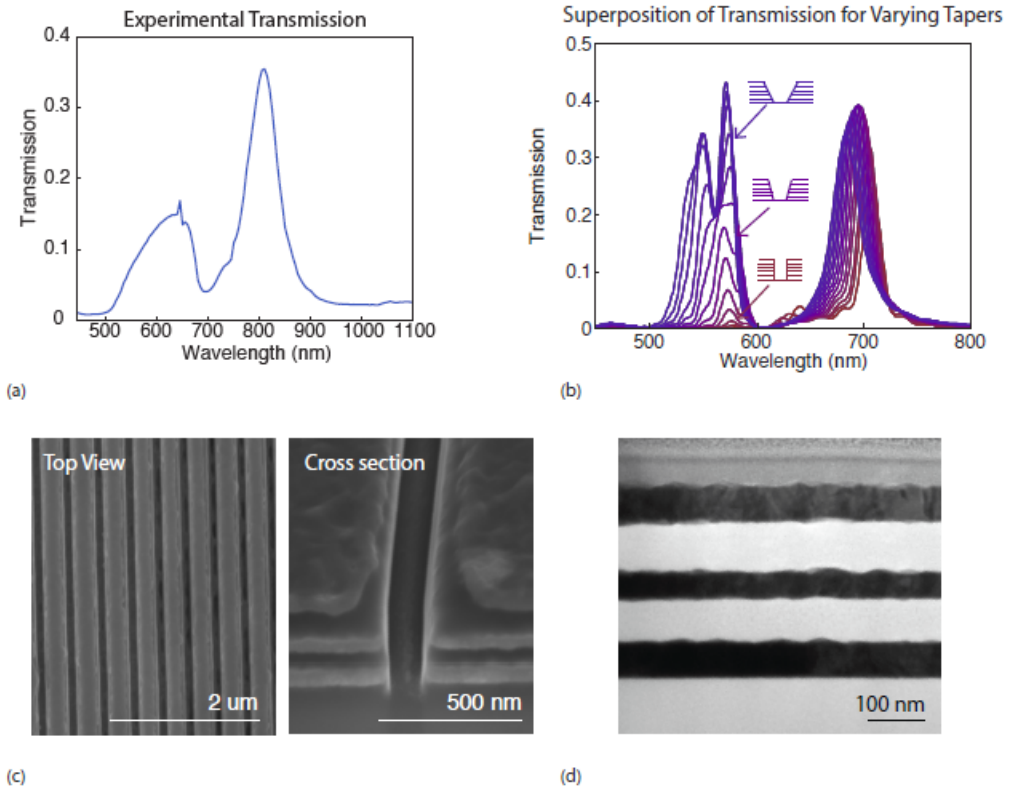

Figure 3.3: (a) Experimentally determined transmission of a single MIMIM filter. (b) Simulated dependence of transmission on taper of slits. (c) Top down and cross-sectional SEMs of the MSPF filter. (d) TEM micrograph showing the layer thicknesses and roughness of the five layers of the filter.

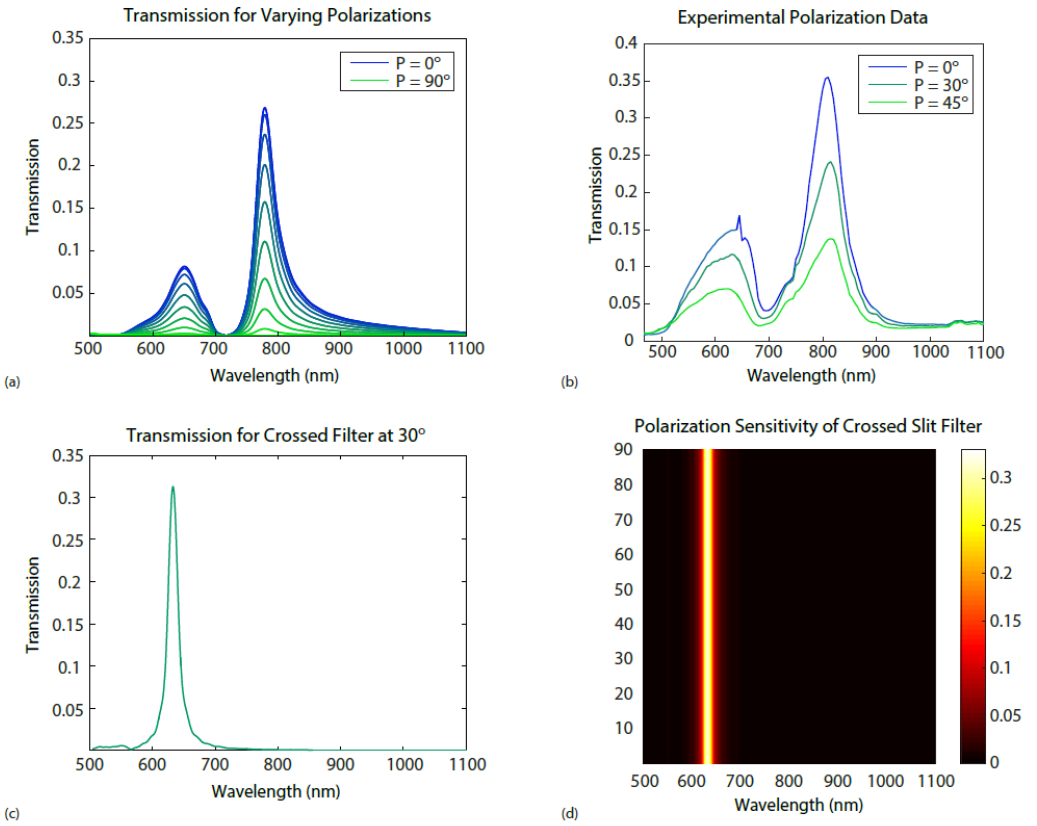

Figure 3.4: (a) Simulated polarization response varying from 0° (blue) to 90° (green). (b) The simulated polarization response was confirmed experimentally, with a 0° measurement (blue), a 30° measurement (teal), and a 45° measurement (green). (c) A transmission spectrum for a crossed MSPF structure with incident polarization oriented at 30° from the original grating normal. (d) Superposition of transmission curves spanning 0° to 90° for a crossed MSPF structure showing complete polarization insensitivity.

3.4 Analytical Analysis

A series of FDTD simulations was performed in order to study the electromagnetic modes that propagate in the MIMIM device stack. To study fundamental properties of these guided mods, light is coupled into the stack using plane wave illumination of a single slit, as opposed to the periodic array of slits that comprise the MSPF structures. A series of 211 single frequency TM plane wave excitations were used to sweep over the entire visible spectrum. Complex vector field data was collected by finely meshed monitors capturing the EM time evolution of each of the FDTD simulations. This dataset can be compressed by taking a discrete-time Fourier transform at runtime which transforms the time-harmonic field data in the frequency domain.

In Fig. 5(a), a single electric field component is plotted from the compressed data set of a sample simulation conducted at an excitation energy of 1.88 eV. The spatial mapping of the electric field depicts light scattered by a slit at z = 0 into multiple modes propagating in the z-direction. These modes have high field intensity within both SiO2 layers as well as the top and bottom Ag surfaces. The spatial mapping of the electric field indicates that slit preferentially couples energy into the topmost SiO2 layer. Coupling between the two dielectric layers is also apparent, as a characteristic beating pattern is observed indicating that power is oscillating between the two MIMs. This result was expected physically—the spacer layer between the two insulating layers is thinner than the skin depth of Ag at this photon energy. To better determine the natures of the various modes within the MSPF, a second Fourier Transform was performed. Using Equation 3.1, an FFT was taken over the propagation direction of the modes (z), thereby moving the phasor direct space dataset into momentum space (i.e., “k-space”).

$$f(k) = \int F(z)e^{ikz}dz \tag{3.1}$$

The results of this FFT can be plotted, as shown in Fig. 5(b), to illustrate the various modes excited by the single frequency source. The vertical streaks in the spectral power map indicate there are modes at multiple propagation wavevectors (kz) at this excitation frequency. Vertical cross-sections through this dataset describe the spatial field profile along the x-axis transverse to the propagation direction, and can provide insight into the nature of particular modes. For example, the dark red streak at kz = 2.7 μm^{-1} is localized on the metallic surface of the MSPF filter, and therefore this feature can be identified as an SPP. Indeed, this corresponds to the expected

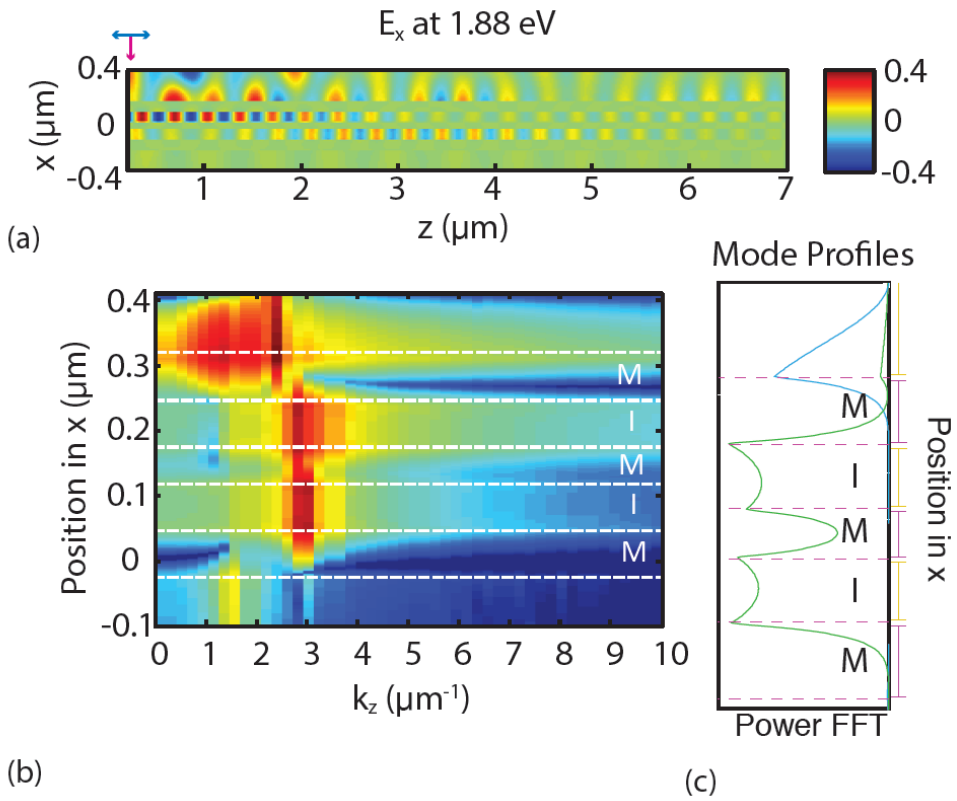

Figure 3.5: (a) Fields resulting after a TM plane wave, incident in the negative x direction, scatters at a single slit and couples into MIM modes propagating in the z direction. (b) An FFT of the fields at a single excitation frequency shows multiple modes resolved by wavenumber. (c) Cross section through the FFT data at a select wavenumber reveals the spatial mode profile.

wavenumber for an SPP on the surface of an Ag film at this excitation frequency.

Close inspection of the intensity patterns of the hot spots in Fig. 5(b) reveals that the region of high spectral power on the surface of the filter at wavenumbers less than 2.7 μm^{-1} corresponds to unbound modes that do not contribute to filter behavior. After discarding the evanescently reflecting quasi-modes, the nature of the remaining modes can be determined by plotting the linear intensity variations at each wavenumber that possesses a streak of high spectral power, superimposing these linear intensity variations on the same axis yields the plot shown in Fig. 5(c). This plot depicts the two strongest plasmon modes in the structure: the mode on the top surface of the filter and the mode spanning the insulating layers contained within the filter. The predominant surface mode, shown in blue in Fig. 5(c), corresponds to SPPs excited at the top Ag surface of the filter. The other excitation is a super-mode

corresponding to a coupling of the two MIM modes generated within each of the two insulating layers in the structure. This is the mode that was implied in the spatial field map in Fig. 5(a) is now clearly depicted in Fig. 5(c), which reveals that the two MIM modes within the super-mode are coupled because of strong field overlap within the 50 nm Ag spacer.

The behavior of the energy propagating through the filter can be determined by the FFT analysis, but it does not indicate how these modes contribute to the overall behavior of the filter. The contribution of each mode to the unsuppressed transmission peak can be determined by normalizing the transmission curves of the periodic grating MSPF structures over the dispersion curve of each mode and the pitches of the filter gratings.

The dispersion curve of each plasmon mode can be determined by constructing a dispersion curve for the MSPF. The dispersion curve shown in Fig. 6(a) was constructed by using the Fourier Transformed k-space data sets and plotting the power of the modes at each spectral frequency as a function of energy. The two branches on curve correspond to the bottom side SPP and the metal-insulator-metal-insulator-metal (MIMIM) super-mode, and can be mapped to the frequency values that correspond to these modes in Fig. 5(c). The lower intensity signal plotted to the left of the branches corresponds to the unbound quasi-modes bouncing off the surface of the filter. From the data contained within this plot, the dispersion curve for each of the two modes can be analytically determined.

The transmission behavior was first normalized over the pitch of the filter grating to lift the dependence of the transmission curves on that characteristic of the filters [21]. Fig. 6(b) shows the transmission curves normalized by the SPP dispersion curve, leading to curves aligned between 0.5 and 1, with the transmission minima collapsing at 1 on the normalized axis [21]. This behavior illustrates that the SPP mode satisfies the momentum matching condition required for it to contribute to the transmission behavior of the filter, with the MIMIM super-mode acting as a supplementary suppression to remove the second highest order peak. This analysis confirms the origin of the spurious peak in the experimental results. As the slits are tapered, the difference between the lengths of the two channels increases, which affects the interference between the two modes. The change in interference behavior reduces the filtering efficiency of this mode and allows multiple orders of modes to

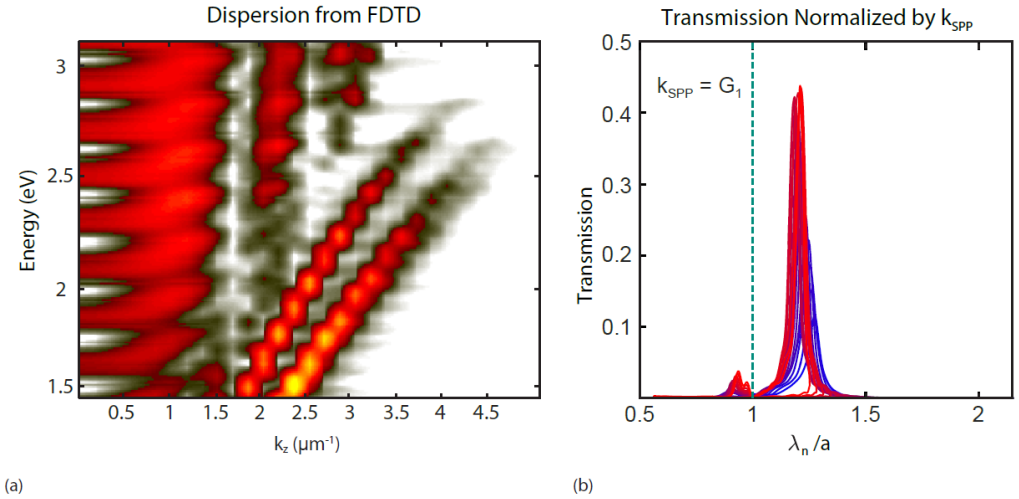

Figure 3.6: (a) By taking FFTs of a sweep of single frequency excitations, a dispersion curve can be constructed that illustrates the behavior of both active modes. (b) Universal curve analysis confirms that the SPP mode on the top surface of the MSPF filter is predominantly responsible for the filters transmission behavior. The various colors of the transmission curves correspond to different peak intensity positions that have all been normalized by the SPP dispersion curve. G1 is the lowest order reciprocal lattice vector and 'a' corresponds to the pitch of the slits.

propagate through the structure, leading to a reduced suppression of the spurious peak.

3.5 Future Work and Conclusions

A plasmonic color filter with a single narrowband transmission response was designed using FDTD and fabricated to confirm the simulated response. However, the fabricated filters were designed to match the infinite periodic array of slits that was simulated in the FDTD simulations. To determine how well these filters could be integrated into devices, a series of calculations were performed to determine how many slits are required for a MSPF filter to achieve the long-range order condition. The superposition of transmission curves shown in Figure 3.7 begin with an MSPF filter with one slit (blue) and step one slit at a time to 64 slits (green). The black curve shows the infinite slit case. These filters rely on long-range order far more than a slit array in a single metal film due to the complex interactions of the SPP modes with the waveguide supermode, so while they could be useful in larger format devices, they are not suitable for small-footprint applications.

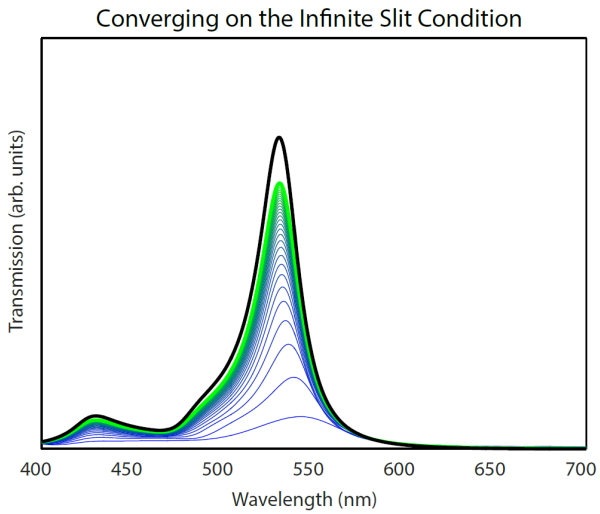

Figure 3.7: Superposition of FDTD calculated transmission responses demonstrating the long-range order dependence of the MSPF filter. The transmission response approaches the infinite case (black curve) as the number of slits increases from one (bluest curve) to 64 (greenest curve).

While the long range order dependence of the grating limits how small this filter can be sized, the grating does preserve behavior across a wide sweep of angles. The angle sensitivity, shown in Figure 3.8, indicates that while the overall coupling efficiency reduces as the angle changes from normal-incidence, the peak position does not shift.

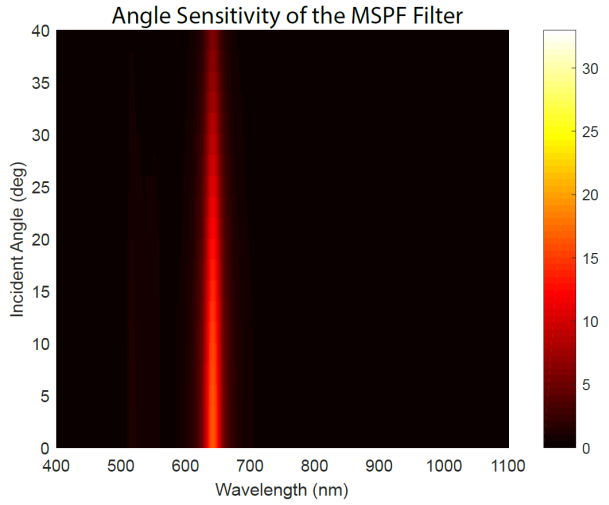

Figure 3.8: Heatmap of FDTD calculated transmission responses of MSPF filters under different angles of incidence. While coupling efficiency decreases with increased angle, the transmission peak remains fixed.

The behavior of this filter was analytically determined to arise from a combination of

SPP excitations– the surface SPP mode leads to the enhanced transmission behavior associated with subwavelength plasmonic filters, while the slightly asymmetric MIM super-mode leads to the suppression of the spurious transmission peak that arises in other narrowband plasmonic filter geometries. The MSPF is inherently gated, and this feature will be capitalized on in future work by incorporating transparent conducting oxides into this geometry to create tunable narrowband color filters spanning both the visible and near infrared parts of the spectrum. Future work, discussed in Chapter 4, utilizes the basic concepts of sub-wavelength slits and plasmon coupling to produce narrow bandwidth transmission that can be confined to ultracompact footprints.

References

[1] M. Khoso and K. Kamra. "Smartphones: A Supercomputer in Your Pocket". In: *http://www.northeastern.edu/levelblog/2016/04/21/smartphones-supercomputer-in-your-pocket/* (2016).

[2] Android. "Sensors Overview". In: *https://developer.android.com/guide/topics/sensors/sensors_overview.html* (2017).

[3] S. Yokogawa, S. P. Burgos, and H. A. Atwater. "Plasmonic color filters for CMOS image sensor applications". In: *Nano Letters* 12 (2012), pp. 4349–4354.

[4] S. P. Burgos, S. Yokogawa, and H. A. Atwater. "Color imaging via nearest neighbor hole coupling in plasmonic color filters integrated onto a complementary metal-oxide semiconductor image sensor". In: *ACS Nano* 7 (2013), pp. 10038–10047.

[5] T. Xu et al. "Plasmonic nanoresonators for high-resolution colour filtering and spectral imaging". In: *Nature Communications* 1.59 (2010).

[6] B. Y. Zheng et al. "Color-selective and CMOS-compatible photodetection based on aluminum plasmonics". In: *Advanced Materials* (2014), pp. 6318–6323.

[7] T. W. Ebbesen et al. "Extraordinary optical transmission through sub-wavelength hole arrays". In: *Nature* 86 (1998), pp. 1114–7.

[8] J. A. Dionne andL. A. Sweatlock, H. A. Atwater, and A. Polman. “Plasmon slot waveguides: Towards chip-scale propagation with subwavelength-scale localization”. In: *Phys. Rev. B - Condens. Matter Mater. Phys.* 73 (2006).

[9] Q. Chen et al. “Nanophotonic Image Sensors”. In: *Small* 12 (2016), pp. 4922–4935.

[10] H. Wang et al. “Full Color Generation Using Silver Tandem Nanodisks”. In: *ACS Nano* 11 (2017), pp. 4419–4427.

[11] A. Kristensen et al. “Plasmonic colour generation”. In: *Nat. Rev. Mater. 2* 16088 (2016).

[12] L. Frey et al. “Color filters including infrared cut-off integrated on CMOS image sensor”. In: *Opt. Express* 19 (2011), p. 13073.

[13] T. Hirayama. “CMOS Image Sensor Evolution: Past, Present, and Future”. In: *SEMICON Europa* (2016).

[14] W.-Y. Jang et al. “Experimental Demonstration of Adaptive Infrared Multispectral Imaging using Plasmonic Filter Array”. In: *Scientific Reports* 6 (2016), p. 34876.

[15] A. A. Gowen et al. “Hyperspectral imaging – an emerging process analytical tool for food quality and safety control”. In: *Trends Food Sci. Technol.* 18 (2007), pp. 590–598.

[16] E. K. Hege et al. “Hyperspectral imaging for astronomy and space surveillance”. In: *Opt. Sci. Technol. SPIE’s 48th Annu. Meet.* 5159 (2004), pp. 380–391.

[17] S. S. Wang and R. Magnusson. “Theory and applications of guided-mode resonance filters”. In: *Appl. Opt.* 32 (1993), pp. 2606–2613.

[18] D. B. Mazulquim et al. “Efficient band-pass color filters enabled by resonant modes and plasmons near the Rayleigh anomaly”. In: *Opt. Express* 22 (2014), pp. 30843–30851.

[19] Z. Li, S. Butun, and K. Aydin. “Large-area, Lithography-free super absorbers and color filters at visible frequencies using ultrathin metallic films”. In: *ACS Photonics* 2 (2015), pp. 183–188.

[20] H. Gao, W. Zhou, and T. W. Odom. “Plasmonic crystals: A platform to catalog resonances from ultraviolet to near-infrared wavelengths in a plasmonic library”. In: *ACS Photonics* 2 (2010), pp. 183–188.

[21] D. Pacifici et al. “Universal optical transmission features in periodic and quasiperiodic hole arrays”. In: *Opt. Express* 16 (2008), pp. 9222–9238.

[22] A. Mazor et al. “Columnar growth in thin films”. In: *Phys. Rev. Lett.* 60 (1988), pp. 424–427.

[23] A. A. Maradudin and D. L. Mills. “Scattering and absorption of electromagnetic radiation by a semi-infinite medium in the presence of surface roughness”. In: *Phys. Rev. B* 11 (1975), pp. 1392–1415.

[24] O. J. Martin, K. Thyagarajan, and C. Santschi. “A New Fabrication Method for Aluminum and Silver Plasmonic Nanostructures”. In: *Workshop on Optical Plasmonic Materials (The Optical Society of America)* (2014).

[25] A. Joshi-Imre and S. Bauerdick. “Direct-Write ion beam lithography”. In: *Nanotechnol.* (2014).

Chapter 4

ULTRACOMPACT AND HIGH RESOLUTION PLASMONIC COLOR FILTERS

4.1 Introduction

The concept of dimensional scaling has been a cornerstone of solid-state integrated device technology over the past 50 years, fueling 'Moore's law' performance advances in silicon integrated circuits[1], magnetic memories[2], optical fiber data transmission[3], among others. Dimensional scaling of pixel size from over 10 μm to as small as 1.1 μm in CMOS digital image sensor arrays over the last decade has led to greatly increased electronic image resolution, accomplished by coupling an objective lens to a focal plane area populated by an ever-increasing number of pixels at constant array size[4]. These image sensors utilize filters composed of dye-doped polymers that allow them to transmit incident light over red, green, and blue ranges of the visible spectrum to form a color image. Such dye-based color filters typically do not allow for high spectral resolution but are adequate for 3-color imaging. Many alternative color filter concepts based on resonances in nanophotonic structures have been explored in attempt to improve upon the transmission efficiency, spectral resolution and spatial resolution of dye based color filters, which suffer from issues with optical cross-talk at small length scales and degradation under UV radiation[4]. Successful demonstrations of hole and slit array filters have relied on short range order, achieving footprints as small as 1 μm[4, 5].

However, these small footprint filters possess relatively large transmission bandwidths, on the order of 100-150 nm, sufficient for 3-color imaging but not for multispectral or hyperspectral imaging. If filters could be realized that feature transmission bandwidths less than 30 nm, rather than filtering just three colors, imaging systems could be designed to spectrally separate the visible and near-infrared spectrum into 20 colors or more, enabling acquisition and construction of an optical spectrum at every pixel in an image[6, 7]. This type of data collection, termed hyperspectral imaging, provides image sensors with the ability to perform spectroscopy at every pixel in an image. The ability to perform multispectral and hyperspectral imaging functions using a compact CMOS image sensor without any moving parts

would have far-reaching impacts in fields as disparate as healthcare, food quality control, and space exploration[8–10].

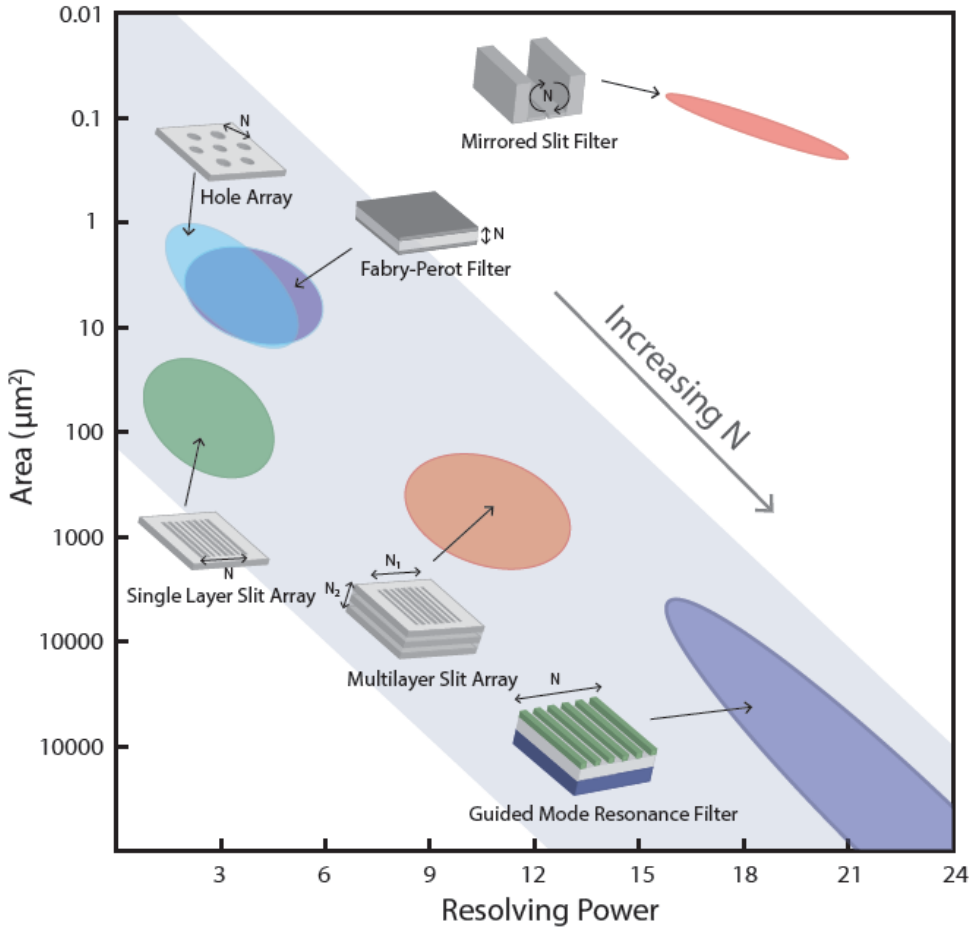

Figure 4.1: The relationship between the volume of a filter and its resolving power ($\lambda/\Delta\lambda$) for transmission color filters in the visible part of the spectrum. The general trend is shown in the grey region, where smaller footprint filters possess large spectral features and larger footprint filters possess smaller spectral features. This relationship is dictated by N, the number of periods contained within the filter. This relationship is broken by the mirrored slit filter (red oval), because the mirrors create an effectively large number of periods within a very confined space.

While there have been demonstrations of nanophotonic color filter architectures capable of producing narrow transmission bandwidths, these filters are large, because they rely on medium-to-long range periodic effects to produce their narrow spectral features[11–14]. Guided-mode resonance filters (GMRs) utilize a transmissive waveguide grating to produce a resonant response[12]. The resolving power ($\lambda/\Delta\lambda$) of the transmission band is directly related to the number of periods[15]. To achieve

a narrow spectral resonance, GMR filters require approximately 50 lattice periods, which gives them a spatial footprint on the 10s of microns at optical wavelengths, making them far too large to serve as color filters in CMOS image sensors[15].

This relationship between quality factor and lattice periodicity is not particular to GMR filters but is related to the spatial-spectral transform relations of periodically-structured media. In general, as the number of periods (N) in a filter increases, so does the spectral resolving power. As shown in Figure 4.1 for experimental results, hole array filters, single film slit array filters, and single film Fabry-Perot resonant filters can all exhibit relatively small footprints, but their experimental spectral transmittances are broad, and color separation is limited to 3 or 4 spectral bands[4, 5, 16, 17]. Multilayer slot mode plasmonic color filters introduce an additional dimension of periodicity, which allows for a narrower response, but the footprint of these filters, while smaller than GMR filters, is still too large for the smallest pixel image sensor applications[11].

Reflective boundaries at the edges of a smaller footprint all-dielectric microwave GMR filters have been used to create a synthetic long range order in smaller footprint structures[18]. In this paper, we use highly reflective metal boundaries on a single plasmonic slit to break the relationship illustrated in Figure 4.1 between footprint and periodicity. The metal mirrors in the mirrored filter impose effective periodic boundary conditions on the transmission slit, that in the lossless limit would introduce infinite periodicity into a small footprint structure. These filters are simultaneously smaller than any color filter described in the literature and possess a resolving power on par with the highest performing nanophotonic visible light color filters that benefit from long range order effects.

4.2 Mirrored Filters

The mirrored filters possess many highly coupled parameters that can be used to control the filters performance. The schematic shown in Figure 4.2 shows the main parameters considered during the optimization of these filters: mirror height, mirror spacing, slit width, film thickness, and oxide thickness.

The general design of the mirrored color filter takes advantage of multiple resonances within the structure. These resonances can be studied and visualized using Lumerical MODE solutions, an eigenmode solver. This method revealed many different

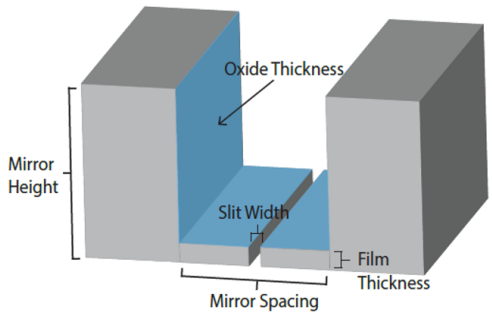

Figure 4.2: Schematic of the narrowband transmission filter showing the main structure parameters: film thickness, mirror height, mirror spacing, slit width, and oxide thickness (shown in blue).

modes supported by the mirrored filter structure at its transmission peak. A few of the dominant modes are shown in Figure 4.3. A gap mode, shown in Figure 4.3(a), is supported in the deeply subwavelength slit that penetrates the thin film. Figure 4.3(b) shows a cavity mode supported by two vertical mirrors, where the available cavity modes are dictated by the mirror spacing, mirror height, and oxide thickness. These modes can be used to produce narrowband spectral responses in Fabry-Perot filters[14]. The thin film also supports surface plasmon polariton modes (SPPs) on its top and bottom surfaces. A top surface SPP mode is shown in Figure 4.3(c). SPP modes have been used to produce transmission color filtering when incorporated into a grating structure. In addition to these three types of modes, there are numerous other modes supported by this structure. However, the transmission filters that exhibit high spectral resolution are characterized by coupling of these three modal types to achieve narrowband filter performance. By optimizing a structure to be resonant at specific wavelengths, it is possible to produce narrow-bandwidth transmission color filtering.

To determine the exact source of the narrowband transmission behavior, mirrored filters with different physical parameters were studied, which are all listed in Table 4.1. Figure 4.4 shows the transmission behavior of four different mirrored filters. The blue transmission curves are from a champion filter identified by a numerical optimization method. The red, green, and violet curves are all deviations from the ideal geometry that illuminate the connection between the physical parameters and the optical response. The suppressed transmission in the red curve in Supplemental Figure 4.4(a) is due to weak gap mode that prevents the modes supported by this

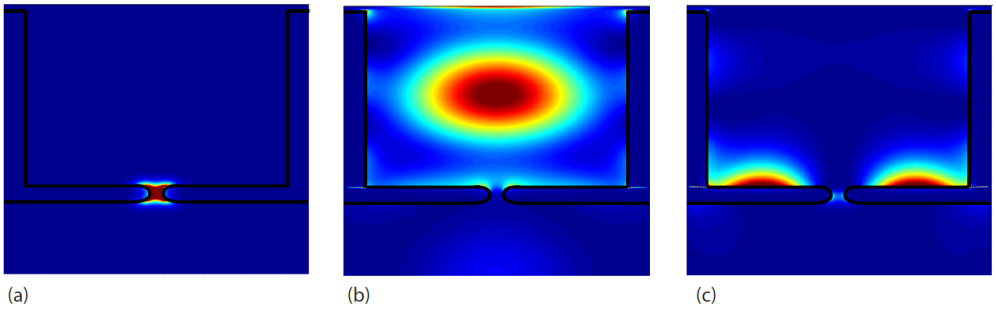

Figure 4.3: Electric field intensity profiles for sample eigenmode solutions for a mirrored slit filter. (a) Gap mode within the slit in the thin film with behavior controlled by the slit width and film thickness. (b) Cavity mode contained between the two mirrors with behavior controlled by the mirror height, mirror spacing, and oxide thickness. (c) Surface plasmon polariton mode supported on the surface of the thin film with behavior controlled by the film thickness, oxide thickness, mirror spacing, and slit width

Curve	**Blue**	**Red**	**Magenta**	**Green**
Mirror Spacing	620	180	800	620
Mirror Height	598	598	598	598
Film Thickness	48	84	48	96
Gap Width	31	44	44	31
Oxide Thickness	1	12	12	1

Table 4.1: Physical parameters for the filters with responses plotted in Figures 4.4 and 4.5. All dimensions are in nm.

filter from out-coupling into the far-field (a representative mode supported by this structure is shown in Figure 4.5(b)). This gap mode, shown in Figure 4.5(a) has a weaker electric field intensity than those of the two filters with higher transmission efficiency shown in Figures 4.5 (c) and (g) (the green and violet curves in Figure 4.4(b) and (c)).

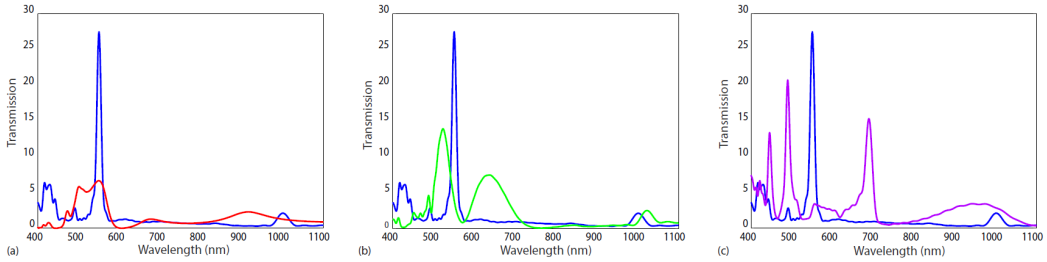

Figure 4.4: (a) comparison between a champion filter (blue) and a filter with reduced transmission (red). The red curve filter possesses a much smaller mirror spacing than the champion filter and a thicker film, which prevent efficient out-coupling of the supported modes. (b) comparison between a champion filter (blue) and a filter (green) with the same physical parameters except for a thicker film, indicating that the thickness of the film between the mirrors plays a very large role in the narrow transmission bandwidth. (c) comparison between a chamption filter (blue) and a filter (violet) with multiple resonances that produce narrow transmission features. The physical parameters of all filters shown are listed in Table 4.1. Representative mode profiles for each of these filters are shown in Figure 4.5

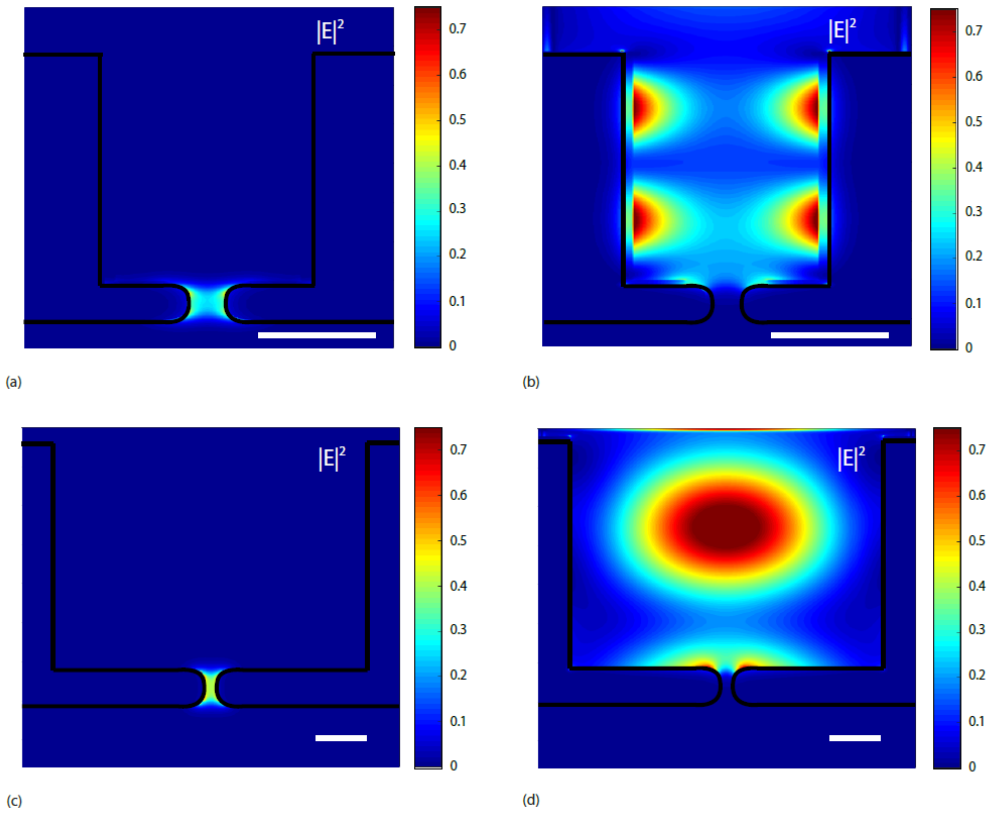

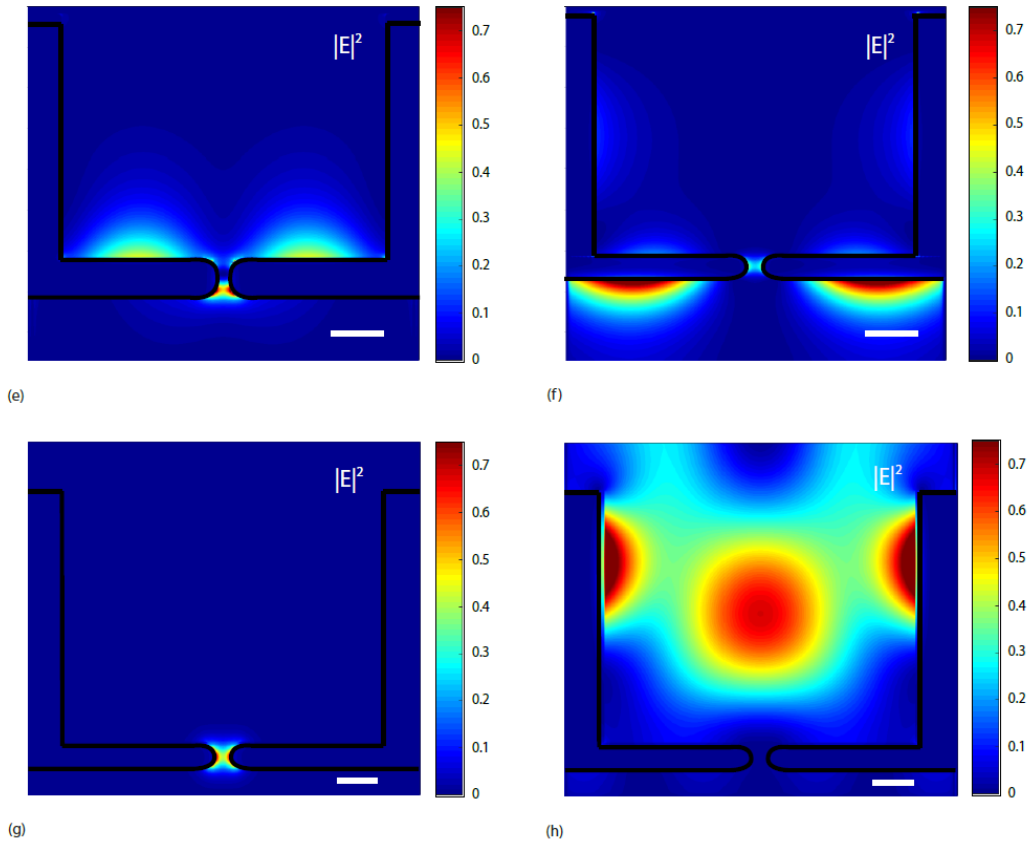

Figure 4.5: (a) and (b) are electric field intensity mode profiles for Figure 4.4(a) red curve filter calculated at 547 nm. The relatively weak gap mode in (a) prevents efficient outcoupling of the mode shown in (b), which leads to this filter's low transmission intensity. (c)-(e) are mode profiles for the green curve filter shown in Figure 4.4(b) calculated at 614 nm. The more efficient gap mode allows for a higher out-coupling of the cavity mode shown in (d) and the SPP shown in (e), which is reflected in the transmission curve shown in Supplemental Figure 1(b). The transmission features are still relatively broad, but by reducing the thickness of the metal film, while holding the rest of the physical parameters of this fixed, the transmission peak can be narrowed. A mode profile calculated at the filter transmission peak at 554 nm is shown in (f) where it is possible to see electric field intensity spanning the thin film, indicating that the top and bottom surface SPPs are coupled and interacting, leading to a much reduced bandpass for this filter relative to the thick film case. (g) and (h) are the mode profiles calculated for the violet curve shown in Figure 4.4(c) at 688 nm, which posseses multiple narrow transmission features. (g) indicates, as expected, that the gap mode is efficient enough to allow for modes to couple out of the filter. The profile shown in (h) indicates that the interacting cavity and SPP modes also couple to the SPPs on the far side of the thin film, which lead to the sharp transmission features present in this filters spectral response.

The primary source of the narrowband transmission is the thickness of the metal film spanning the region between the two mirrors. In Figure 4.4(b), the physical parameters of the green curve filter are identical to those of the blue filter except that the green filter's film is twice the thickness of the blue filter. Increasing the thickness of the film pushes it outside the range of the skin depth of visible light, thereby preventing SPP modes from coupling across the surface of the film. The mode profiles verify that the supported modes only couple across the film in the thin film case. There is no evidence of cross-film coupling in the supported modes of the green curve filter (shown in Figure 4.5(d) and (e)), but the thin film case clearly possesses cross-film coupling, as shown in Figure 4.5(f).

By combining these conditions, a supported gap mode and cross-film coupling, it is possible to produce narrowband transmission features. The filter shown in the violet curve in Figure 4.4(c) possesses a thin film and multiple narrow transmission features. Each of these features correspond to different supported modes in the structure. An example of a supported mode was determined for the peak at 688 nm and is shown in Figure 4.5(h) which illustrates a cavity mode coupled to SPPs on the surfaces of the mirrors. This mode penetrates the thin film, as shown by both the non-zero field in the film and the weak SPPs supported on the film outside the cavity. The efficient gap mode shown in Figure 4.5(g) allows for this mode to out-couple for a transmission response. The dimensions for all filters described in Figures 4.4 and 4.5 are listed in Table 4.1.

While the presence of a gap mode and the thinness of the metal film play a large role in the transmission response, changes to any of the filter dimensions were found to affect the coupling of the excited modes and the resulting transmission of the filters. The height and spacing of the mirrors, the thickness of the thin film, the slit width, the high index oxide coating thickness, and the materials chosen as the metal and dielectric components all affect the filter transmission efficiency and linewidth.

4.3 Inverse Design

Even for a fixed set of chosen dielectric and metallic materials, the number of parameters is too high and their relationships too complex to effectively optimize filter transmission efficiency and linewidth by heuristic analysis and inductive physical reasoning alone. To ensure a strong candidate filter was identified, a numerical optimization method was used to design the champion filter fabricated in this study.

There are many numerical optimization methods available that are capable of optimizing nanophotonic structures, including Particle Swarm (PSwarm), Covariance Matrix Adaptation Evolutionary Strategy (CMA-ES), and Nonlinear Mesh Adaptive Direct Search (NOMAD). NOMAD was selected to optimize this structure because it is well-suited for computationally expensive problems and allows for the use of surrogate functions.

NOMAD is a local, direct, determistic method developed by Sébastien Le Digabel, Christophe Tribes, and Charles Audet to address optimization problems that lack derivatives, have noisy parameter spaces, and are unable to give results for feasible points [19–21]. Computationally expensive optimization problems with relatively few parameters are particularly well-suited for this method.

The exact implementation of NOMAD allows for customization, but in general the algorithm builds off of the core Mesh Adaptive Direct Search (MADS) algorithm. This algorithm, shown below in Algorithm 1, consists of alternating search and poll steps on a mesh of points within the parameter space. This mesh is formed by a spanning positive set (that can produce any vector in the parameter space via a non-negative linear combination of the vectors in the set). The resolution of the mesh is adjusted to allow for both coarsely searching the space and finely polling with high resolution depending on the step on the step in the algorithm. For instance, when considering a point in the parameter space, there are two options: either the search and poll step can find a more optimal point or they cannot. If a more optimal point is not found, the point under consideration is deemed a "mesh local optimizer" and the mesh is refined to search with higher resolution. If instead a more optimal point is found, the mesh is either kept the same or coarsened to use the new parameter information to try to find an even better point.

Algorithm 1: High-level presentation of MADS

Initialization: Let $x_o \in \mathbb{R}^n$ be an initial point and set the iteration counter $k \leftarrow 0$

Main loop:

repeat

SEARCH on the mesh to find a better solution than x_k

if *the SEARCH failed* **then**

POLL on the mesh to find a better solution than x_k

if *a better solution than x_k was found by either the SEARCH or the POLL* **then**

call it x_{k+1} and coarsen the mesh

else

set $x_{k+1} = x_k$ and refine the mesh

Update parameters and set $k \leftarrow k + 1$

until *Stopping criteria is satisfied*

There are a number of different ways the general NOMAD framework can be implemented. The algorithm implementation allows for different search and poll methods to be used (standard and gradient polling, latin hypercube sampling, etc).

NOMAD also allows for the use of a surrogate function, which can reduce the computational load when optimizing computationally expensive objective functions. A surrogate function approximates the objective function values and can be used instead of explicit function evaluations, allowing for this reduced computational load during the optimization[22]. The surrogate options within the NOMAD framework are DACE, Nadaraya-Watson, and the Radial Basis Function.

To optimize the mirrored filter, the DACE surrogate function was used to reduce the number of simulation executions and minimize the computational load of the optimization. After the surrogate function is approximated, the algorithm seeks to minimize the figure of merit. The goal of this structure is to produce a single narrowband transmission peak. To direct the optimization towards this goal, the figure of merit (FOM) was defined by Equation 4.1.

Setting	Filter Optimization	Default
Surrogate Sample Points	500	20
Minimum Mesh Size	1e-3	1e-4
Initial Mesh Size	1	0.1
Surrogate Minimum Mesh Size	0.05	0.01

Table 4.2: Settings where the defaults of the Matlab implementaion of NOMAD vary from those used during the Mirrored Filter Optimization

$$FOM = \frac{\Delta_{wav}}{c.wav} + \frac{peak}{c.peak} + \frac{noise}{c.noise} + \frac{FWHM}{c.FWHM} \tag{4.1}$$

This relation seeks to maximize the intensity of a single peak at the desired wavelength ($peak$) while minimizing both the FWHM ($FWHM$) of that peak and the intensity of any additional peaks ($noise$). It also seeks to shift the maximum intensity of the peak to the intended transmission band of the filter (Δ_{wav}). Each term has a weighting factor ($c.wav$, $c.peak$, $c.noise$, and $c.FWHM$) that can be used to enhance or suppress the effect of a given term in the FOM. These weighting factors were varied during the study, but the champion filter identified had the following weighting factors: $c.wav = 0.1$, $c.peak = 1$, $c.noise = 5$, $c.FWHM = 5$ to yield a filter with $\Delta_{wav} = 0.5$ nm, $peak = 25.3\%$, $noise = 49$, and $FWHM = 15$ nm. The optimization produced a spread of FOMs, starting as high as 330 and reaching as low as 16.7.

The process for optimizing the filter structure using this FOM is illustrated in Fig 4.4. All steps are performed automatically after the optimization process is initiated, using the default settings for the Matlab adaptation of NOMAD in Table 4.2. In this method, the algorithm suggests a set of physical parameters for the filter. Lumerical's Finite Difference Time Domain simulation package (FDTD) then uses these parameters to perform a simulation to determine the filter's optical response. The resulting transmission spectrum of the filter is then analyzed by a custom peak-finding algorithm, which was developed to include both the maxima at the edges of a vector and plateaus, to make sure that all peak-like features would be properly identified and accounted for. Using the analyzed spectrum, the FOM is calculated, and used by NOMAD to suggest a new set of physical parameters. This process repeats until the convergence criteria is met.

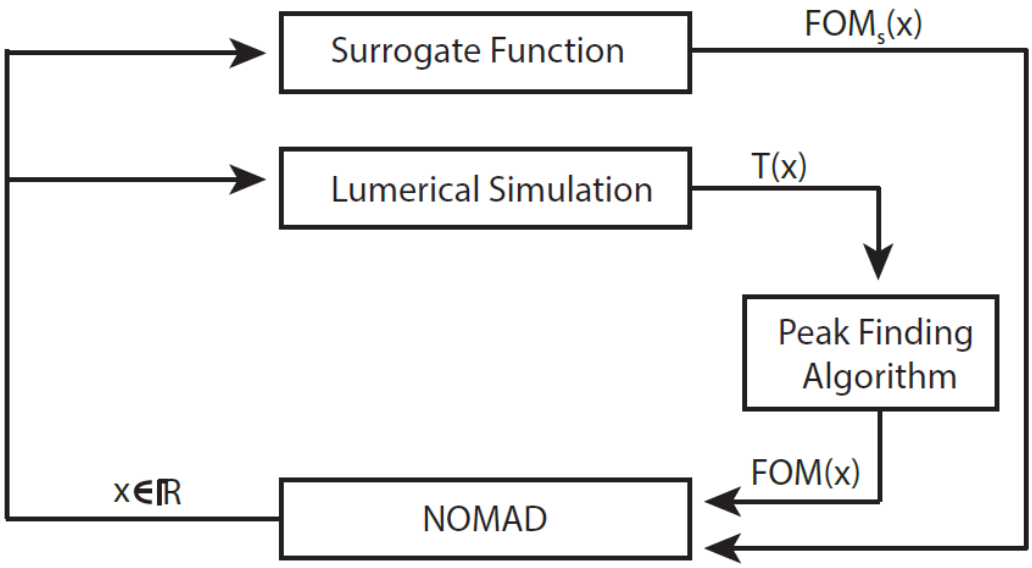

Figure 4.6: The components of the filter optimization process. The Nonlinear Mesh Adaptive Direct Search algorithm (NOMAD) determines the parameters probed to find the optimal solution. Once the physical parameters (x) are selected, they will either be evaluated by the surrogate function or a Lumerical calculation, which return the FOM to NOMAD. For each Lumerical calculation, the transmission response is analyzed by the peak finding algorithm to determine the FOM, which can then be used by NOMAD

Optimized Filter

To find the champion filter shown in Fig 4.7, five optimization parameters were varied: mirror height, mirror spacing, slit width, film thickness, and the thickness of a HfO_2 layer coating the metal filter. We also found that while additional slits can be used to improve the overall transmission intensity of the color filter, these additional slits increase the footprint of the filter, so the number of slits was fixed to one. For a filter optimized to have a single transmission peak at 550 nm, the spacing between the mirrors of this optimized filter is 618 nm. The fields of the modes supported by the structure were calculated to penetrate 46 nm into each mirror, leading to a full footprint of 710 nm.

The transmission peak of the optimized filter can be shifted across the spectrum by changing the position of the mirrors. Figure 4.8(a) shows a superposition of transmission curves for filters with different mirror spacing for linear filters in a 2D simulation environment. The superposition plot indicates there are two active transmission bands in the visible part of the spectrum, one corresponding to shorter

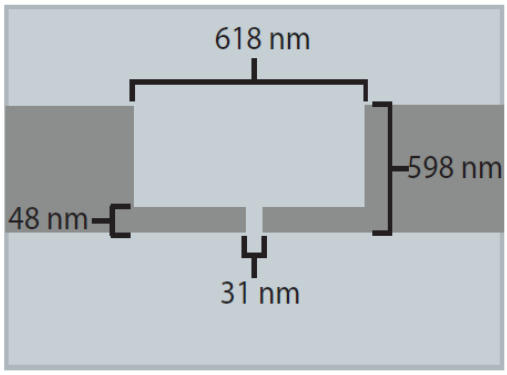

Figure 4.7: Schematic of the champion mirrored narrowband transmission filter optimized using NOMAD

wavelengths and one corresponding to longer wavelengths. The FWHM of these optimized filters varied from 14 – 26 nm across the visible spectrum. The FWHM of these filters is in large part dictated by the optical loss present in Ag. We also investigated filter design for the same structures under the assumption of a metal that acts as a perfect electric conductor. In these lossless structures, filter structures were found to exhibit FWHM values as low as 7 nm. The spectrum of an example PEC filter with a 8 nm FWHM is shown in Figures 4.9(a) and (b).

We explored the mode orders associated with these transmission bands using an eigenmode solver, and the results indicated that the shorter wavelength band is due to the lowest order cavity mode, while the longer wavelength transmission arises from the second-order cavity mode. To further illustrate the transmission response, Figure 4.8(b) shows a few representative transmission spectra for linear filters with a single slit. Between the two different transmission bands these filters possess narrowband transmission behavior across most of the visible and part of the near IR portions of the spectrum. To demonstrate that the principles at work in the performance of the two-dimensional filters also apply for three-dimensional filters comprised of two crossed slits instead of a linear slit, three-dimensional simulations were performed for the same geometrical parameters and materials used in the two-dimensional filters. The results of these simulations are shown in Figure 4.8(c) and illustrate that despite the submicron areas of three-dimensional filters, the resonant modes excited in the three-dimensional structures are similar to those seen in two-dimensional filters.

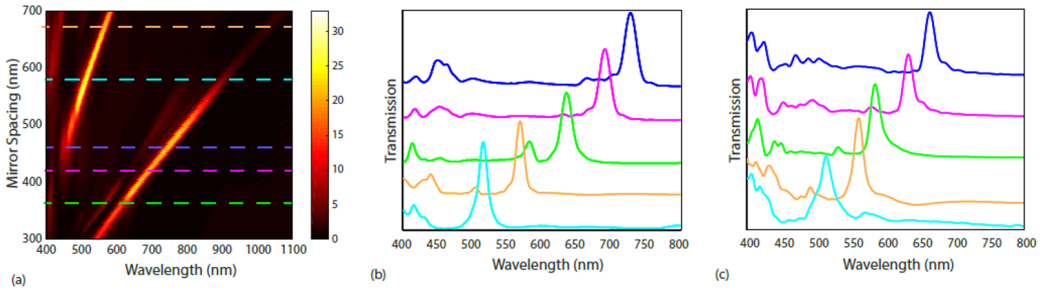

Figure 4.8: (a) A superposition of transmission plots illustrating the effect of mirror spacing on transmission peak position for 2D linear filters. There are two active mode orders in the visible spectrum, the shorter wavelength transmission band corresponds to the lowest order cavity mode and the longer wavelength band corresponds to the first higher order cavity mode (b) The simulated transmission response of the optimized 2D linear filter for a few mirrored filters spanning the visible part of the spectrum (c) The simulated transmission response of a few 3D square filters with the same mirror spacings as the filters shown in (b).

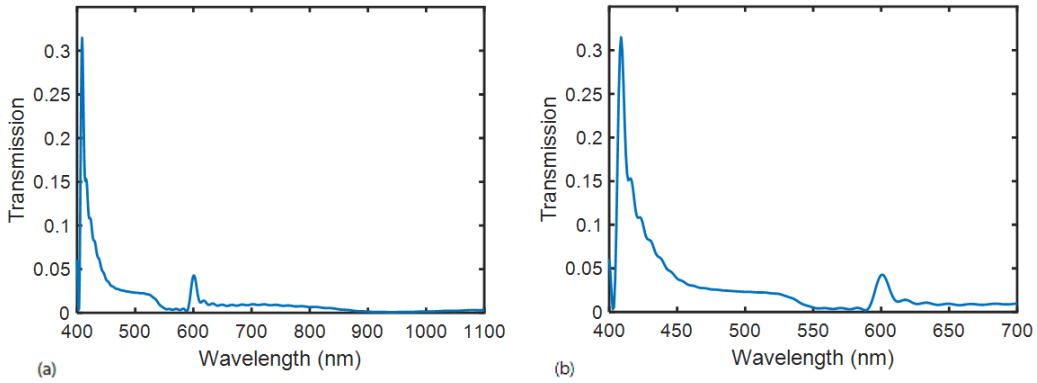

Figure 4.9: (a) The simulated transmission spectrum of a lossless filter composed of perfect electrical conductors (PECs) that possesses an 8 nm FWHM (b) The same PEC filter as (a) with a reduced view of the filter's transmission spectrum to better illustrate the behavior of the extremely narrow transmission peak. This narrow spectral response shows that ohmic loss in Ag is the cause of some of the spectral width of the champion optimized filter

4.4 Experimental Demonstration

Fabrication Method

The sidewalls of the mirrors were found to strongly affect filter transmittance. Slight changes to the mirror spacing or sidewall taper can dramatically change filter performance. To closely control the quality of the mirrors, the filters were fabricated using a novel metal imprinting method, with the process flow shown in Figures 4.10. This method produces metallic nanostructures with extremely smooth

metal surfaces on all sides. While template stripping methods are able to produce very smooth surface on one side of the metallic structure[23], the other surface has a roughness defined by metallic grain growth during vapor deposition. By contrast, our metal imprinting yields equivalently smooth surfaces on both sides which is critical to narrowband filter performance. The imprinting method was also found to yield straighter, smoother and more vertically-oriented metallic sidewalls than is achievable via either metal etching or lift-off processing.

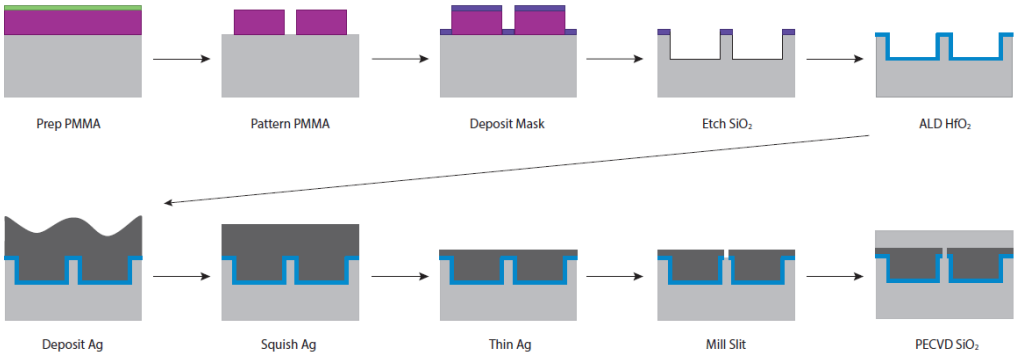

Figure 4.10: The process flow for fabricating mirrored filters. First the region between the mirrors is defined in a fused silica substrate using a pattern defined by electron-beam lithography that is subsequently dry etched. Next a thick layer of Ag is deposited and pressed into the etched regions to form the mirrors. The Ag is then thinned to the final thickness of the thing film and the slit is milled before SiO_2 is deposited on the top surface to encapsulate the Ag

The initial steps define SiO_2 structures that form the negative space around the metal mirrors using electron-beam lithography. The fused silica chips are first sonicated in acetone before being rinsed in IPA. Next a single layer of 950 A4 PMMA is spun at 1500 rpm for 1 minute and then baked for 5 minutes at 180°C. The fused silica substrate is electrically insulating, so a 5 nm Al film is thermally deposited on top of the resist to reduce charging during electron-beam patterning step. Electron-beam lithography is then used to write rectangles and squares that will eventually be the SiO_2 regions between the mirrors for 2D linear and 3D square filters respectively. After the patterning step, the Al film is removed by first etching it using 30% TMAH for 50 seconds before rinsing the substrate with DI water. The PMMA is then developed using MIBK:IPA 1:3 for 30 seconds and the substrate is rinsed in IPA.

Next, a 60 nm Cr film is deposited via electron beam evaporation at 0.6A/s in a chamber at pressure $5.3\text{x}10^{-7}$ torr. The PMMA and unwanted Cr are then removed

via lift-off using Remover PG for 5 minutes and occasional sonication. The remaining Cr film is used as an etch mask during a 1:54 m:s ICP etch in C_4F_8/O_2 that defines 598 nm tall SiO_2 pillars. The Cr etch mask is then removed by a 20 minute soak in Cr-7S etchant solution.

Once the Cr is removed, a 1 nm layer of HfO_2 is deposited via an 8 cycle deposition in an ALD. Next, 2 μm of Ag is deposited on top of the sample using electron-beam evaporation. The sample is rotated to try to ensure as conformal a deposition as possible. The height of the SiO_2 pillars prevents from completely infilling the regions between the pillars. To create Ag mirrors that are flush to the SiO_2 pillars, a wafer bonder was used to press a dummy chip of thermal SiO_2 on Si onto the Ag film. The stack is pressed together at 1500 torr and 175°C overnight, to allow the Ag to infill into the voids near the SiO_2 pillar and the top of the film to reach the smoothness of the SiO_2 on Si dummy chip. This process considerably reduces the surface roughness of metal films, Figure 4.11 shows the roughness of two Ag films that were deposited by electron-beam evaporation simultaneously. Figure 4.11(a) is an AFM scan of the Ag after it was deposited. The columnar growth mechanism in electron beam deposited leads to rough films, which is reflected by this film's RMS roughness of 5.58 nm[24]. Figure 4.11(b) shows the roughness of an Ag film that experiences the wafer bonding pressing method after deposition. The film is far smoother, as reflected by the films RMS roughness, which is an order of magnitude less than the unpressed case at 0.55 nm.

The wafer bonder process was also able to effectively infill the voids around the SiO_2, as demonstrated by the focused ion beam (FIB) cross-section shown in Figure 4.12. The grain growth under heat and pressure is evident on the top and front faces of the film the films, and the Ag is pressed flush next to the pillar.

After the Ag is pressed around the SiO_2 pillar to form the mirrors, there is a 1.48 μm thick film of Ag on top of the pillar that must be milled to the final 50 nm thickness. An Ar mill in an ICP plasma etch system was used to remove the excess Ag. Different grains in Ag etch at different rates, so the forward power was increased to its maximum value of 300W to make the etch as physical as possible The sample was milled for 6 minutes at a rate of 205 nm/min yielding a 255 nm thick film. The etch was stopped before the final 50 nm was reached to do a second pressing step to smooth out any thickness variations due to the grain texturing. The Ag film is then

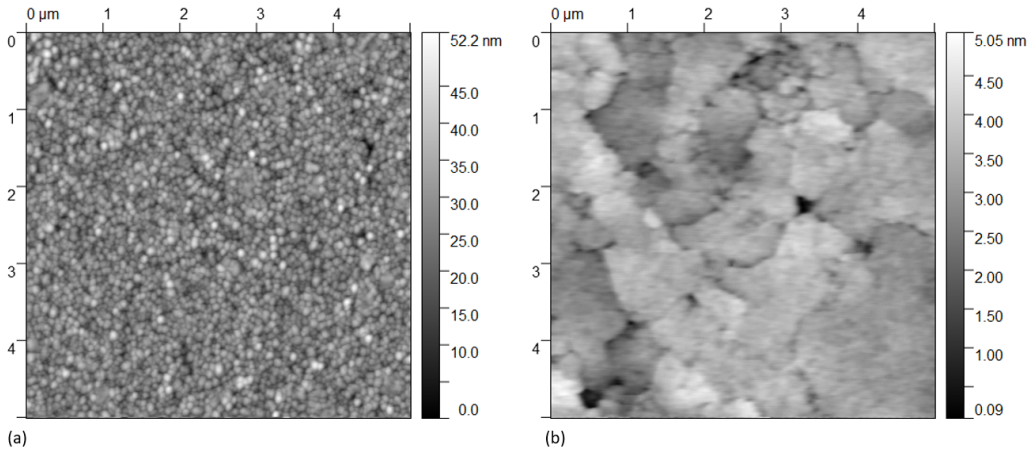

Figure 4.11: AFM scans illustrating the smoothing effect of the wafer bonder pressing process. (a) An electron beam evaporated Ag film that was not pressed. The RMS roughness is 5.58 nm. (b) An Ag film deposited in the same conditions that was then pressed at 1400 torr and held at 100°C for 6 hours.

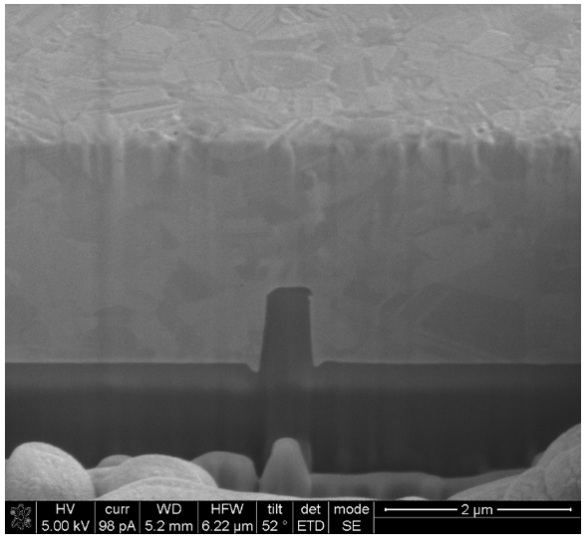

Figure 4.12: Cross-section after the Ag film is pressed in the wafer bonder. The large grains give evidence to atom mobility under the temperature and pressure conditions and the metal has been pressed up to the sides of the pillar without any evidence of gaps.

etched for another 32 seconds to bring the final thickness to 50 nm.

These 50 nm Ag films are relatively transparent to back scattered electrons generated by a 30 kV and 2.4 nA electron beam. An illustration of this transparency is shown in Figure 4.13, where an SiO_2 structure cannot be seen under low voltage and current

conditions in (a) but can be seen clearly from beneath the 50 nm Ag film when the voltage and current are increased in (b). This transparency was used to align the slit between the mirrors during the FIB process. While a 30 kV Ga beam does not generate enough back scattered electrons for visibility, by aligning the electron and ion beams to a coincident point, the proper position can be observed using the electron beam and then milled using a low current ion beam.

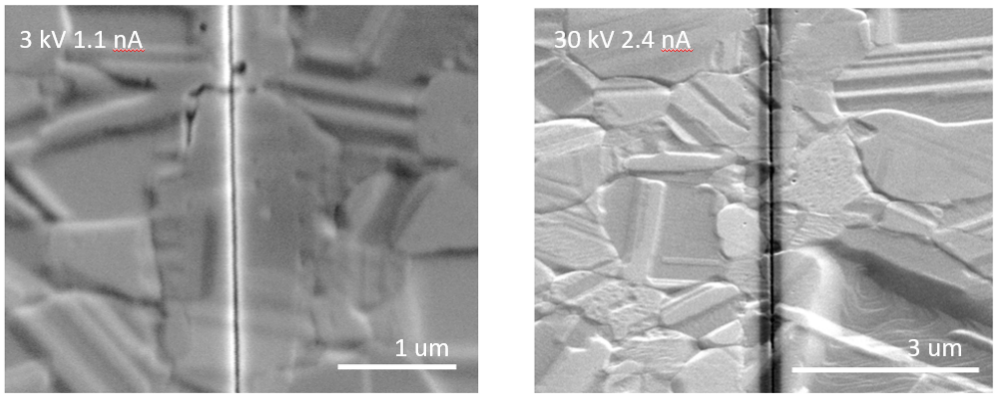

Figure 4.13: Comparing contrast of buried features in different SEM conditions (a) an SEM micrograph taken at 3kV and 1.1 nA where no patterns beneath the milled line are visible (b) an SEM micrograph taken at 30 kV and 2.4 nA where the SiO_2 pattern beneath the milled line is clearly visible.

Once the slits were milled, 1.4 μm of SiO_2 was deposited in a PECVD using SiH_4/Ar. The films deposited in the PECVD used are not conformal at the edges of chips, so to prevent the sample from oxidizing, an additional 8 nm of Al_2O_3 were deposited in an ALD to ensure the sample was completely encapsulated. To prevent the H_2O precursor to oxidize the edges during the ALD processing, the sample was first coated with extra-long pulses of the Al_2O_3 precursor and then subject to 40 cycles of 50°C Al_2O_3 depositions before depositing the final 4nm at 150°C[25]. Cross-sections of a filter prior to milling and a completed filter are shown in Figures 4.14(a) and (b) respectively.

While the fabrication process used to make the measured filters uses serial patterning systems such as electron beam lithography, focused ion milling, and makes unconventional use of a wafer bonder, these filters can be fabricated in a nanofabrication foundry environment. The electron beam lithography and focused ion milling steps can also be replaced by a two-step aligned photolithography process that defines two

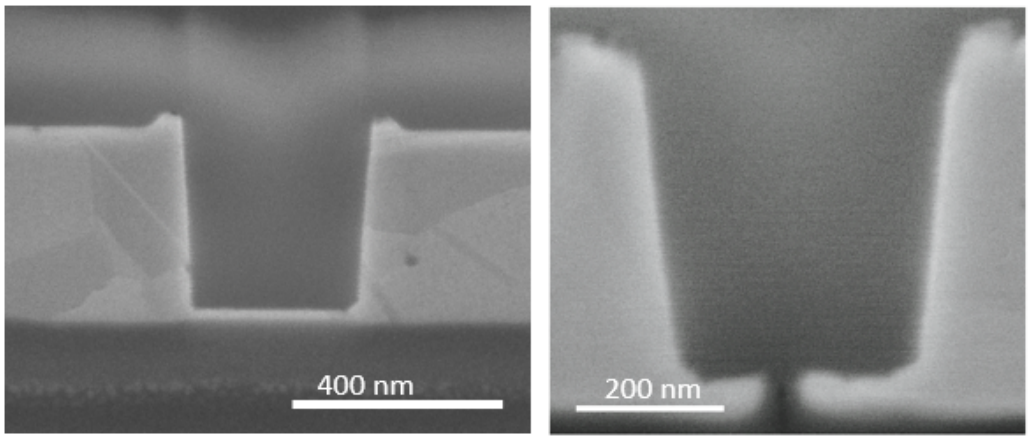

Figure 4.14: (a) Cross-section of a thinned filter prior to the aligned mill of the slit. (b) Cross-section of a completed filter. The images are both tilted to 52°, exaggerating the apparent taper. The measured tapers of the mirrors of these filters are both less than 3°.

SiO_2 pillars. During the first photolithography step, a small pillar that will become the slit can be etched onto an SiO_2 film. In the second photolithography process, a larger pillar can be defined under the small pillar to become the spacing between the mirrors. After the metal is deposited on the stacked pillars, a chemical mechanical polishing system can be used to thin the metal down and smooth it flat, leaving the top of the slit exposed, and finishing the filter with the final SiO_2 coating step.

Experimental Results

The fabricated filters were measured using a supercontinuum laser incident upon a monochromater that is focused through a home-built focusing set-up and a 50X objective to yield a Gaussian beam with a 2 μm spot size. A beam splitter directed some of the incident power to a reference diode that was used to ensure the consistent normalization of all spectra. Multiple filter geometries were measured to verify the spectral response of the simulated filters. Due to the sub-diffraction limit footprint of all filters, they were all normalized relative to 5 μm aperture. This relatively large aperture was chosen to prevent any resonant effects in the normalization spectrum.

If a smaller aperture were used, it would add resonant features into the transmission response that would be convolved with the transmission spectrum of the filter. While the 2 μm beam spot still allowed for the filters to report relatively high transmission

efficiencies, these values would be even higher if considered relative to the 1 μm footprint of state-of-the-art CMOS pixels. Normalization was also used to account for the spurious scattered background signal reported by the measurement set-up in the near-IR. More details about the measurement set-up are addressed at length in the Measurement Set-up section at the end of this chapter.

Three transmission spectra for different linear color filters are shown in Figure 4.15(a). The linear filters are polarization dependent and each have a footprint of less than 600 nm in the lateral direction. Filter 1 demonstrated peak transmission at 475.0 nm, indicating that while these filters are made with Ag, they can still perform at wavelengths less than 500 nm. The FWHM of this filter is 24.8 nm, corresponding to a resolving power of 19.2. Filter 2 shows similar behavior at peak position 512.5 nm, FWHM 30.6 nm, and resolving power 16.7. Filter 3's peak at 570.0 had a FWHM and resolving power of 31.5 nm and 18.1 respectively. There is small side-lobe on Filter 3, which we suggest is due to a slight misalignment of the filtering slit. Each filter was normalized to a 5 um square hole through the Ag and reported a normalized transmission of at least 40%, despite the sub-micron width of each slit filter. The footprint of Filter 3 is 0.65 that of Filter 2, which was used as an additional normalization factor to account for the reduced amount of light incident on that filter.

Even more importantly, the measured filters demonstrated high signal to noise ratios, indicating that they are well-suited for application in hyperspectral filtering. Figure 4.15(b) illustrates the normalized transmission spectra for filters whose transmission band varies across the visible range. These filters were measured using a transmission confocal set-up with a 5 μm circular pinhole aperture (discussed in detail in the Measurement Methods subsection), which mimics the detection configuration of color filters integrated into CMOS image sensors. In general, the measured filters show excellent agreement with simulation, and the experimental filters possess enhanced transmission that we suggest is due to the very large grains and smooth surfaces of the Ag, which reduces loss within the system[26]. The experimental filter results validate that the mirrored filter design is capable of breaking the relationship between footprint and resolving power within nanophotonic filters. These filters can produce narrowband transmission spectra with just a single period of the nanophotonic feature.

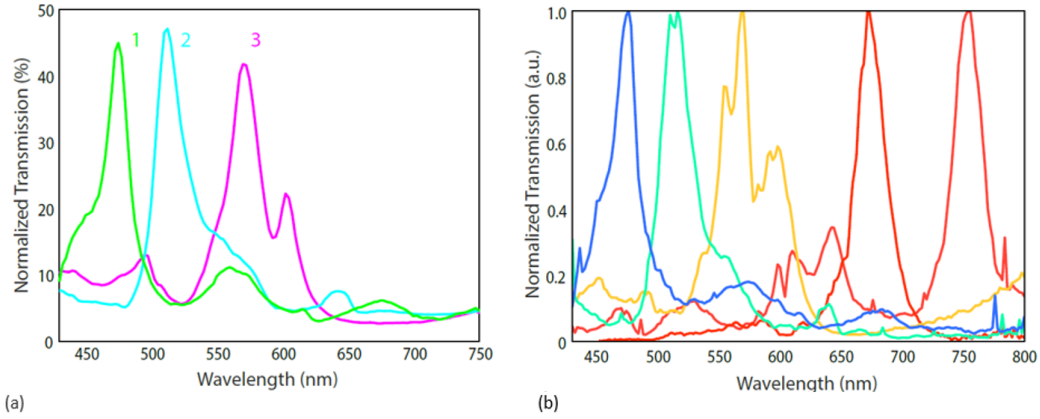

Figure 4.15: (a) Measured transmission spectra for 3 linear color filters. Each possesses a FWHM of 31 nm or less and a cross-sectional footprint of less than 600 nm (b) Transmission measurements of 5 linear color filters plotted in the CIE color of their transmission peak. Each filter was normalized to its peak transmission value to emphasize its narrow transmission bandwidth and high signal-to-noise ratio.

4.5 Extending to CMOS Applications

In a multispectral or hyperspectral image sensor, individual filters are architected in pixel arrays. A potential layout geometry is shown in Figure 4.16 in which individual square filters (Figure 4.16(a)) are arrayed into superpixels (Figure 4.16(b)) that each correspond to a single spatial coordinate, and the filters are all separated by the width of the mirrors that surround the active filtering area.

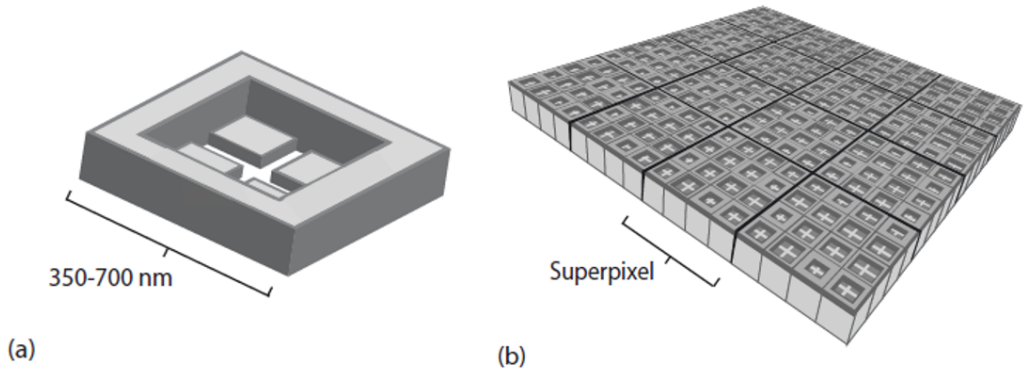

Figure 4.16: (a) A schematic of a single square filter. The footprint of each side varies from 350 – 700 nm for filters in the visible part of the spectrum. (b) Schematic of a proposed multispectral "superpixel" composed of arrays of ultracompact square filters.

A fabricated array of filters is shown in Figure 4.17. The dark grey squares are the

SiO_2 regions between the lighter gray 200 nm wide mirrors. Experimental results for the three-dimensional square filters are shown in Figures 4.18(a) and 4.18(b). In 4.18(a) the transmission results for a single square filter with mirror-to-mirror spacing of 692 nm is shown normalized to a 5 μm aperture. The transmission response demonstrates that a sharp feature can be produced, even for a sub-micron single filter. If the filter is normalized to an approximation of the amount of light incident on the actual footprint filter, the transmission intensity is nearly 70%.

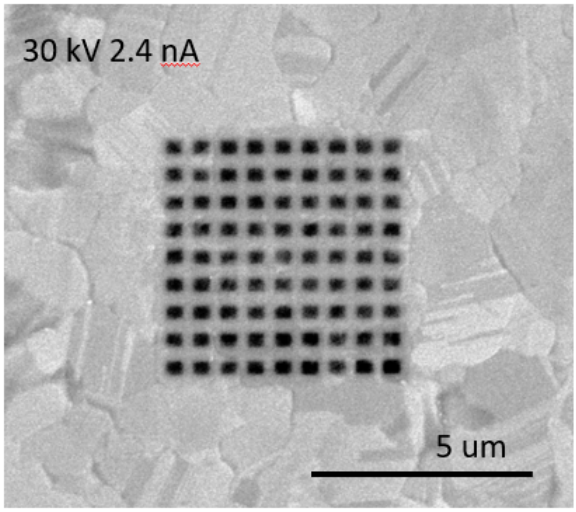

Figure 4.17: SEM micrograph of an array of square SiO_2 pillars buried beneath 50 nm of Ag. The underlying patterns are visible and can be used for alignment when imaging with a high kV electron beam.

The noise around the peak is due to fabrication imperfections in individual filters and as can be seen by comparison with spectrally-averaged measurements from multiple square filters, as shown in Figure 4.18(b), where a 2 x 2 array of the same square filters were measured. Each filter has an edge length of 424 nm and the spacing between the filters is 200 nm. The filters are each spaced less than 200 nm apart and there is no evidence of optical crosstalk between the filters. The leftmost secondary peak is evident in simulations of single pixels of this structure. Slight misalignments of the milled crosses within each filter area is responsible for the slight broadening of this peak, which is less evident in the single filter case. We suggest the other two smaller peaks are also due to these fabrication imperfections.

Calculations further demonstrate that not only can same wavelength filters be arrayed close together, so can filters targeting different wavelengths. Figure 4.19 illustrates an array of simulations where the spacing between two adjacent filters was varied

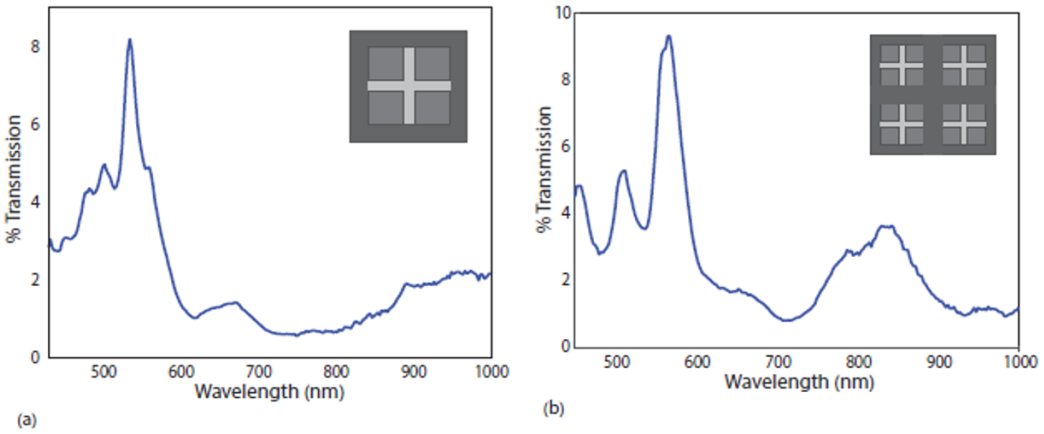

Figure 4.18: (a) Transmission spectrum for a single square filter that has an edge-length of 692 nm (b) Transmission spectrum for a 2 x 2 array of square filters. Each filter has edge-lengths of 424 nm and they are spaced 200 nm apart. The single narrow peak experimentally verifies that square filters produce the expected response and arrays of pixels do not possess optical crosstalk.

from 10 nm to 70 nm. The two peaks at 612.2 and 718.1 nm correspond to the transmission bands of the individual filters. Once the spacing between the filters exceeds the skin depth of Ag, 50 nm at these wavelengths, there is no evidence of optical crosstalk between the filters. This indicates that in a device, filters can be spaced as close as 50 nm apart without introducing artifacts from optical crosstalk.

The above discussion focused on designing and demonstrating a narrowband small-footprint filter in the visible part of the spectrum. In other parts of the spectrum other materials systems are available to produce similar results. For example, farther into the IR a Cu and SiO_2 filter produces the same narrowband transmission results. Figure 4.20(a) shows a superposition of transmission spectra for different Cu mirror spacings and Figure 4.20(b) shows a single narrowband spectral response of an individual Cu filter.

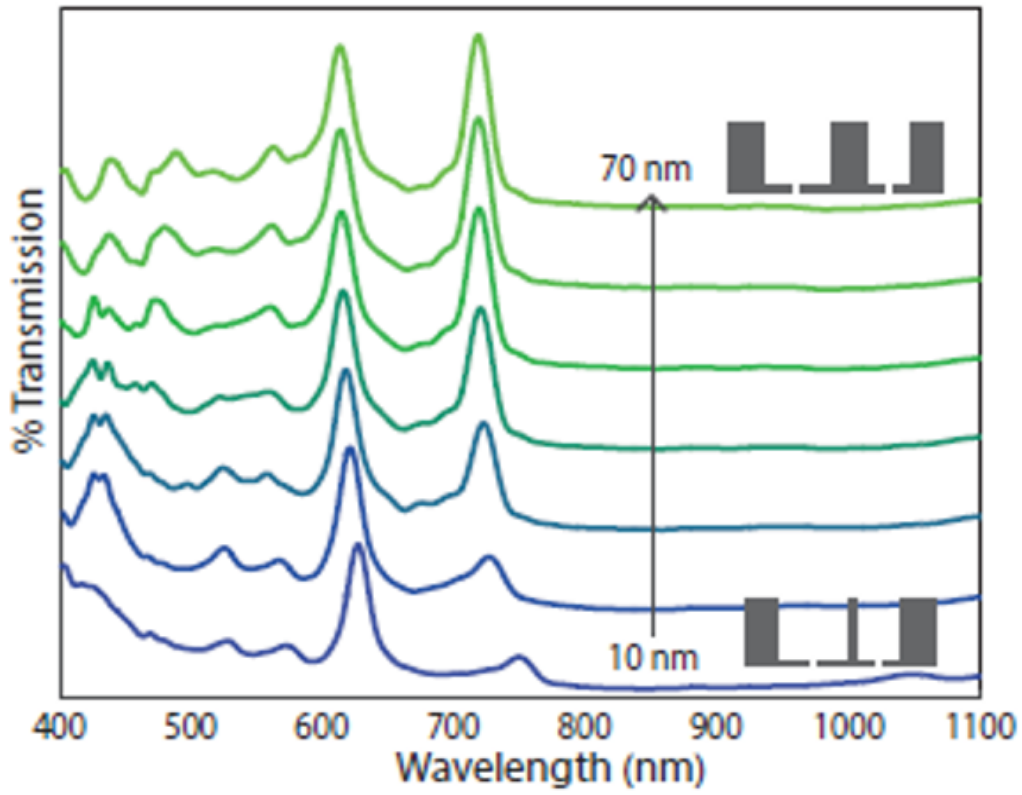

Figure 4.19: Calculated crosstalk between two spectrally distinct linear filters. The width of the mirror separating the two active filter areas varies from 10 nm (blue) to 70 nm (green). There is no evidence of optical crosstalk in filters spaced at least 50 nm apart.

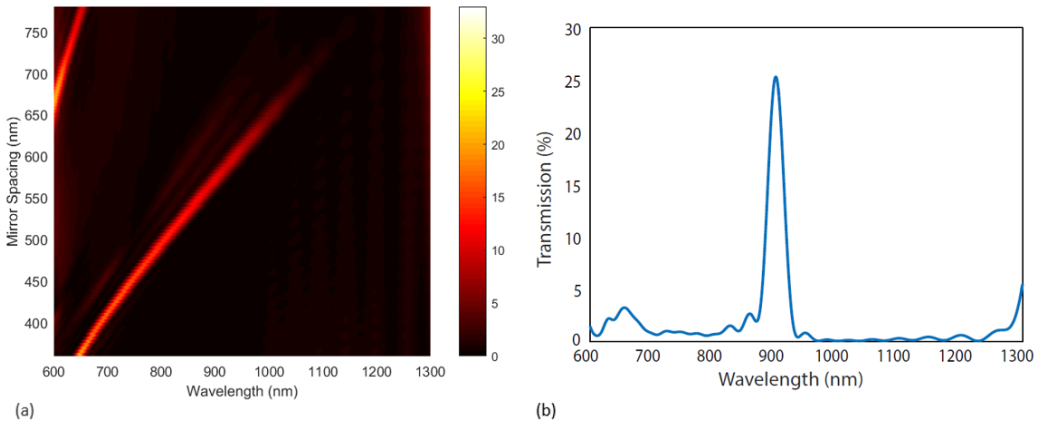

Figure 4.20: (a) A superposition of Transmission Spectra for Varying Mirrors Spacings in Cu filters (b) A representative single spectral response of a single optimized Cu filter.

4.6 Conclusions, Future Directions, and Outlook

By coupling an in-plane Fabry-Perot resonator to a surface plasmon polariton mode, and utilizing a novel metal imprint fabrication method for filter fabrication, we were able to design ultracompact narrowband transmission color filters that break the relationship between footprint and resolving power. Filters were experimentally shown to achieve narrowband spectral filtering and function in pixel arrays. The filtering mechanism is not dependent on any absolute length scale, so larger filters can be used to filter longer wavelength light utilizing Ag or other materials systems. Additionally, while these filters are static, introducing a gate-tunable dielectric like ITO could potentially be used to spectrally tune the peak transmission wavelength, and thus increasing the number of spectral bands captured without reducing the spectral resolution of the sensor.

4.7 Measurement Methods

The custom-built optical transmission measurement set-ups used in this work are shown schematically in Figure 4.21. In this configuration, a beam supplied by a NKT SuperK Extreme white laser was monochromated with variable slit width to give a constant bandpass of 2 nm, collimated, expanded by two 90 degree off-axis parabolic mirrors, and finally focused onto the sample with a long working distance, low-NA objective (Mitutoyo Plan Apo 50X, Tube Length 200mm, NA=0.55). A CMOS (IDS UI-1460SE) camera was used to experimentally characterized the beam shape at the focal plane and verified it had a FWHM of 2 μm.

A calibrated Si photodetector (Newport 818-ST2-UV) was used to measure the power transmitted through the filter, as well as the reference 5μm aperture. During all measurements the beam was sampled with a glass slide and measured with a Si reference photodiode for simultaneous recording of the beam photocurrent, allowing correction of any fluctuations in the laser power between a normalization measurement and measurement of the samples. A chopper, typically at a frequency of 95Hz, was used to modulate the incident beam, and provide a reference frequency to two Stanford Research Systems SR840 lock-in amplifiers. An external, low-noise current-to-voltage transimpedance amplifier was used to feed both photodiode signals to the respective lock-in amplifier. The lock-in amplifiers were used to filter the modulated signal from other potential noise signals in the photodiode responses.

For the SNR measurements shown in Figure 4.15(b), the background signal needed

to be attenuated as much as possible. To achieve this, the optical transmission set-up described above was further modified into a transmission confocal microscopy configuration shown in Figure 4.21(c). The same monochromatic and collimated beam was redirected 180° via mirrors to enter the objective passing through its focal point. A second objective (Mitutoyo Plan Apo 2X, Tube Length 200 mm, NA=0.05) focused and collimated the beam at the focal spot. The back side of the filter being measured was placed at the focal point of the high N.A. objective, creating a transfer function of the transmitted light. This collimated beam was refocused with a 100 mm focal length plano-convex lens to form an image of the transmitted light.

A 5 μm pinhole was placed in this image plane. The portion of the image transmitted by the pinhole was controlled by translating the sample, rather than the pin-hole in the image plane. Due to the tube length being larger than 200 mm, the actual magnification of this image was about 62x. The equivalent diameter of the aperture with respect to the magnified image was about 5μm as measured by the CMOS camera. A low dark current photodiode was used behind this pinhole to measure the transmitted photocurrent through the lock-in amplifier system. The imaging objective was calibrated for chromatic focal shifts and the position of the objective was adjusted with sub-micrometer steps to further reduce chromatic aberrations. Peak normalized signal-to-noise (SNR) plots were created using this method because it significantly increased spatial signal contrast and greatly reduced the background spectrum such that sub-percent peaks could be detected without a loss in SNR. The normalization spectrum for each filter was measured on an area of the fused silica superstrate where no Ag film existed, which accounted for the reflection of the superstrate.

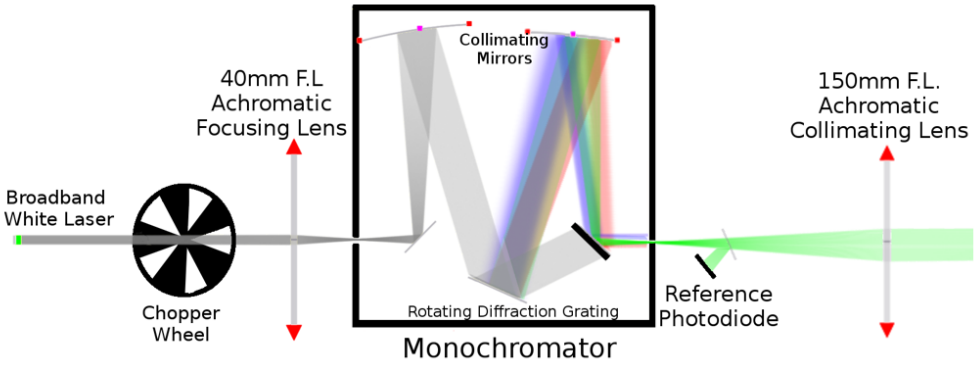

(a)

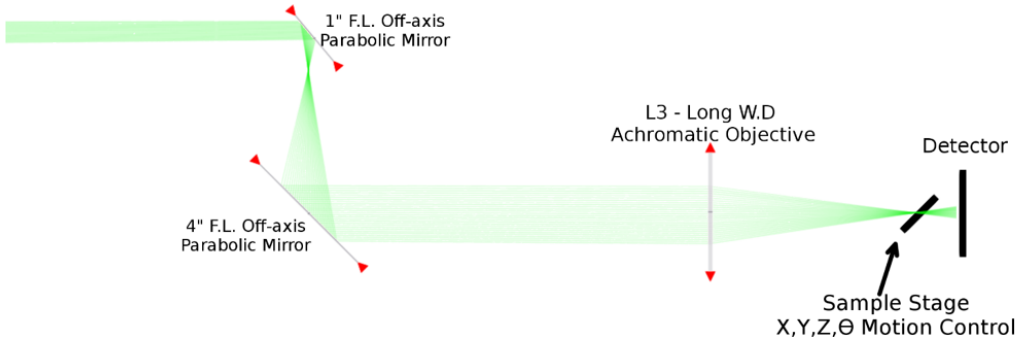

(b)

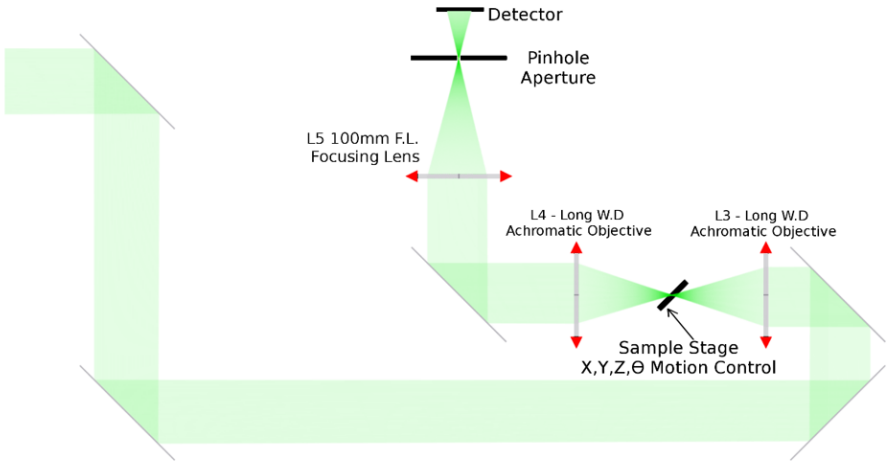

(c)

Figure 4.21: (a) Schematic of the optical set-up depicting the monochromation and collimation of the light beam and the collection of the reference signal. (b) Schematic of the focusing of light onto the sample and the collection of the transmitted signal with a Si Photodetector. (c) Schematic of the confocal transmission microscopy configuration. The ultracompact Ag filter transmits light into the high N.A. objective and it is imaged onto a pinhole aperture which selects a 5um diameter portion of the image signal.

References

[1] Gordon E Moore. “Cramming more components onto integrated circuits”. In: *Proceedings of the IEEE* 86.1 (1965), pp. 82–85.

[2] David A Thompson and John S Best. “The future of magnetic data storage technology”. In: *IBM Journal of Research and Development* 44.3 (2000), p. 311.

[3] Jeff Hecht. “Is Keck’s law coming to an end”. In: *IEEE Spectrum* (2016), pp. 11–23.

[4] Yu Horie et al. “Visible wavelength color filters using dielectric subwavelength gratings for backside-illuminated CMOS image sensor technologies”. In: *Nano letters* 17.5 (2017), pp. 3159–3164.

[5] Sozo Yokogawa, Stanley P Burgos, and Harry A Atwater. “Plasmonic color filters for CMOS image sensor applications”. In: *Nano Letters* 12.8 (2012), pp. 4349–4354.

[6] Qin Chen et al. “Nanophotonic image sensors”. In: *Small* 12.36 (2016), pp. 4922–4935.

[7] Woo-Yong Jang et al. “Experimental Demonstration of Adaptive Infrared Multispectral Imaging using Plasmonic Filter Array”. In: *Scientific reports* 6 (2016), p. 34876.

[8] Dmitry Yudovsky, Aksone Nouvong, and Laurent Pilon. *Hyperspectral imaging in diabetic foot wound care*. 2010.

[9] AA Gowen et al. “Hyperspectral imaging–an emerging process analytical tool for food quality and safety control”. In: *Trends in Food Science & Technology* 18.12 (2007), pp. 590–598.

[10] E Keith Hege et al. “Hyperspectral imaging for astronomy and space surviellance”. In: *Imaging Spectrometry IX*. Vol. 5159. International Society for Optics and Photonics. 2004, pp. 380–392.

[11] Dagny Fleischman et al. “Hyper-selective plasmonic color filters”. In: *Optics Express* 25.22 (2017), pp. 27386–27395.

[12] SS Wang and R Magnusson. “Theory and applications of guided-mode resonance filters”. In: *Applied optics* 32.14 (1993), pp. 2606–2613.

[13] Daniel B Mazulquim et al. “Efficient band-pass color filters enabled by resonant modes and plasmons near the Rayleigh anomaly”. In: *Optics express* 22.25 (2014), pp. 30843–30851.

[14] H Angus Macleod and H Angus Macleod. *Thin-film optical filters*. CRC press, 2010.

[15] Jon Olav Grepstad et al. “Finite-size limitations on quality factor of guided resonance modes in 2d photonic crystals”. In: *Optics Express* 21.20 (2013), pp. 23640–23654.

[16] Yeo-Taek Yoon and Sang-Shin Lee. “Transmission type color filter incorporating a silver film based etalon”. In: *Optics Express* 18.5 (2010), pp. 5344–5349.

[17] Beibei Zeng, Yongkang Gao, and Filbert J Bartoli. “Ultrathin nanostructured metals for highly transmissive plasmonic subtractive color filters”. In: *Scientific reports* 3 (2013), p. 2840.

[18] Jay H Barton et al. “All-dielectric frequency selective surfaces with few number of periods”. In: *Progress In Electromagnetics Research* 41 (2012), pp. 269–283.

[19] Luis Miguel Rios and Nikolaos V. Sahinidis. “Derivative-free optimization: a review of algorithms and comparison of software implementations”. In: *Journal of Global Optimization* 56.3 (2013), pp. 1247–1293.

[20] Charles Audet and Jr. J. E. Dennis. “Mesh Adaptive Direct Search Algorithms for Constrained Optimization”. In: *SIAM Journal on Optimization* 17.1 (2006), pp. 188–217.

[21] Sébastien Le Digabel. “Algorithm 909: NOMAD: Nonlinear Optimization with the MADS Algorithm”. In: *ACM Trans. Math. Softw.* 37.4 (2011), 44:1–44:15.

[22] A. J. Booker et al. “A rigorous framework for optimization of expensive functions by surrogates”. In: *Structural optimization* 17.1 (1999), pp. 1–13.

[23] Jong Hyuk Park et al. “Fabrication of smooth patterned structures of refractory metals, semiconductors, and oxides via template stripping”. In: *ACS applied materials & interfaces* 5.19 (2013), pp. 9701–9708.

[24] AG Dirks and HJ Leamy. “Columnar microstructure in vapor-deposited thin films”. In: *Thin Solid Films* 47.3 (1977), pp. 219–233.

[25] Joshua D Wood et al. “Effective passivation of exfoliated black phosphorus transistors against ambient degradation”. In: *Nano letters* 14.12 (2014), pp. 6964–6970.

[26] Kevin M McPeak et al. “Plasmonic films can easily be better: rules and recipes”. In: *ACS photonics* 2.3 (2015), pp. 326–333.

Chapter 5

THE COOKBOOK

> Well, all I know is this—nothing you ever learn is really wasted, and will sometime be used.
>
> Julia Child

I spent a lot of time during my PhD thinking about making things, attempting to make things, failing to make things, and occasionally succeeding at making things. While some of those successes are addressed with some detail in other chapters of this thesis, a lot of the gritty specifics of what I did were not. In attempt to help facilitate knowledge transfer, I compiled a lot of fabrication specifics into this chapter. To make things clear, for the most part each section has the components and supplies that are needed, and the steps I'd recommend following. A cookbook, if you will.

Most of the recipes in this chapter were adapted from elsewhere. They're all cited and many of these references contain a lot of very useful details. Recipes without citations are either things I came up with or things so basic and general that I couldn't find any relevant references. If you are reading this because you want to make something and are only inclined to look up a single reference, I highly recommend the etch bible[1]—a paper I have looked at more than any other during the course of my PhD.

5.1 Substrate Cleaning Methods

Cleaning Germanium Substrates

Method adapted from the following reference[2].

Ingredients	Supplies
• Germanium Substrate	• 2 acid safe beakers
• DI Water	• 2 base safe beakers
• Hydrogen Peroxide (H_2O_2)	• 1 set of acid safe tweezers
• Hydrochloric Acid (HCl)	• 1 set of base safe tweezers

Instructions

Note: you need an acids bench and bases bench in close proximity to do this (or a bench that can safely accommodate both).

1. Prep both benches. The acids bench needs two beakers large enough to accommodate the Ge. Fill one beaker with DI water and another with 1:3 DI:HCl. On the bases bench, fill one beaker with DI and another with H_2O_2.

2. At the bases bench, dip the Ge in DI for 30 seconds to remove the native oxide layer and then dip in H_2O_2 to grow a fresh oxide. Quickly rinse with DI to remove the H_2O_2 and N_2 dry the sample.

3. Transfer the sample to the acids bench, and using fresh acid safe tweezers, dip the Ge into HCl. After 10 minutes, remove the Ge from the HCl, rinse with DI, N_2 dry, and immediately put it under vacuum.

Cleaning Silicon Substrates

Ingredients	Supplies
• Si Substrate	• 2 acid safe beakers
• DI Water	• 2 HF safe teflon containers
• Nanostrip	• 1 set of acid safe tweezers
• Hydrofluoric Acid (HF)	• 1 set of HF safe tweezers

Instructions

Note: you need an acids bench an HF bench in close proximity to do this (or a bench that can safely accommodate both).

1. Prep both benches. The acids bench needs two beakers large enough to accommodate the Si. Fill one beaker with DI water and another with Nanostrip. On the HF bench, fill one teflon container with DI and another with HF.

2. At the acids bench, drop the Si chip into the nanostrip beaker. After 5 minutes, remove the Si from the nanostrip and rinse thoroughly with DI water.

3. Transfer the sample to the HF bench, and using fresh HF safe tweezers, dip the Si into HF. Periodically try dipping the Si into DI. The Si should be fairly hydrophyllic after the nanostrip clean, but once the SiO_2 is removed, the sample will become hydrophobic. Once the oxide is removed, N_2 dry the sample and immediately put it under vacuum.

Cleaning Fused Silica Substrates

Ingredients	Supplies
• Fused Silica Substrate • Acetone • Isopropyl Alcohol	• 1 sonicator • 2 solvent beakers • 1 set of solvent safe tweezers

Instructions

1. Sonicate fused silica chip in a beaker full of acetone for 5 minutes
2. Rinse chip in IPA and then N_2 dry

5.2 Flat Metals

AgO Seed Layer

Ag does not deposite smoothly on many common substrates (the native oxide on Si, for example). This method first deposits a thin layer of AgO, which wets far better to SiO_2 than Ag. Because AgO is not vacuum stable, if the film is left under vacuum, the O_2 will pump out and leave a smooth Ag film. When the rest of the film is deposited onto this seed layer, the final result is far smoother than just depositing Ag directly onto the substrate. This method was adapted from the following reference [3].

Ingredients	Supplies
• Substrate	• E-beam Evaporator w/O_2 flow
• Oxygen Gas	
• Silver	

Instructions

1. To deposit the AgO seed layer flow in as much O_2 as the deposition system will accommodate. In the system I used, the deposition interlock was at 1E-4 torr, so I would flow enough O_2 so the chamber pressure hovered around 9.8E-5 torr before the deposition started. With the O_2 flowing, deposit 2 nm of Ag at 0.1 A/s.

2. Pump the O_2 out of the film by pausing the deposition process and leaving the substrate under vacuum for 10 minutes. During this step, the chamber pressure would usually get down to approximately 2E-7 torr.

3. Deposit the remaining Ag without a gas flow at a rate of 1 A/s.

Template Stripping

This is a very convenient way to get smooth metal substrates if you don't mind having epoxy as a part of your materials stack. With minimal effort my samples would always have RMS roughness less than 1 nm. This method works for metals that have low surface adhesion to a given substrate. I was able to do it successfully for gold and silver using native SiO_2 on Si as a substrate, but there are lots of other feasible combinations. I have used this method using both optical and thermal epoxy. Optical is easier but there are circumstances where thermal is preferred. There are many reports in the literature using this or similar methods and the following are a few representative references [4, 5].

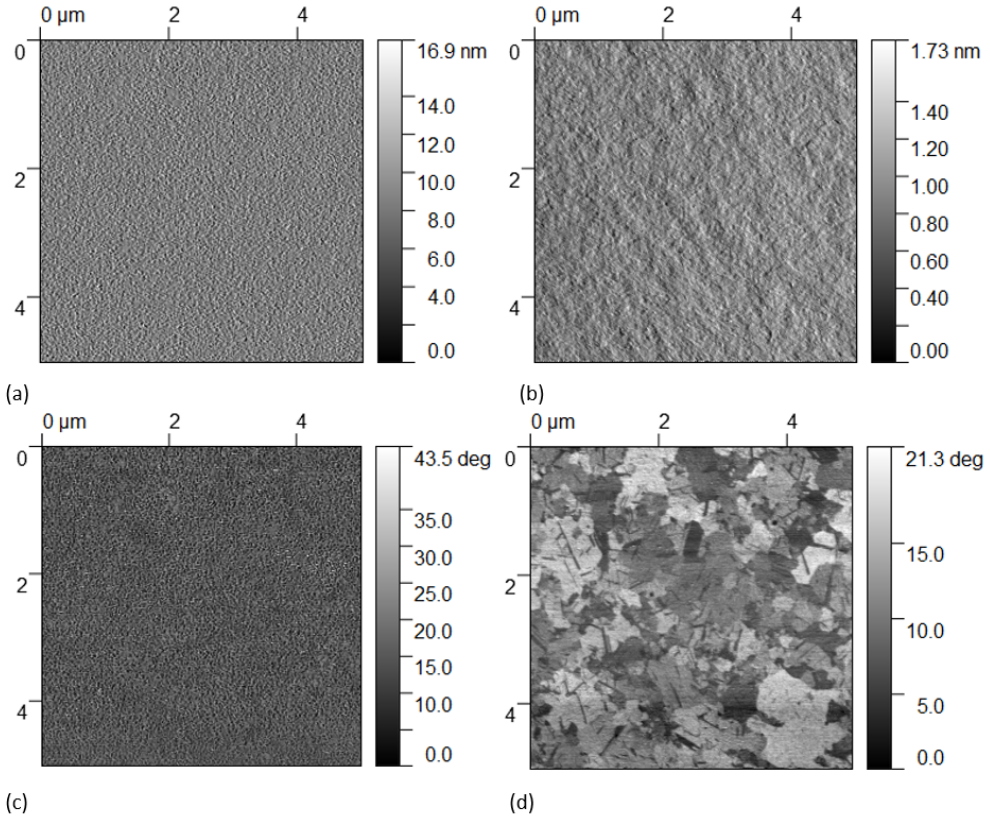

Figure 5.1: AFM scans showing two sides of a template Au stripped film. (a) and (b) show the amplitude scans for an as deposited unstripped and stripped sides of Au film respectively. The unstripped side of the film has an RMS roughness of 2.2 nm and the stripped side has an RMS of 0.87 nm. (c) and (d) are the phase retraces for the unstripped and stripped sides of the film. The clear grains in the stripped film is a further indication of how much more smooth the stripped Au is.

Ingredients	Supplies
• Si substrate	• E-beam Evaporator
• Gold or Silver	• UV lamp/Hot Plate
• Optical or Thermal Epoxy	• Sonicator
• Acetone	
• Isopropyl Alchohol	

Instructions

1. Clean Si substrate using *Cleaning Fused Silica Substrates* recipe
2. Deposit metal using an electron beam evaporator (thermal evaporation would also work)
3. Clean glass slide using *Cleaning Fused Silica Substrates* recipe. I recommend depositing on Si chips larger than my glass slides to allow for easier stripping.
4. Put one small drop of epoxy on to sample, a little bit goes a very long way so restraint is advisable here
5. Place cleaned glass chip on top and force out the bubbles by pressing the center of the glass chip with a pair of tweezers
6. If using optical epoxy (I used NOA 88-8801) put sample under a UV lamp for 3 hours. If using thermal epoxy (I used Epo-Tek 375) follow the epoxy instructions (I cured it at 80°C).
7. Use edge of the razor blade to remove glass slide. It is often possible to use the edge of the razor to apply enough force to the glass slide to get the film to strip without risking scratching the film.

Wafer Bonder

This method is a bit of a hack, but one that has worked very well for me. It produces smoother Ag than the AgO seed method and unlike template stripping it doesn't introduce any additional materials to the stack. I've tried this with both silver and copper, and it should work with gold and other metals that don't adhere well to SiO_2.

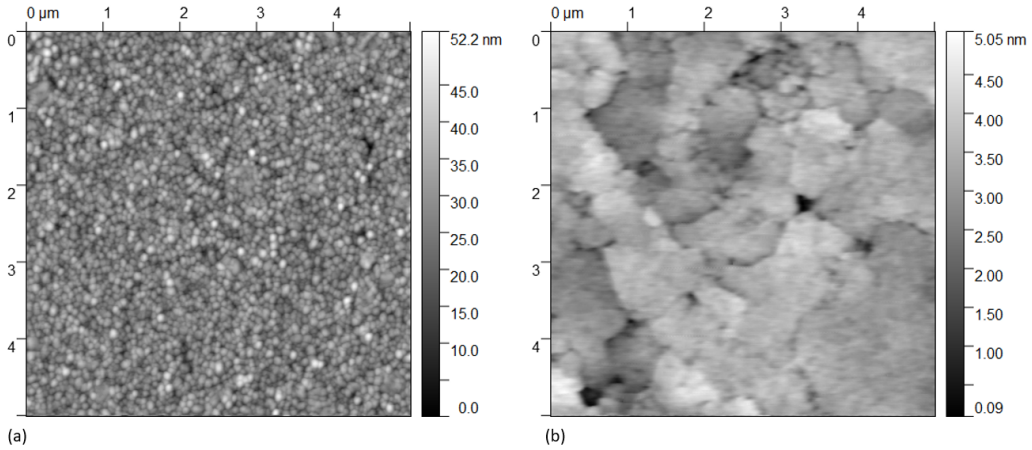

Figure 5.2: AFM scans illustrating the smoothing effect of the wafer bonder pressing process. (a) An electron beam evaporated Ag film that was not pressed. The RMS roughness is 5.58 nm. (b) An Ag film deposited in the same conditions that was then pressed at 1400 torr and held at 100°C for 6 hours

Ingredients	Supplies
• Sample	• E-beam Evaporator
• Metal	• Sonicator
• SiO_2 on Si chip	• Wafer Bonder
• Carbon Paper	

Instructions

1. Deposit metal using an electron beam evaporator onto the sample (thermal evaporation would also work). The sample can have features on it, but if so, make sure the deposited metal considerably thicker than the tallest feature. For reference: I deposited 2 μm on a sample that had 600 nm features.

2. Clean SiO_2 on Si chip using *Cleaning Fused Silica Substrates* recipe. The chip must be larger than your sample or your sample will shatter in the wafer bonder. I used about 500 nm of thermal SiO_2 on Si chips, because there was

a cassette full of them no one was using, but I would expect this method to work with any Si chips as long as there was a continuous layer of SiO_2 on it.

3. Put a piece of carbon paper that is larger than your sample on the bottom chuck of the wafer bonder. Put your sample on centered on the carbon paper with the Si chip on top of it. Close the wafer bonder and set the height such that the stack is in contact when the tool is in the down setting.

4. The recipe format I recommend is: pump down the wafer bonder to 1.5E-2 torr, have the tool come into contact, first apply pressure, then apply heat, then remove heat, then remove pressure. There is a lot of flexibility with the temperature and heat that will smooth films and infill structures. To just make smooth films I had success at 1400 torr and 100°C for 6 hours. To infill structures I would press at 1500 torr and 175°C overnight[1].

[1]It is worth mentioning that there is a such thing as "too much". If too much pressure or heat is applied the chip will bond to the film.

5.3 Bilayer Nanoparticle Liftoff

This general method is a pretty common way to get good lift-off. You can see example results in the following reference [6]

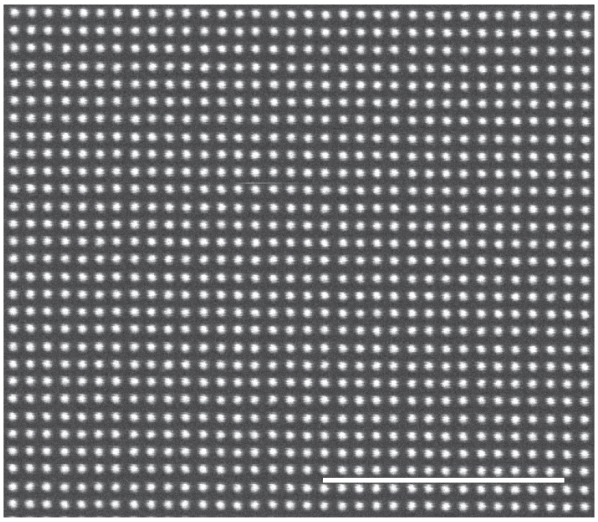

Figure 5.3: SEM image of Au nanoparticles on a Si substrate. The scale bar is 1 μm

Ingredients	Supplies
• Clean Si Substrate(s)	• 1 set of solvent safe tweezers
• 495 A4 PMMA	• 2 Pipettes
• 950 A2 PMMA	• Spinner
• MIBK:IPA 1:3	• Hot Plate
• Remover PG	• E-beam Lithography System
• Acetone	• 2 solvent beakers
• Isopropyl Alcohol	• E-beam Deposition System
• Chrome	• Acetone Squirt Bottle
• Gold	

Instructions

1. Mount clean silicon substrate onto the spin coater chuck. Use a pipette to dispense enough drops of 495 A4 PMMA to coat the substrate. Spin the substrate at 3500 RPM for 1 minute and then bake on the hot plate at 180 °C for 5 minutes. Let cool for 1 minute.

2. Mount the freshly spun substrate on the spin coater chuck. Use a fresh pipette to dispense enough drops of 950 A2 PMMA to coat the substrate. Spin the substrate at 3500 RPM for 1 minute and then bake on the hot plate at 180 °C for 5 minutes. Let cool for 1 minute.

3. Use an electron beam lithography system to write the desired pattern onto the PMMA. The parameters will vary substantially based on what type of system is used. To give a starting point, I successfully wrote nanoparticles using 500 pA and 700 pA beams and doses varying from 640 - 1040 μC/cm^2.

4. Develop PMMA using MIBK:IPA 1:3 developer. Nanoparticle arrays can successfully be made using room temperature developer or cold developer. At room temperature, the sample should be dunked in the developer for 30 seconds before immediately rinsing in IPA and N_2 drying. When using cold developer, I usually put it in the a 4.5 °C at least 12 hours before development. When ready to develop, the bottle can be left at room temperature for 2 minutes before submerging the chip in the developer for 30 seconds. Immediately after developing, rinse the chip with IPA and N_2 dry.

5. To deposit the metal nanoparticles, I recommend using a deposition system with a long chase to reduce the sidewall deposition. For the same reason, I also recommend keeping substrate rotation off for the same reason. The rest of the deposition parameters will vary based on which materials will be deposited. As an example, when depositing Au with an adhesion layer, I would first deposit 3 nm of Cr at 0.5 A/s before depositing 30 nm of Au at 1 A/s.

6. To lift-off the unwanted metal and leave just the nanoparticles on the substrate, use heated Remover PG. Note, the flash point of Remover PG is 88 °C so be very careful while heating. Let the temperature oscillate between room temperature and as high as you're comfortable going if the film isn't quickly lifting off. You can also score around the edges of the chip if there are no important features there. Once the film is lifted off, dunk the chip in a beater of acetone. While it is submerged, use an acetone squirt bottle to blast away any remaining metal flakes. Then rinse in IPA to remove the acetone before N_2 drying.

5.4 Electron Beam Lithography on Insulating Substrates

A representative at Raith told me about this method, so I'm not sure how to properly cite it. This method will not work for any base developed resists.

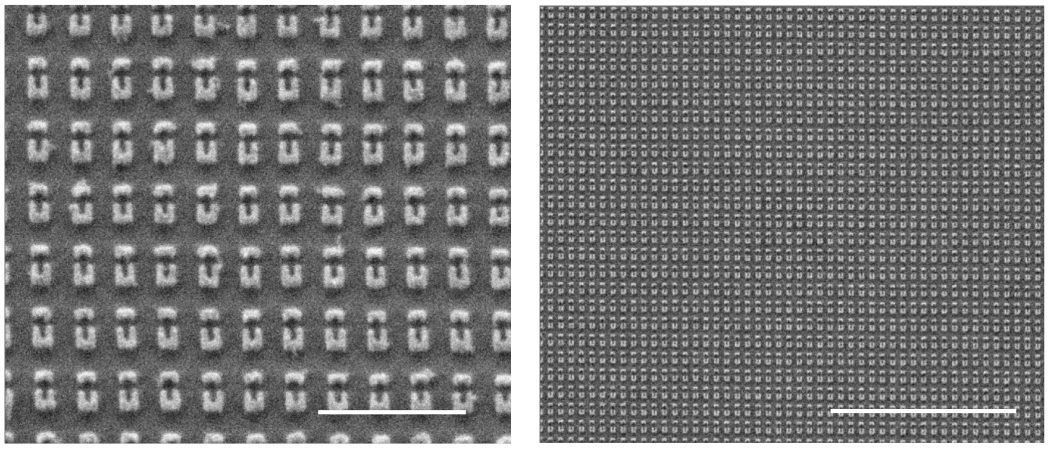

(a) (b)

Figure 5.4: SEM images of Au split ring resonators patterned in Er doped insulating YAG substrates. Using this method, features with sharp corners and spacings as small as 10 nm were successfully patterned. (a) The gap between the resonators is 20 nm and the scale bar is 1 μm. (b) The gap between the resonators is 80 nm and the scale bar is 5 μm

Ingredients	Supplies
• PMMA coated substrate	• Base safe tweezers
• Aluminum	• 2 base beakers
• Tetramethylammonium Hydroxide	• Solvent safe tweezers
• DI Water	• 2 solvent beakers
• MIBK:IPA 1:3	• Thermal Evaporation System
• IPA	

Instructions

1. Thermally evaporate 5 nm of Al at 0.4 A/s on top of the PMMA coated substrate. Thermal evaporation doesn't produce as much higher energy radiation so it is less likely to expose the resist than electron beam evaporation.

2. Expose the patterns in an electron beam lithography system. I highly recommend running a Monte Carlo simulation on the substrate + resist + Al stack

and using the results to run a proximity effect correction on the pattern prior to patterning to make sure the scattering events at the Al layer don't overexpose parts of the pattern.

3. Remove the Al layer using TMAH. Dunk the chip into a beaker of TMAH and watch the film to see when it dissolves. It usually takes about 50 seconds. Once there is no more evidence of the film, rinse the substrate in DI wafer and N_2 dry.

4. Develop normally. For PMMA, develop chip in room temperature MIBK:IPA 1:3 for 30 seconds, rinse in IPA, and then N_2 dry.

5.5 Deposition Recipes for Multilayer Structures

Multilayer Slot-Mode Plasmonic Color Filters

The following is the deposition conditions for the MSPF color filters. After the deposition step, the filters were milled in a Ga^+ focused ion beam to create the slit array[7].

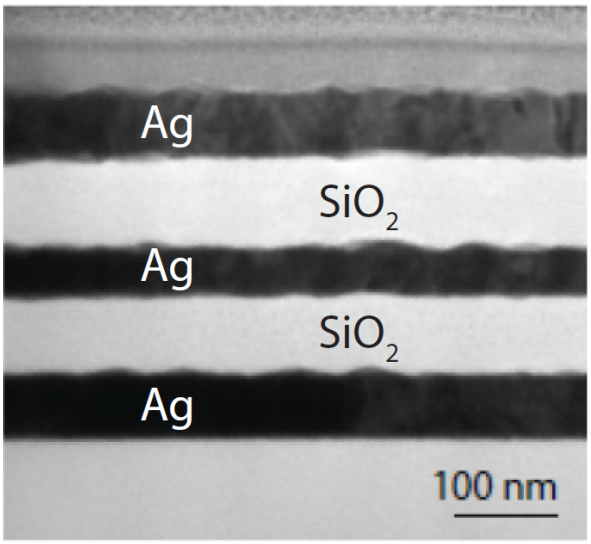

Figure 5.5: TEM micrograph of the MSPF color filter fabricated using the deposition recipe in the table below

Ingredients	Supplies
• Clean fused silica substrate • E-beam Ag source • E-beam SiO_2 source • O_2 gas	• E-beam Evaporator w/O_2 flow

Instructions

1. Clean fused silica substrate following the *Cleaning Fused Silica Substrates* recipe.

2. Load the sample in an e-beam evaporator that has O_2 flow.

3. Deposit the layers according to the table listed below. Each AgO layer in this recipe should be deposited following the *AgO Seed Layer* recipe. The SiO_2 deposition should be monitored closely to ensure the electron beam is not

boring a hole into the material in the crucible (which changes the apparent deposition rate).

Material	**Thickness (nm)**	Rate(Å/s)	**Dep. Pressure (torr)**	**Temp (°C)**
AgO	2	0.1	9.62-5	27
Ag	68	0.5	3.58E-7	27
SiO_2	70	1.5	3.25E-7	29
AgO	2	0.1	9.67E-5	30
Ag	48	0.5	3.91E-7	29
SiO_2	70	1.5	3.51E-7	30
AgO	2	0.1	9.67E-5	31
Ag	68	0.5	3.58E-7	31

Multilayer Metamaterial Heterostructures: SiO_2/Ag

The following is the deposition conditions for the SiO_2/Ag heterostructures. The process for making these structures is extremely similar to the MSPF color filters, they just have different layer thicknesses[8].

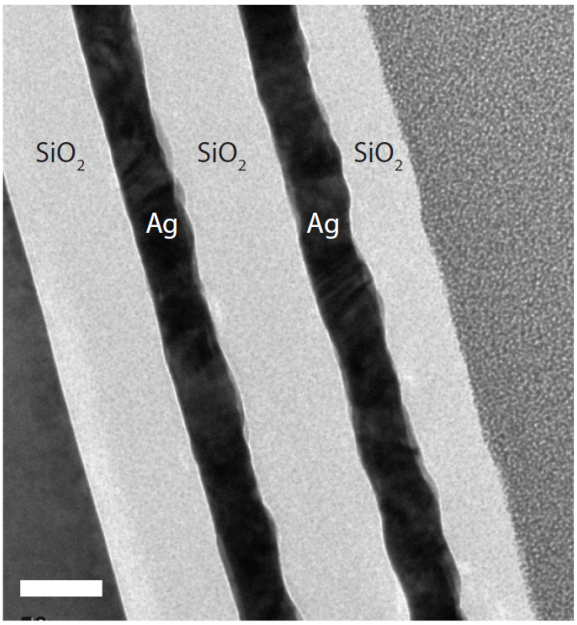

Figure 5.6: TEM micrograph of the SiO_2/Ag heterostructure fabricated using the deposition recipe in the table below. The scalebar is 100 nm

Ingredients	Supplies
• Clean Germanium substrate • E-beam Ag source • E-beam SiO_2 source • O_2 gas	• E-beam Evaporator w/O_2 flow

Instructions

1. Clean Germanium substrate following the *Cleaning Germanium Substrates* recipe
2. Load the sample in an e-beam evaporator that has O_2 flow.
3. Deposit the layers according to the table listed below. Each AgO layer in this recipe should be deposited following the *AgO Seed Layer* recipe. The SiO_2

deposition should be monitored closely to ensure the electron beam is not boring a hole into the material in the crucible (which changes the apparent deposition rate).

Material	**Thickness (nm)**	Rate(Å/s)	**Dep. Pressure (torr)**	**Temp (°C)**
AgO	2	0.2	9.48E-5	23
Ag	28	0.5	3.85E-7	24
SiO_2	40	1.5	3.35E-7	25
AgO	2	0.2	9.44E-5	27
Ag	28	0.5	3.07E-7	28
SiO_2	40	1.5	2.84E-6	30
AgO	2	0.2	9.30E-5	29
Ag	28	0.5	2.33E-6	30

Multilayer Metamaterial Heterostructures: TiO_2/Ag

The following is the deposition conditions for the TiO_2/Ag heterostructures[8].

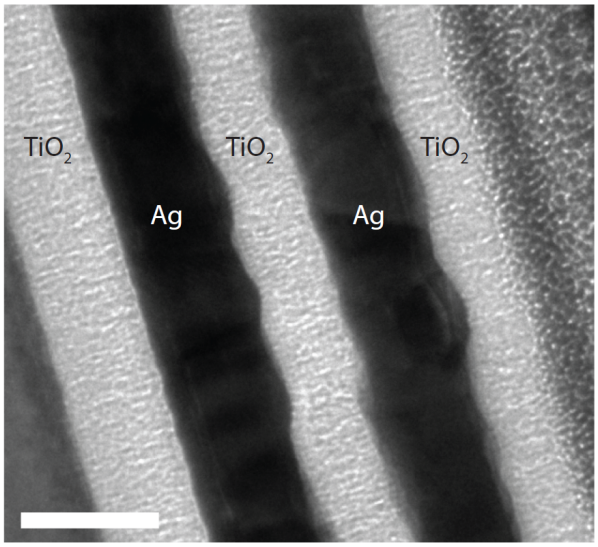

Figure 5.7: TEM micrograph of the TiO_2/Ag heterostructure fabricated using the deposition recipe in the table below. The scalebar is 50 nm.

Ingredients	Supplies
• Clean fused silica substrate • E-beam Ag source • E-beam Ti source • O_2 gas	• E-beam Evaporator w/O_2 flow

Instructions

1. Clean Germanium substrate following the *Cleaning Germanium Substrates* recipe.

2. Load the sample in an e-beam evaporator that has O_2 flow. The O_2 flow is used to deposit all materials. It is used in the AgO seed layer following the *AgO Seed Layer* recipe. It is also used to deposit the TiO_2. Rather than using a TiO_2 source, a Ti source is used and O_2 is flowed throughout the course of the deposition to reactively deposit TiO_2. The pressure during each Ti + O_2 step starts at 9.9E-5, but the pressure rapidly drops as the Ti evaporates into the chamber.

Material	**Thickness (nm)**	Rate(Å/s)	**Dep. Pressure (torr)**	**Temp (°C)**
Ti + O_2	40	0.5	8.175E-5	30
AgO	2	0.2	9.62-5	35
Ag	68	0.5	1.91E-6	35
Ti + O_2	40	0.5	8.095E-5	39
AgO	2	0.2	9.48E-5	33
Ag	48	0.5	1.28E-6	39
Ti + O_2	40	0.5	8.005E-5	40

Multilayer Metamaterial Heterostructures: Ge/Ag

The following is the deposition conditions for the Ge_2/Ag heterostructures[8]. Ag wets extremely well to Ge, so the AgO seed layer is not necessary for these structures[9]. I used this method to remain consistent with the other two fabricated heterostructures, but for general Ge/Ag stacks, the AgO seed layer does not need to be used[8].

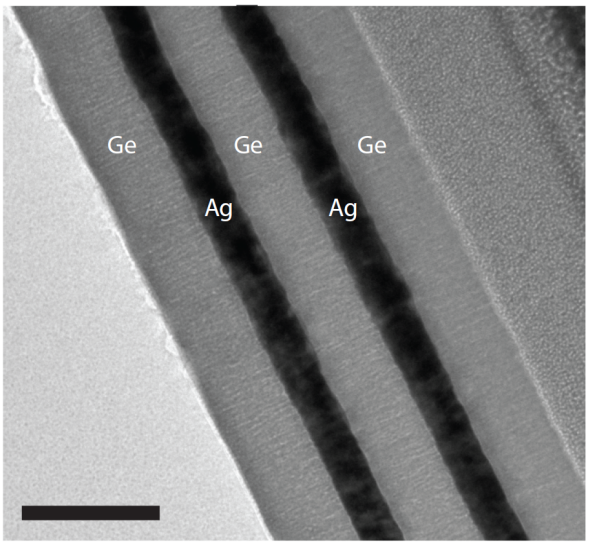

Figure 5.8: TEM micrograph of the Ge/Ag heterostructure fabricated using the deposition recipe in the table below. The scalebar is 100 nm

Ingredients	Supplies
• Clean silicon substrate	• E-beam Evaporator w/O_2 flow
• E-beam Ag source	
• E-beam Ge source	
• O_2 gas	

Instructions

1. Clean silicon substrate following the *Cleaning Silicon Substrates* recipe.
2. Load the sample in an e-beam evaporator that has O_2 flow.
3. Deposit the layers according to the table listed below. Each AgO layer in this recipe should be deposited following the *AgO Seed Layer* recipe.

Material	**Thickness (nm)**	Rate(Å/s)	**Dep. Pressure (torr)**	**Temp (°C)**
Ge	40	1.5	1.82E-6	24
AgO	2	0.1	9.13E-5	26
Ag	28	0.5	1.54E-6	27
Ge	40	1.5	1.70E-6	29
AgO	2	0.1	9.13E-5	31
Ag	28	0.5	1.38E-6	31
Ge	40	1.5	1.43E-6	32

5.6 Dry Etches

Straight-Sidewalled SiO_2 etch

This method adapted from the following reference [10]

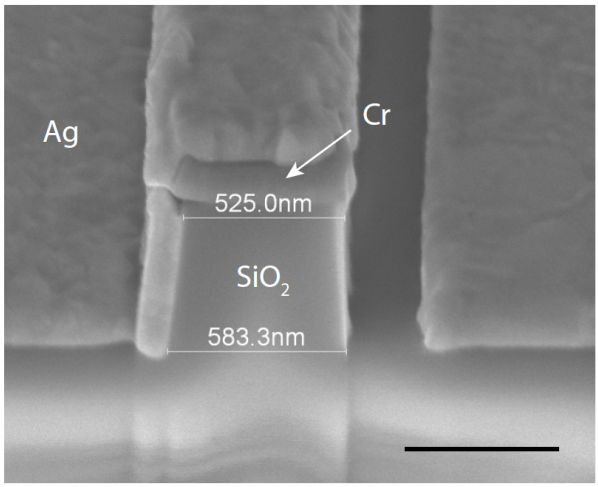

Figure 5.9: Focused ion beam cross-section of a structure milled using the etch described in the recipe below. The Cr mask was left on the structure to determine degree of undercutting and the whole structure was coated in Ag to prevent charging during cross-sectioning and imaging. The sample is tilted to 52°, which exaggerates the taper. Using the measurements on the image, the taper of the structure was calculated to be 1.6°. The scalebar is 500 nm.

Ingredients	Supplies
• Cr masked SiO_2 substrate	• ICP Etcher
• SF_6 gas	
• O_2 gas	
• C_4F_8 gas	

Instructions

1. The substrate should be prepared with a Cr mask. This etch has good selectivity between Cr and SiO_2. I had no issues with a 1:15 thickness ratio (which was likely overkill, and a lot less would likely also work well).

2. Prepare the chamber with a cleaning recipe. First clean with 10 minutes of an SF_6 plasma and then with 10 minutes of an O_2 plasma.

3. Condition the chamber using the etch recipe. The first step cools down the chamber without striking a plasma. The second step strikes the plasma and conditions the chamber. The parameters are as follows:

Step 1	
Temperature	5°C
Time	5 minutes
Step 2	
Temperature	5°C
Time	5 minutes
C_4F_8 Flow	40 sccm
O_2 Flow	1.8 sccm
RF FP	200 W
ICP FP	2100 W
Pressure	7 mTorr

4. To etch the sample, use the same recipe as during the conditioning step, but changing the time for step 2. The etch rate for this process was found to be 310 nm/min. The reported taper of a 400 nm wide and 600 nm tall pillar was less than 3°. For this process, the conditions reported by the etcher were: RF RP 3W, RF DC Bias 202V, ICP DC Bias 13W, and He flow 24.0 sccm.

5. The Cr mask can be removed using Cr-7 if there are no other materials on the chip. It took about 20 minutes to completely etch away a 40 nm Cr mask.

ICP Argon mill of Silver

This is a general Ar mill recipe that was adapted for use on an Oxford ICP system. This is a very physical process, and made even more so by the power parameters used.

Ingredients	Supplies
• Material to Etch	• ICP Etcher
• SF_6 gas	
• O_2 gas	
• Ar gas	

Instructions

1. Prepare the chamber with a cleaning recipe. First clean with 10 minutes of an SF_6 plasma and then with 10 minutes of an O_2 plasma.

2. Condition the chamber using the etch recipe for 5 minutes.

3. Run the recipe using the parameters listed in the table below. The etch rate is very dependent on chamber conditions, and for the smooth and large grained Ag I worked with, the rate would vary from 205 nm/min to 260 nm/min.

   The parameters are as follows:

Recipe	
Temperature	20°C
Ar Flow	30 sccm
RF FP	300 W
ICP FP	1000 W
Pressure	3 mTorr

5.7 Aligning to Hidden Features in Focused Ion Beam Systems

There are a number of ways to align features in focused ion beams, depending on the system in use. While there are many ion beam systems that have pattern generator add ons (such as the Raith ELPHY system) those are often not available. In the mirrored filter work in Chapter 4 of this thesis, backscatter contrast at high accelerating voltages was used to mill patterns aligned to the features hidden beneath the film. To use this type of alignment, the buried material has to have high backscatter contrast compared to the film that covers it.

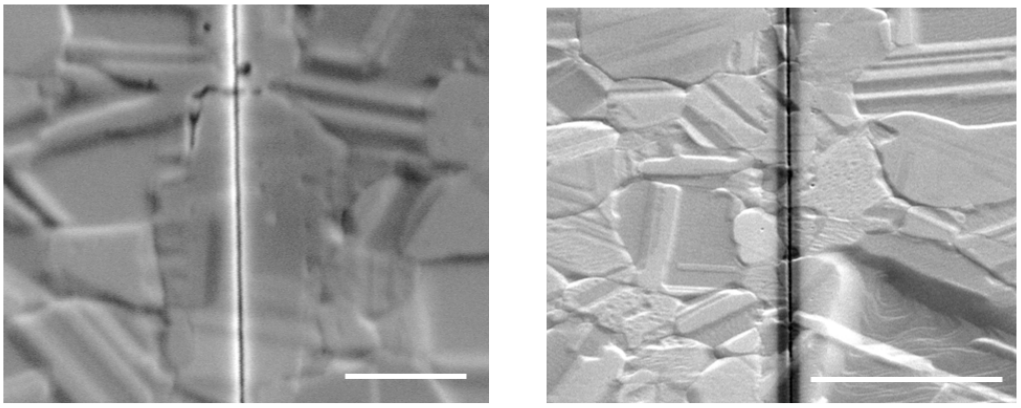

(a) (b)

Figure 5.10: The difference in feature visibility for the same feature imaged with an electron beam at (a) 3kV and 1.1 nA (scale bar 1 μm) and (b) 30 kV and 2.4 nA (scale bar 3 μm).

Ingredients	Supplies
• Buried feature sample	• Ion beam + ebeam system

1. Get the sample aligned, focused, and to eucentric height. Tilt to perpendicular with the ion beam
2. Mill a small feature in the center of the ion beam window that is sized large enough to mill the final pattern.
3. Using high magnification and high accelerating voltage, beam shift the electron beam to be exactly centered on the small milled feature.
4. Using the stage, move to the center of the hidden feature. The magnification of the electron beam needs to be the same as the previous step.

5. As long as there appears to be no drift, mill the feature with the ion beam. If there is drift, raster the electron and ion beams somewhere that can be damaged and repeat steps 2 and 3.

5.8 E-beam Deposition Tips

I spent about half my PhD on an electron beam evaporator, so I've accumulated some tips I always tell the new users of the system I managed. These are not in recipe format, but I thought worth mentioning nonetheless.

Electron Beam Evaporation of Oxides

Be wary of depositing oxide materials in ebeam evaporators, especially those without gas flow capabilities. The O_2 often evaporates at a different rate than the metal which depletes the source of O_2 and changes the stoichiometric ratio of both the source material and the deposited film. Whenever possible, I recommend not bothering with oxide starters and doing a reactive deposition by flowing O_2 during a metal deposition. Using this method, I've been able to deposit Al_2O_3 that was a good enough oxide to serve as as a pseudobosch etch mask. I also recommend depositing TiO_2 using this method.

Lift-off Considerations

The configuration of an electron beam evaporation system is at least as important as the recipe used for lift-off. The longer the chase in a deposition system, the more directional the deposition. Systems with shorter chases make lift-off more challenging because the increased angular spread of the deposition increases the amount of material deposited on the sidewalls. To reduce sidewall deposition, it is advisable to not use substrate rotation and to mount the sample as perpendicular to the source as possible. The lack of rotation will increase shadowing effects that can distort features, but this is preferable to not being able to lift-off at all.

References

[1] K. R. Williams, K. Gupta, and M. Wasilik. "Etch rates for micromachining processing-Part II". In: *Journal of Microelectromechanical Systems* 12.6 (2003), pp. 761–778.

[2] Shiyu Sun et al. "Surface termination and roughness of Ge(100) cleaned by HF and HCl solutions". In: *Applied Physics Letters* 88.2 (2006), p. 021903.

[3] O. J. Martin, K. Thyagarajan, and C. Santschi. "A New Fabrication Method for Aluminum and Silver Plasmonic Nanostructures". In: *Workshop on Optical Plasmonic Materials (The Optical Society of America)* (2014).

[4] J. Diebel et al. "Fabrication of large-scale ultra-smooth metal surfaces by a replica technique". In: *Applied Physics A* 73.3 (2001), pp. 273–279.

[5] Jong Hyuk Park et al. "Fabrication of smooth patterned structures of refractory metals, semiconductors, and oxides via template stripping". In: *ACS applied materials & interfaces* 5.19 (2013), pp. 9701–9708.

[6] Mary X. Wang, Soyoung E. Seo, Paul A. Gabrys, Dagny Fleischman, Byeongdu Lee, Youngeun Kim, Harry A. Atwater, Robert J. Macfarlane, and Chad A. Mirkin. "Epitaxy: Programmable Atom Equivalents Versus Atoms". In: *ACS Nano* 11.1 (2017), pp. 180–185. DOI: 10.1021/acsnano.6b06584.

[7] Dagny Fleischman, Luke A. Sweatlock, Hirotaka Murakami, and Harry Atwater. "Hyper-selective plasmonic color filters". In: *Opt. Express* 25.22 (2017), pp. 27386–27395. DOI: 10.1364/OE.25.027386.

[8] Georgia T. Papadakis, Dagny Fleischman, Artur Davoyan, Pochi Yeh, and Harry A. Atwater. "Optical magnetism in planar metamaterial heterostructures". In: *Nature Communications* 9.296 (2018). DOI: 10.1038/s41467-017-02589-8.

[9] Hong Liu et al. "Enhanced surface plasmon resonance on a smooth silver film with a seed growth layer". In: *ACS nano* 4.6 (2010), pp. 3139–3146.

[10] Michael David Henry. "ICP Etching of Silicon for Micro and Nanoscale Devices". PhD thesis. California Institute of Technology, 2010.